Title
A Mathematical Algorithm for Estimating the Rotational Diffusion Coefficients from X-ray Photon Correlation Spectroscopy Data

Author
Hu, Zixi

Publication Date
2021

Peer reviewed|Thesis/dissertation

A Mathematical Algorithm for Estimating the Rotational Diffusion Coefficients from X-ray Photon Correlation Spectroscopy Data

by

Zixi Hu

A dissertation submitted in partial satisfaction of the

requirements for the degree of

Doctor of Philosophy

in

Applied Mathematics

in the

Graduate Division

of the

University of California, Berkeley

Committee in charge:

Professor James A. Sethian, Chair
Professor Laurent El Ghaoui
Professor Per-Olof Persson

Spring 2021

A Mathematical Algorithm for Estimating the Rotational Diffusion Coefficients from X-ray Photon Correlation Spectroscopy Data

by

Zixi Hu

Abstract

A Mathematical Algorithm for Estimating the Rotational Diffusion Coefficients from X-ray Photon Correlation Spectroscopy Data

by

Zixi Hu

Doctor of Philosophy in Applied Mathematics

University of California, Berkeley

Professor James A. Sethian, Chair

The Brownian motion of particles can be decomposed into translational and rotational components, characterized by translational and rotational diffusion coefficients respectively. Measuring these two coefficients plays an important role in determining the structure and understanding the dynamic properties of materials, with benefit to research in such areas as molecular biology, material sciences. One of the promising tools for investigation of Brownian motion is the emerging X-ray Photon Correlation Spectroscopy (XPCS), which can capture dynamics of samples comprising large groups of particles in a broad range of time scales and length scales. Methods for estimating translational diffusion coefficients on the basis of the temporal auto-correlation analysis of XPCS images are used widely. However, to the best of our knowledge, there is no XPCS-based algorithm for assessing the rotational diffusion coefficients from such temporal auto-correlation data. In this thesis, we take a different route, and propose exploiting an angular-temporal cross-correlation function whose values are approximated by an estimator based on the collected experimental images. We prove the consistency of this estimator by deriving a tail bound. A numerical algorithm, MTECS, for estimating the rotational diffusion coefficients from the cross-correlation is designed and implemented. We demonstrate the capability of this algorithm by testing it on a range of simulated data.

Contents

Acknowledgments

First, I want to express my genuine gratitude to my advisor, James Sethian, for his patient guidance, constant encouragement and support that help me make through the whole journey. Thank him for opening the door to those great opportunities for me.

I would like to thank Jeffrey Donatelli for leading me through the basis of X-ray techniques, for his excellent ideas and advice, for the inspiring conversations, and for the chats about video games.

The Mathematics Group at LBNL has been an important part during these years. I want to thank all its members for the joyful conversations during lunch time, for organizing the Applied Math happy hours and virtual zoom lunches, for leading me to the football and the gym. Thank them for helping me stay healthy both mentally and physically, especially during the time of the pandemic.

I want to thank all my dissertation committee members, James Sethian, Per-Olof Persson, and Laurent El Ghaoui for their helpful feedback.

Many thanks to Mark Sutton, Alex Hexemer, Sujoy Roy, Hilmar Koerner, Edward Trigg, Lutz Wiegart, Andrei Fluerasu for the enlightening conversations in development of this work.

This work was partially supported by the Center of Advanced Mathematics for Energy Research Applications (CAMERA) funded by the U.S. Dept. of Energy's Office of Advanced and Scientific Computing Research and Basic Energy Sciences and by Laboratory Directed Research and Development funds from Berkeley Lab, both under contract number DE-AC02-05CH11231. This research also used resources of the National Energy Research Scientific Computing Center (NERSC), operated under the same contract number.

Chapter 1

Introduction

Investigation of the Brownian motion of different types of particles attracts considerable attention in research across such fields such as molecular biology and material sciences. For particles suspended in fluids, this Brownian results from collisions from solvent particles whose size are usually much smaller than the solutes, leading to random reposition and reorientation. If the suspension is dilute enough so that the direct interaction and hydrodynamics interaction disappear, then in the thermal equilibrium state, the random motion of particles can be characterized by the translational diffusion coefficient D_t and the rotational diffusion coefficient D_r in two-dimensional case. In the three-dimensional case, a 3×3 rotational diffusion tensor is required to fully describe the rotational diffusion. Knowledge of these parameters provides information about both the static structure and dynamic properties of the particles, opening the door for understanding functions and transport process of proteins [18], synthesis and stability of materials [28], and biomolecular reactions [38], etc.

As an emerging X-ray diffraction techniques, X-ray photon correlation spectroscopy (XPCS) is a promising tool for analyzing disordered systems, whose Brownian motion reveals considerable information about the underlying system. Due to the short wavelength of X-ray, XPCS is able to probe length scale down to nanometers. In XPCS experiments, a sample is illuminated by X-ray beams and the intensity of the scattered field is recorded by detectors. (See Fig. 1.1 for an illustration of the experiments). The inhomogeneity of the sample leads to the irregular interference of the fields scattered by different particles, and consequently results in brightness variation of different parts of the collected images. Typically, images collected from disordered systems in XPCS experiments present a grainy texture, often referred to as a "speckle" pattern. Valuable knowledge of the electron density distribution within the sample can be recovered by analyzing the images. Furthermore, the temporal variation of the speckle pattern yields information of the fluctuation of the electron density distribution and thus can be used for studying the dynamic properties of the sample.

The most classical tool for analyzing the images is the auto-correlation g_2, which is defined

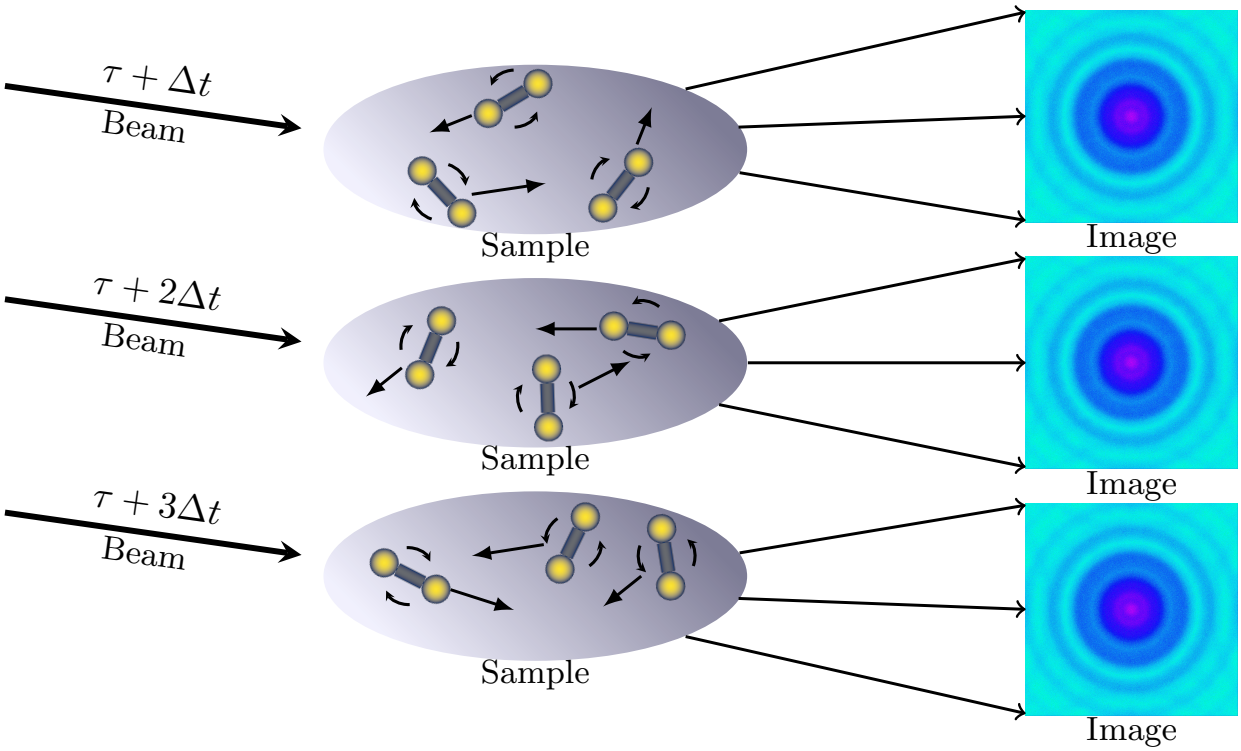

Figure 1.1: Illustration of the XPCS experiments.

based on the second-order degree of coherence [49]. The translational diffusion coefficient D_t can be measured by fitting the auto-correlation g_2 to parametric models, which will be introduced later in Chapter 2. Other applications of g_2 are described in [31], [44], [42]. However, to the best of our knowledge, there is no current algorithm to extract the rotational diffusion coefficient D_r from XPCS experimental data, though the required raw data is accessible.

One reason that the auto-correlation g_2 does not capture rotational information is that it does not utilize the angular fluctuation of the images. Such information is preserved when the X-ray exposure time is below the rotational diffusion relaxation time of the particles in samples, which can be achieved by conducting the XPCS experiments on beamlines which have ultrafast pulses [30, 47], or by slowing down the motion of the particles. In this thesis, we demonstrate the feasibility to estimate the rotational diffusion coefficient D_r in a two-dimensional case by capitalizing on the angular fluctuation. We first propose exploiting the more informative angular-temporal cross-correlation, which is able to extract the information contained in the angular fluctuation. Mathematically, this cross-correlation can be regarded as an probability expectation which in practice can be approximated by an estimator whose consistency we prove in this thesis. In order to then extract the rotational

diffusion coefficient D_r once the angular-temporal cross-correlation is estimated, we build a numerical algorithm named "Multi-tiered Estimation for Correlation Spectroscopy (MTECS)", following the multi-tiered iterative projection (M-TIP) philosophy [9, 10, 39]. Our algorithm is built by constructing a set of operators which taken together form an iteration mapping the cross-correlation to a form that agrees with the underlying mathematical model.

Our approach requires almost no prior assumption about the structure of the electron density distribution. However, if such knowledge is a priori known, MTECS can take advantage by including additional operators to enforce the corresponding constraints. By incorporating with additional noise reduction, the MTECS algorithm is robust against noisy data and is able to output filtered cross-correlation data for further analysis. Much of the mathematical formulation and underlying algorithm lend themselves to a three-dimensional version, which will be reported on elsewhere.

In Chapter 2, we introduce the background knowledge including the notations, description of the rotational Brownian motion and the mathematical formulation of the XPCS experimental data. In Chapter 3, we present angular-temporal cross-correlation analysis of the XPCS images and prove the consistency of the estimator of the cross-correlation data. In Chapter 4 we construct our MTECS mathematical algorithm to extract the rotational diffusion coefficient D_r from the estimated cross-correlation data. In Chapter 5, we illustrate the capability of our algorithm by testing it on a series of simulated XPCS images. In Chapter 7, two extensions will be discussed.

Chapter 2

Background

In this chapter, we formulate background relevant to Brownian motion and XPCS. In this thesis, we will discuss about both the real space and Fourier space. First, we introduce notations and definitions used through this paper.

2.1 Notations and Definitions

Let $\boldsymbol{r}$ and $\boldsymbol{q}$ denote the Cartesian coordinates in real space and Fourier space, which can be expressed in terms of the polar coordinates as $\boldsymbol{r} = (r, \theta)$ and $\boldsymbol{q} = (q, \phi)$ where $r = |\boldsymbol{r}|$, $q = \boldsymbol{q}$ are the radial coordinates and θ, ϕ are the angular coordinates.

Assume a function $f : \mathbb{R}^d \to \mathbb{C}$. Let $L^1(\mathbb{R}^d)$ denote the Banach space of complex-valued Lebesgue integrable functions on set $\Omega \subset \mathbb{R}^d$ with norm

$$\|f\|_{L^1(\Omega)} = \int_\Omega |f(\mathbf{r})| d\mathbf{r}, \tag{2.1}$$

and $L^2(\mathbb{R})$ denote the Hilbert space of complex-value Lebesgue integrable functions on set $\Omega \subset \mathbb{R}^d$ with norm

$$\|f\|_{L^2(\Omega)} = \int_\Omega |f(\mathbf{r})|^2 d\mathbf{r}. \tag{2.2}$$

We use the following definition of the Fourier transform:

Definition 2.1. *Define the Fourier transform of $f \in L^1(\mathbb{R}^d) + L^2(\mathbb{R}^d)$ as*

$$(\mathcal{F}f)(\boldsymbol{q}) = \hat{f}(\boldsymbol{q}) = \int_{\mathbb{R}^d} f(\mathbf{r}) e^{-2\pi i \mathbf{r}\cdot\boldsymbol{q}} d\mathbf{r}, \tag{2.3}$$

and its inverse transform as

$$(\mathcal{F}^{-1}f)(\mathbf{r}) = \int_{\mathbb{R}^d} \hat{f}(\mathbf{q}) e^{2\pi i \mathbf{r}\cdot\boldsymbol{q}} d\mathbf{q}. \tag{2.4}$$

The definition of the Fourier transform in $L^2(\mathbb{R}^d)$ is extended from $L^1(\mathbb{R}^2)$ by using a density argument.

Definition 2.2. *The autocorrelation of a function $f \in L^2(\mathbb{R}^d)$ is given by*

$$(Af)(\mathbf{r}) = \int_{\mathbb{R}^d} f(\mathbf{r})\overline{f(\mathbf{r}-\mathbf{r}')} d\mathbf{r}'. \tag{2.5}$$

Definition 2.3. *For function $f \in L^2([0, 2\pi])$, its Fourier series is given by*

$$f(\phi) = \sum_{m=-\infty}^{\infty} f_m e^{im\phi}, \tag{2.6}$$

where the coefficients f_m is given by

$$f_m = \frac{1}{2\pi}\int_0^{2\pi} f(\phi) e^{-im\phi} d\phi. \tag{2.7}$$

Definition 2.4. *The Wiener algebra $A([0, 2\pi])$ is the space of functions whose Fourier series is absolutely convergent. For $f \in A([0, 2\pi])$, the norm is*

$$\|f\|_A = \sum_{m=-\infty}^{\infty} |f_m|. \tag{2.8}$$

One important property of the Wiener algebra is that it is closed under pointwise multiplication:

$$\|f \cdot g\|_A \leq \|f\|_A \|g\|_A. \tag{2.9}$$

By realizing that each function $f : \mathbb{R}^2 \to \mathbb{C}$ can be turned into a set of functions $f(r, \cdot) : [0, 2\pi] \to \mathbb{C}$, each formed by fixing the radial coordinate r, we can calculate the Fourier series of $f(r, \cdot)$ to make the following definition:

Definition 2.5. *For $f \in L^2(\mathbb{R}^2)$, its circular harmonic series is given by*

$$f(r, \phi) = \sum_{m=-\infty}^{\infty} f_m(r) e^{im\phi}, \tag{2.10}$$

where the circular harmonic coefficients $f_m(r)$ are given by

$$f_m(r) = \frac{1}{2\pi}\int_0^{2\pi} f(r, \phi) e^{-im\phi} d\phi. \tag{2.11}$$

Let J_m denote the Bessel function of the first kind with integer order m, which can be defined using integral as follows:

Definition 2.6. *For an integer m, the Bessel function of the first kind with order m, denoted as J_m, can be defined as*

$$J_m(r) = \frac{1}{\pi}\int_0^\pi \cos(m\theta - r\sin\theta)d\theta. \tag{2.12}$$

Then we can make the following definition:

Definition 2.7. *The Hankel transform of order $m \geq -\frac{1}{2}$ of a function $f \in L^2(\mathbb{R}^+)$ is given by*

$$(\mathcal{H}_m f)(q) = \int_0^\infty f(r)J_m(qr)rdr. \tag{2.13}$$

The circular harmonic coefficients of a function $f \in L^1(\mathbb{R}^2) \cap L^2(\mathbb{R}^2)$ and its Fourier transform $\hat{f}$ can be related via the Hankel transform,

$$\hat{f}_m(q) = 2\pi(-i)^m \int_0^\infty f_m(r)J_m(2\pi qr)rdr, \tag{2.14}$$

$$f_m(q) = 2\pi i^2 \int_0^\infty \hat{f}_m(q)J_m(2\pi qr)qdq. \tag{2.15}$$

Definition 2.8. *For $f \in L^2([0,R])$ satisfying $f(R) = 0$, the Fourier-Bessel series of f is given by*

$$f(r) = \sum_{n=1}^\infty f_{mn}\frac{\sqrt{2}J_m(\frac{u_{m,n}}{R}r)}{RJ_{m+1}(u_{m,n})}, \tag{2.16}$$

where $u_{m,n}$ is the n-th nontrivial root of the m-th order Bessel function J_m and the coefficients are given by

$$f_{mn} = \int_0^R f(r)\frac{\sqrt{2}J_m(\frac{u_{m,n}}{R}r)}{RJ_{m+1}(u_{m,n})}rdr. \tag{2.17}$$

The basis of Fourier-Bessel series is orthonormal in the sense that

$$\int_0^R \frac{\sqrt{2}J_m(\frac{u_{m,n}}{R}r)}{RJ_{m+1}(u_{m,n})}\cdot\frac{\sqrt{2}J_m(\frac{u_{m,n'}}{R}r)}{RJ_{m+1}(u_{m,n'})}rdr = \delta(n-n'). \tag{2.18}$$

2.2 Mathematical Formulation of Brownian Motion

In this thesis, we consider a dilute two-dimensional system in which particles barely interact with each other due to the large distances between them.

For the non-interacting particles, there are several mathematical formulations of their translation Brownian motion, including the classical diffusion equation [11, 12], the Langevin equation [27], the Wiener process [51, 52, 53]. We present the definition of the standard multidimensional Wiener process, which is also introduced in [13, 34, 37].

Definition 2.9. *A stochastic process $W(\cdot) \in \mathbb{R}$ is a 1-dimensional Wiener process or Brownian motion if it has the following properties:*

(1) $W(0) = 0$ *almost surely.*

(2) $W(t) - W(s) \sim \mathcal{N}(0, t-s)$ *for all* $t \geq s \geq 0$.

(3) $W(t_1), W(t_2) - W(t_1), \cdots, W(t_n) - W(t_{n-1})$ *are independent for all* $0 < t_1 < t_2 \cdots < t_n$.

(4) $W(t)$ *is continuous in* t *almost surely.*

Definition 2.10. *A stochastic process $\boldsymbol{W}^{(d)}(\cdot) = (W_1(\cdot), \cdots, W_d(\cdot)) \in \mathbb{R}^d$ is a d-dimensional Wiener process or Brownian motion if it has the following properties:*

(1) For $k \in [1, d] \cap \mathbb{Z}$, the component $W_k(\cdot)$ is a 1-dimensional Wiener process.

(2) The components are independent.

Here we consider the isotropic translation diffusion only. The non-isotropic translation diffusion is not within the scope of this thesis. Let $\boldsymbol{r}(\cdot)$ be the position of the center of mass of a Brownian particle with translation diffusion coefficient D_r in two-dimensional space. Then we have

$$\boldsymbol{r}(t) - \boldsymbol{r}(0) \sim \sqrt{2D_t} W^{(2)}(t). \tag{2.19}$$

To fully characterize the three-dimensional rotational diffusion, a 3×3 diffusion tensor is required. The description of the orientation depends on the choice of a set of particle fixed axes. By choosing the particle fixed axes as the principal axes of inertia, the rotational diffusion tensor can be diagonalized. We say the rotational diffusion is isotropic if diagonal entries of such tensor are all the same. The equation of the isotropic rotational diffusion was derived in [17] by means of the quaternions. The anisotropic rotational diffusion was treated in [15] using the Cayley-Klein parameters.

In the two-dimensional system we consider, each particle rotates with respect to an axis that passes through the center of mass of the particle and is perpendicular to the system.

Let $SO(2)$ be the two-dimensional rotation group, which can be parametrized by the angle of the rotation. Stated by [8, 34], the orientation $\theta(t) \in SO(2)$ of a Brownian particle with rotational diffusion coefficient D_r can be described as

$$\theta(t) - \theta(0) \sim \sqrt{2D_r}W(t). \tag{2.20}$$

Remark 2.2.1. Though $\theta(t)$ takes value over $(-\infty, \infty)$ in the above equation the orientation, and in [34], $\theta(t)$ is viewed as a random variable on $[0, 2\pi)$, by reducing Eq. (2.20) modulo 2π, one can establish the equivalence between them through the Poisson Summation Formula (Theorem A.2). Naturally, their characteristic functions are the same.

Assuming decoupling of the translation diffusion and rotational diffusion, we summarize the above formulations to give the description of the system studied in this thesis:

Condition 2.1. *The system contains N_p identical particles with position $\{\boldsymbol{r}_n(t)\}_{n=1}^{N_p}$ and orientation $\{\theta_n(t)\}_{n=1}^{N_p}$ satisfying:*

(1) For each $n \in [1, N_p] \cap \mathbb{Z}$, $\boldsymbol{r}_n(t) - \boldsymbol{r}_n(0) \sim \sqrt{2D_t}W^{(2)}(t)$ and $\theta_n(t) - \theta_n(0) \sim \sqrt{2D_r}W(t)$.

(2) $\boldsymbol{r}_n(t), n \in [1, N_p] \cap \mathbb{Z}$ and $\theta_n(t), n \in [1, N_p] \cap \mathbb{Z}$ are all independent.

(3) For each $n \in [1, N_p] \cap \mathbb{Z}$, $\theta_n(0)$ is uniformly distributed on $[0, 2\pi)$, and $\boldsymbol{r}_n(0)$, whose characteristic function is χ, is uniformly distributed on an initial domain.

The last one is used for calculation of the ensemble average in Section 3.2. Section 3.3 addresses and overcomes the challenge that one cannot repeat the experiment to acquire good approximation of such initial distributions.

2.3 Mathematical Formulation of X-ray Photon Correlation Spectroscopy

Let $\rho : \mathbb{R}^2 \to \mathbb{R}$ be the electron density of an individual particle whose center of mass is at the origin and orientation is associated with angle 0. Throughout this thesis, we assume:

Condition 2.2. *The electron density ρ satisfies that ρ, $|\boldsymbol{r}\rho(\boldsymbol{r})| \in L^1(\mathbb{R}^2) + L^2(\mathbb{R}^2)$.*

In practice, the above assumption holds naturally since the electron density ρ is always a nicely-behaved function that can be treated to be smooth and compactly supported.

The above condition ensures the existence of the Fourier transform of ρ,

$$\hat{\rho}(\boldsymbol{q}) = \int \rho(\boldsymbol{r}) e^{-2\pi i \boldsymbol{q}\cdot\boldsymbol{r}} d\boldsymbol{r}, \tag{2.21}$$

which is usually called the form factor in X-ray context, and can be expressed in circular harmonic expansion as

$$\hat{\rho}(q,\phi) = \sum_{m=-\infty}^{\infty} \hat{\rho}_m(q) e^{im\phi}, \tag{2.22}$$

where $\hat{\rho}_m$ are the circular harmonic coefficients of $\hat{\rho}$. The intensity I is the squared modulus of the form factor $\hat{\rho}$,

$$I(\boldsymbol{q}) = |\hat{\rho}(\boldsymbol{q})|^2, \tag{2.23}$$

which can also be represented in circular harmonic expansion with coefficients $\{I_m(q)\}_{m=-\infty}^{\infty}$.

$$I(q,\phi) = \sum_{m=-\infty}^{\infty} I_m(q) e^{im\phi}, \tag{2.24}$$

The convergence of Eq. (2.22) and Eq. (2.24) are proved given Condition 2.2 (See Lemma 3.1).

Let $R(\theta)$ be the rotation matrix that rotates the angle θ to angle 0. Then the overall electron density distribution of the sample is

$$\bar{\rho}(\boldsymbol{r},t) = \sum_{n=1}^{N_p} \rho\Big(R\big(\theta_n(t)\big)\cdot\big(\boldsymbol{r}-\boldsymbol{r}_n(t)\big)\Big). \tag{2.25}$$

The scattering vectors at which the images are recorded form a surface in the Fourier space, termed as the Ewald sphere [14]. Assuming a flat Ewald sphere, these scattering vector $\boldsymbol{q}$ can be reduced to its component orthogonal to the incident beam. In the absence of multiple scattering, the scattered field in the far field can be modeled by the Fourier transform of $\bar{\rho}(\boldsymbol{r},t)$,

$$\begin{aligned} E(\boldsymbol{q},t) &= \int_{\mathbb{R}^2} \bar{\rho}(\boldsymbol{r},t) e^{-2\pi i \boldsymbol{q}\cdot\boldsymbol{r}} d\boldsymbol{r} && (2.26)\\ &= \sum_{n=1}^{N_p} e^{-2\pi i \boldsymbol{q}\cdot\boldsymbol{r}_n(t)} \int_{\mathbb{R}^2} \rho\Big(R\big(\theta_n(t)\big)\boldsymbol{r}\Big) e^{-2\pi i \boldsymbol{q}\cdot\boldsymbol{r}} d\boldsymbol{r} && (2.27)\\ &= \sum_{n=1}^{N_p} e^{-2\pi i \boldsymbol{q}\cdot\boldsymbol{r}_n(t)} \hat{\rho}\Big(R\big(\theta_n(t)\big)\cdot\boldsymbol{q}\Big) && (2.28)\\ &= \sum_{n=1}^{N_p} e^{-2\pi i \boldsymbol{q}\cdot\boldsymbol{r}_n(t)} \hat{\rho}\big(q,\phi-\theta_n(t)\big). && (2.29) \end{aligned}$$

Let $J(\cdot, t)$ denote the scattering images recorded by the detectors at time t. For any scattering vector $\boldsymbol{q}$, $J(\boldsymbol{q}, t)$ is the squared modulus of the scattered field $E(\boldsymbol{q}, t)$,

$$J(\boldsymbol{q}, t) = |E(\boldsymbol{q}, t)|^2 = \left| \sum_{n=1}^{N_p} e^{-2\pi i \boldsymbol{q} \cdot \boldsymbol{r}_n(t)} \hat{\rho}\big(q, \phi - \theta_n(t)\big) \right|^2. \tag{2.30}$$

The temporal auto-correlation function g_2 is defined as follows:

$$g_2(q, \phi, t) = \frac{\langle J(q, \phi, \tau) J(q, \phi, \tau + t) \rangle}{\langle J(q, \phi, \tau) \rangle^2}, \tag{2.31}$$

where the angle bracket $\langle \cdot \rangle$ indicates the ensemble average that is equivalent to the time average taken over τ for systems under thermal equilibrium. For isotropic systems, g_2 does not depend on ϕ [8]. In this case, the averages are also taken over ϕ, and the dependency of g_2 on ϕ can be dropped, thus becoming $g_2(q, t)$.

For spherical particles undergoing free diffusion [4, 45, 46],

$$g_2(q, t) = 1 + e^{-8\pi^2 q^2 t D_t}. \tag{2.32}$$

and hence estimation of D_t can be obtained according to this equation.

Remark 2.3.1. Due to the factor 2π in the formulation of Fourier transform (Definition 2.1), there is a difference of factor $4\pi^2$ between Eq. (2.32) and the equation $g_2(q, t) = 1 + e^{-2q^2 t D_t}$ introduced elsewhere.

For non-spherical particles, the particle structure plays an important role. Assuming anistropic structure of particles and decoupling of translation diffusion and rotational diffusion, we are able to show (see Section 3.2) that

$$g_2(q, t) = 1 + e^{-8\pi^2 q^2 t D_t} \frac{\left(\sum_{m=-\infty}^{\infty} |\hat{\rho}_m(q)|^2 e^{-m^2 t D_r} \right)^2}{\left(\sum_{m=-\infty}^{\infty} |\hat{\rho}_m(q)|^2 \right)^2}. \tag{2.33}$$

Other than D_t and D_r, the above equation involves also the unknowns, $|\hat{\rho}_m(q)|^2$. However, there may be insufficient information in Eq. (2.33) to extract all of these quantities, which leads us to the analysis introduced in the next chapter.

Chapter 3

Formulation, Analysis, and Estimation of Angular-temporal Cross-correlation

In current XPCS experiments, one can extract the angular fluctuation of the speckle patterns. In this and the following chapters, we show that this provides key information for estimating the rotational diffusion coefficients D_r as demonstrated in the following chapters. The central idea stems from the realization that the angular fluctuation at different angles are correlated because the pairs of photons that are scattered to different directions can be correlated by the rotational dynamics. By capturing such pairs of photons, we can probe the rotational motion of the particles. Furthermore, the de-correlation of the angular fluctuation is caused by the relaxation of the rotational diffusion. Therefore, measurement of the de-correlation of the angular fluctuation is crucial to retrieve the relaxation time of the rotational diffusion, enabling us to estimate the rotational diffusion coefficients.

The temporal autocorrelation function g_2 fails to take advantage of such information in the angular fluctuation, since g_2 does not depends on the angular coordinates for the isotropic systems of our interests. Instead, we propose using the angular-temporal cross-correlation function, whose formulation will be presented in Section 3.1.

Armed with an appropriate formulation of the angular-temporal cross-correlation function, we can then explicitly calculate the angular-temporal cross-correlation (Section 3.2), illustrating that the cross-correlation can be related to the rotational diffusion and the structure of the particles. The derivation of Eq. (2.33) is also provided in this section.

In practice, since the cross-correlation can be only approximated using a finite amount of images, extra statistical bias is introduced. In Section 3.3, we present an estimator of the desired cross-correlation and prove its consistency.

3.1 Angular-temporal Cross-correlation

As said earlier, one disadvantage of the temporal auto-correlation g_2 is that it correlates points at only the same spatial positions (See Figure 3.1a). However, more information can be uncovered by correlating points at different spatial positions. Thus we propose the angular-temporal cross-correlation,

$$C(q, q', \Delta\phi, t) = \langle J(q, \phi, \tau) J(q', \phi + \Delta\phi, \tau + t) \rangle, \tag{3.1}$$

where, as before, angle brackets indicate the ensemble average. See Figure 3.1b for an illustration. Since the system of interest is isotropic and in equilibrium state, the ensemble average equals the average performed over the angular coordinates ϕ and time τ. Then Eq. (3.1) can be rewritten as

$$C(q, q', \Delta\phi, t) = \Big\langle \Big\langle \big(J(q, \phi, \tau) - \langle J(q, \phi, \tau)\rangle_\phi\big) \cdot \big(J(q', \phi + \Delta\phi) - \langle J(q', \phi, t + \tau)\rangle_\phi\big) \Big\rangle_\phi \Big\rangle_\tau + \big\langle \langle J(q, \phi, \tau)\rangle_\phi \cdot \langle J(q', \phi, \tau + t)\rangle_\phi \big\rangle_\tau \tag{3.2}$$

where $\langle\cdot\rangle_\phi$ is the angular average and the $\langle\cdot\rangle_\tau$ is the temporal average. The first term on the right-hand-side is the correlation of the angular fluctuation of the images.

The angular-temporal cross-correlation C can be reduced to the numerator of the temporal autocorrelation g_2 by setting $q = q'$ and $\Delta\phi = 0$, and hence the data obtained through C is a proper subset of the data obtained through g_2, which implies that most of the analysis methods designed for g_2 could be adapted to take C as input. Moreover, given the same images, g_2 generates only a data matrix, while the more informative C generates a 4-way data tensor. To unleash more potential of the cross-correlation C, we designed the MTECS algorithm (See Chapter 4).

In the context of other X-ray diffraction experiments, most of whom focus on revealing information about static structures, researchers have been exploring application of reduced forms of the cross-correlation Eq. (3.1) with consideration of only angular or spatial effect. It is realized that the cross-correlation analysis is able to discover the symmetries of local structures in disordered systems [54], and supporting theory was developed by [2] and validated later by simulations [25]. Several algorithms for determination of macromolecular structure utilizing the cross-correlation data gathered in Fluctuation X-ray scattering experiments [43, 29, 40, 10] were constructed on the foundation of the theory built in [20]. For anisotropic systems, [26, 33] applied the techniques suggested by [7, 1, 32] to investigate the orientational order.

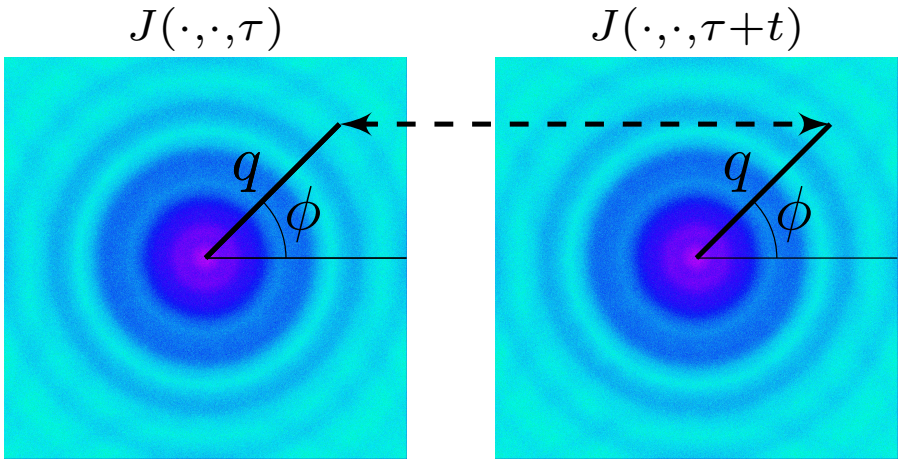

(a)

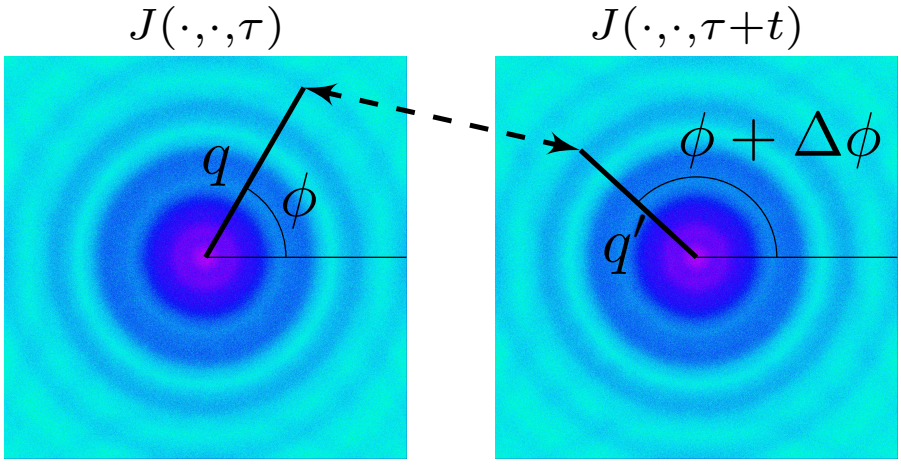

(b)

Figure 3.1: (a) Illustration of the angular-temporal cross-correlation C correlating two points at different spatial positions; (b) Illustration of the autocorrelation g_2 correlating two points at the same spatial positions.

3.2 Calculation of Ensemble Average

By viewing the image J as a function of the positions $\{\boldsymbol{r}_n(t)\}_{n=1}^{N_p}$ and orientations $\{\boldsymbol{r}_n(t)\}_{n=1}^{N_p}$, which are stochastic processes satisfying Condition 2.1, the angular-temporal cross-correlation Eq. (3.1) can be expressed in terms of the expectation of those stochastic processes,

$$C(q,q',\Delta\phi,t)=\frac{1}{2\pi}\int_0^{2\pi}\mathbb{E}[J(q,\phi,0)J(q',\phi+\Delta\phi,t)]d\phi. \tag{3.3}$$

In this section, we calculate the expectation explicitly to obtain the following theorem:

Theorem 3.1. *Given Condition 2.1 and Condition 2.2, we have*

$$\begin{aligned}
&\mathbb{E}[J(q,\phi,0)J(q',\phi',t)]\\
=\;& N_p\sum_{m=-\infty}^{\infty}e^{-im(\phi'-\phi)}I_m(q)\overline{I_m(q')}e^{-m^2tD_r} \qquad (3.4)\\
&+N_p(N_p-1)I_0(q)I_0(q')\\
&+N_p(N_p-1)\big|\chi\big(2\pi(\boldsymbol{q}-\boldsymbol{q}')\big)\big|^2e^{-8\pi^2q^2tD_t}\left(\sum_{m=-\infty}^{\infty}e^{-im(\phi'-\phi)}\hat\rho_m(q)\overline{\hat\rho_m(q')}e^{-m^2tD_r}\right)^2\\
&+N_p(N_p-1)\big|\chi\big(2\pi(\boldsymbol{q}+\boldsymbol{q}')\big)\big|^2e^{-8\pi^2q^2tD_t}\left(\sum_{m=-\infty}^{\infty}e^{-im(\phi'-\phi)}\hat\rho_m(q)\hat\rho_{-m}(q')e^{-m^2tD_r}\right)^2\\
&+N_p(N_p-1)|\chi(2\pi\boldsymbol{q})|^2\hat\rho_0(q)\sum_{m=-\infty}^{\infty}e^{-im(\phi-\phi')}\overline{\hat\rho_m(q)}I_m(q')e^{-tm^2D_r}\\
&+N_p(N_p-1)|\chi(2\pi\boldsymbol{q})|^2\overline{\hat\rho_0(q)}\sum_{m=-\infty}^{\infty}e^{im(\phi-\phi')}\hat\rho_m(q)\overline{I_m(q')}e^{-tm^2D_r}\\
&+N_p(N_p-1)|\chi(2\pi\boldsymbol{q}')|^2e^{-8\pi^2q'^2tD_t}\hat\rho_0(q')\sum_{m=-\infty}^{\infty}e^{im(\phi-\phi')}I_m(q)\overline{\hat\rho_m(q')}e^{-tm^2D_r}\\
&+N_p(N_p-1)|\chi(2\pi\boldsymbol{q}')|^2e^{-8\pi^2q'^2tD_t}\overline{\hat\rho_0(q')}\sum_{m=-\infty}^{\infty}e^{-im(\phi-\phi')}\overline{I_m(q)}\hat\rho_m(q')e^{-tm^2D_r}\\
&+N_p(N_p-1)(N_p-2)|\chi(2\pi\boldsymbol{q}')|^2e^{-8\pi^2q'^2tD_t}I_0(q)|\hat\rho_0(q')|^2\\
&+N_p(N_p-1)(N_p-2)\chi\big(-2\pi(\boldsymbol{q}+\boldsymbol{q}')\big)\chi(2\pi q)\chi(2\pi q')e^{-8\pi^2q'^2tD_t}\\
&\quad\cdot\overline{\hat\rho_0(q)\hat\rho_0(q')}\sum_{m=-\infty}^{\infty}e^{im(\phi-\phi')}\hat\rho_m(q)\hat\rho_{-m}(q')e^{-tm^2D_r}\\
&+N_p(N_p-1)(N_p-2)\chi\big(-2\pi(\boldsymbol{q}-\boldsymbol{q}')\big)\chi(2\pi q)\chi(2\pi q')e^{-8\pi^2q'^2tD_t}
\end{aligned}$$

$$
\begin{aligned}
&\cdot \overline{\hat{\rho}_0(q)}\hat{\rho}_0(q') \sum_{m=-\infty}^{\infty} e^{im(\phi-\phi')}\hat{\rho}_m(q)\overline{\hat{\rho}_m(q')}e^{-tm^2D_r} \\
&+ N_p(N_p-1)(N_p-2)\chi\big(2\pi(\boldsymbol{q}-\boldsymbol{q}')\big)\chi(2\pi q)\chi(-2\pi q')e^{-8\pi^2 q'^2 tD_t} \\
&\cdot \hat{\rho}_0(q)\overline{\hat{\rho}_0(q')} \sum_{m=-\infty}^{\infty} e^{-im(\phi-\phi')}\overline{\hat{\rho}_m(q)}\hat{\rho}_m(q')e^{-tm^2D_r} \\
&+ N_p(N_p-1)(N_p-2)\chi\big(2\pi(\boldsymbol{q}+\boldsymbol{q}')\big)\chi(2\pi q)\chi(2\pi q')e^{-8\pi^2 q'^2 tD_t} \\
&\cdot \hat{\rho}_0(q)\hat{\rho}_0(q') \sum_{m=-\infty}^{\infty} e^{-im(\phi-\phi')}\overline{\hat{\rho}_m(q)\hat{\rho}_{-m}(q')}e^{-tm^2D_r} \\
&+ N_p(N_p-1)(N_p-2)|\chi(2\pi\boldsymbol{q})|^2|\hat{\rho}_0(q)|^2 I_0(q') \\
&+ N_p(N_p-1)(N_p-2)(N_p-3)|\chi(2\pi\boldsymbol{q})|^2|\chi(2\pi\boldsymbol{q}')|^2 e^{-8\pi^2 q'^2 tD_t}|\hat{\rho}_0(q)|^2|\hat{\rho}_0(q')|^2,
\end{aligned}
$$

where the expectation is over the joint distribution of $\{\boldsymbol{r}_n(0)\}_{n=1}^{N_p}$, $\{\boldsymbol{r}_n(t)\}_{n=1}^{N_p}$, $\{\theta_n(0)\}_{n=1}^{N_p}$ *and* $\{\theta_n(t)\}_{n=1}^{N_p}$.

If the characteristic function χ is isotropic, then the right hand side of the above equation depends on ϕ and ϕ' only through $\phi' - \phi = \Delta\phi$, i.e. the integrand of the right-hand-side of Eq. (3.3) does not depend on ϕ. Thus $C(q, q', \Delta\phi, t)$ (Eq. (3.3)) is equivalent to the right hand side of Eq. (3.4).

Under the same assumption required by Theorem 3.1, we have

$$
\mathbb{E}[J(q,\phi,t)] = N_p I_0(q) + N_p(N_p-1)|\chi(\boldsymbol{q})|^2 e^{-8\pi^2 q^2 tD_t}|\hat{\rho}_0(q)|^2, \tag{3.5}
$$

whose derivation is presented in Appendix B.

If $\boldsymbol{r}_n(0)$ is distributed uniformly on a large enough domain with smooth boundary, which is always true in practice, the characteristic function $\chi(\cdot)$ can be approximately viewed as the indicator function at 0,

$$
\mathbf{1_0}(\boldsymbol{q}) = \begin{cases} 1 & \text{if } \boldsymbol{q} = \mathbf{0}, \\ 0 & \text{if } \boldsymbol{q} \neq \mathbf{0}. \end{cases} \tag{3.6}
$$

Additionally, suppose that the scattering vectors are non-zeros, i.e. $\boldsymbol{q} \neq \mathbf{0}$ and $\boldsymbol{q}' \neq \mathbf{0}$. Then only the first four terms remain in the expression of Eq. (3.4).

Taking $\boldsymbol{q} = \boldsymbol{q}'$, we can obtain Eq. (2.33),

$$
g_2(q,t) = \frac{1}{N_p}\frac{\sum_{m=-\infty}^{\infty}|I_m(q)|^2 e^{-m^2 tD_t}}{|I_0(q)|^2} + \frac{N_p-1}{N_p}
$$

$$+\frac{N_p-1}{N_p}e^{-8\pi^2q^2tD_t}\frac{\left(\sum_{m=-\infty}^{\infty}|\hat{\rho}_m(q)|^2e^{-m^2tD_r}\right)^2}{|I_0(q)|^2} \tag{3.7}$$

$$\approx 1+e^{-8\pi^2q^2tD_t}\frac{\left(\sum_{m=-\infty}^{\infty}|\hat{\rho}_m(q)|^2e^{-m^2tD_r}\right)^2}{|I_0(q)|^2}, \tag{3.8}$$

where the approximation holds when N_p is large.

Besides, considering $\boldsymbol{q}\neq\boldsymbol{q}'$ and $\boldsymbol{q}\neq-\boldsymbol{q}'$, we have:

Theorem 3.2. *Suppose Condition 2.1 and Condition 2.2 hold, and $\chi=\mathbf{1_0}$. For $q>0,q'>0$ and $\Delta\phi\neq 0$ or π, we have*

$$C(q,q',\Delta\phi,t)=N_p\sum_{\substack{m=-\infty\\ m\neq 0}}^{\infty}e^{-im\Delta\phi}I_m(q)\overline{I_m(q')}e^{-m^2tD_r}+N_p^2I_0(q)I_0(q'). \tag{3.9}$$

Remark 3.2.1. Fixing q,q',t and viewing $C(q,q',\Delta\phi,t)$ as a function of the angular coordinate $\Delta\phi$, the second term on the right hand side is merely the angular average, and the first term on the right hand side is in fact resulted from the angular average of the images. Intuitively, provided the assumption that the motions of different particles are independent with each other (Condition 2.1 (2)), the inter-particle effects vanish [35]. The main contribution to the first term arises from the effect of each individual particles. The rotational diffusion results in the decaying terms $e^{-m^2k\Delta tD_r}$, and consequently the de-correlation of the angular fluctuation of the images.

This shows why the cross-correlation C Eq. (3.9) is more powerful than the auto-correlation g_2 Eq. (2.33) in terms of estimating the rotational diffusion coefficients D_r. First, notice the rates of the multi-component exponential decay in C are determined by D_r, while the rates of the decay in g_2 depend on both D_r and the translational diffusion coefficient D_t. We also note that though both C and g_2 involve unknowns I_m in C and ρ_m in g_2 that are related to the static electron density of the particle, C is able to give substantially more data to handle those unknowns. In Chapter 4, we develop an algorithm exploiting this cross-correlation C.

We can now prove Theorem 3.1. We first prove the following lemma:

Lemma 3.1. *If Condtion 2.2 holds, then for any $q>0$, $\hat{\rho}(q,\cdot)\in A([0,2\pi])$, where $A([0,2\pi])$ is a Wiener algebra.*

Proof of Lemma 3.1. We first define

$$f(\boldsymbol{q})=-2\pi i\int_{\mathbb{R}^2}\rho(\mathbf{r})(r_2q\cos\phi-r_1q\sin\phi)e^{-2\pi i\mathbf{r}\cdot\boldsymbol{q}}d\mathbf{r}, \tag{3.10}$$

where $\boldsymbol{q} = (q, \phi)$ in polar coordinates and $\mathbf{r} = (r_1, r_2)$ in Euclidean coordinates. Since $|\mathbf{r}\rho(\mathbf{r})| \in L^1(\mathbb{R}^2) + L^2(\mathbb{R}^2)$, it is easy to verify that the integral in $f(\boldsymbol{q})$ is well-defined and $f(\boldsymbol{q})$ is continuous. According to Fubini's Theorem (Theorem A.8), for any $q > 0$, ϕ, ϕ',

$$\int_{\phi}^{\phi'} f(q,\phi)d\phi = \int_{\phi}^{\phi'} -2\pi i \int_{\mathbb{R}^2} \rho(\mathbf{r})(r_2 q\cos\phi - r_1 q\sin\phi)e^{-2\pi i\mathbf{r}\cdot\boldsymbol{q}}d\mathbf{r}d\phi \tag{3.11}$$

$$= \int_{\mathbb{R}^2} \rho(\mathbf{r}) \int_{\phi}^{\phi'} -2\pi i(r_2 q\cos\phi - r_1 q\sin\phi)e^{-2\pi i\mathbf{r}\cdot\boldsymbol{q}}d\phi d\mathbf{r} \tag{3.12}$$

$$= \int_{\mathbb{R}^2} \rho(\mathbf{r})e^{-2\pi i\mathbf{r}\cdot\boldsymbol{q}}\Big|_{(q,\phi)}^{(q,\phi')} d\mathbf{r} \tag{3.13}$$

$$= \hat{\rho}(q,\phi') - \hat{\rho}(q,\phi). \tag{3.14}$$

From the fundamental theorem of calculus, for each $q > 0$, $\hat{\rho}(q,\cdot)$ is differentiable. Thus, for each $k \in \mathbb{Z}$,

$$\hat{\rho}_m(q) = imf_m(q). \tag{3.15}$$

By Cauchy-Schwarz inequality and Parseval's Theorem for Fourier series (Theorem A.5),

$$\sum_{m=-\infty}^{\infty} = |\hat{\rho}_0(q)| + \sum_{m\neq 0} |\hat{\rho}_m(q)| \tag{3.16}$$

$$= |\hat{\rho}_0(q)| + \sum_{m\neq 0} |imf_m(q)| \tag{3.17}$$

$$\leq \|\rho(q,\cdot)\|_{L^1([0,2\pi])} + \left(\sum_{m\neq 0}\frac{1}{m^2}\right)^{\frac{1}{2}}\left(\sum_{m\neq 0}|f_m(q)|^2\right)^{\frac{1}{2}} \tag{3.18}$$

$$\leq \|\rho(q,\cdot)\|_{L^1([0,2\pi])} + \left(\sum_{m\neq 0}\frac{1}{m^2}\right)^{\frac{1}{2}}\left(\|f(q,\cdot)\|_{L^2([0,2\pi])}\right)^{\frac{1}{2}} \tag{3.19}$$

$$< \infty. \tag{3.20}$$

So $\hat{\rho}(q,\cdot) \in A([0,2\pi])$ for each $q > 0$. □

Remark 3.2.2. Given the closedness of a Wiener algebra, it is trivial to show that if $\hat{\rho}(q,\cdot) \in A([0,2\pi])$, then both $\overline{\hat{\rho}(q,\cdot)}$ and $I(q,\cdot)$ are in the same Wiener algebra, i.e. their circular harmonic series are all absolutely convergent. Thus the order of the summation and integration of their circular harmonic coefficients can be interchanged arbitrarily.

Proof of Theorem 3.1. Let $\phi' = \phi + \Delta\phi$ and $\boldsymbol{q}' = (q', \phi')$. According to Eq. (2.30), the integrand reads

$$\mathbb{E}[J(q,\phi,0)J(q',\phi',t)] = \sum_{n_1,n_2,n_3,n_4=1}^{N_p} \mathbb{E}\big[e^{-2\pi i\boldsymbol{q}\cdot(\boldsymbol{r}_{n_1}(0)-\boldsymbol{r}_{n_2}(0))}e^{-2\pi i\boldsymbol{q}'\cdot(\boldsymbol{r}_{n_3}(t)-\boldsymbol{r}_{n_4}(t))}\big]$$
$$\mathbb{E}\big[\hat{\rho}\big(q,\phi-\theta_{n_1}(0)\big)\overline{\hat{\rho}\big(q,\phi-\theta_{n_2}(0)\big)}\hat{\rho}\big(q',\phi'-\theta_{n_3}(t)\big)\overline{\hat{\rho}\big(q',\phi'-\theta_{n_4}(t)\big)}\big]. \quad (3.21)$$

We denote the terms in the above quadruple summation as $S_{n_1n_2n_3n_4}$, which we categorize into 15 types based on the equivalence between n_1, n_2, n_3, n_4:

1) When $n_1 = n_2 = n_3 = n_4$, without loss of generality, we assume that they all equal to 1, then

$$S_{1111} = \mathbb{E}\big[I\big(q,\phi-\theta_1(0)\big)I\big(q',\phi'-\theta_1(t)\big)\big] \quad (3.22)$$
$$= \sum_{m,m'=-\infty}^{\infty} I_m(q)\overline{I_{m'}(q')}e^{im\phi}e^{-im'\phi'}\mathbb{E}\big[e^{-im\theta_1(0)}e^{im'\theta_1(t)}\big] \quad (3.23)$$
$$= \sum_{m,m'=-\infty}^{\infty} I_m(q)\overline{I_{m'}(q')}e^{im\phi}e^{-im'\phi'}\mathbb{E}\big[e^{i(m'-m)\theta_1(t)}\big]\mathbb{E}\big[e^{im'(\theta_1(t)-\theta_1(0))}\big] \quad (3.24)$$
$$= \sum_{m,m'=-\infty}^{\infty} I_m(q)\overline{I_{m'}(q')}e^{im\phi}e^{-im'\phi'}\delta_{mm'}e^{-m'^2tD_r} \quad (3.25)$$
$$= \sum_{m=-\infty}^{\infty} e^{-im(\phi'-\phi)}I_m(q)\overline{I_m(q')}e^{-m^2tD_r}, \quad (3.26)$$

where I_m are circular harmonic coefficients of the intensity I.

$$\delta_{mm'} = \begin{cases} 0 & \text{if } m \neq m', \\ 1 & \text{if } m = m'. \end{cases} \quad (3.27)$$

There are N_p such terms in the summation.

2) When $n_1 = n_2 \neq n_3 = n_4$, the term becomes

$$S_{1122} = \mathbb{E}\big[I\big(q,\phi-\theta_1(\tau)\big)\big]\mathbb{E}\big[I\big(q',\phi'-\theta_1(t+\tau)\big)\big]. \quad (3.28)$$

We have

$$\mathbb{E}\big[I\big(q,\phi-\theta_1(\tau)\big)\big] = \sum_{m=-\infty}^{\infty} I_m(q)e^{im\phi}\mathbb{E}\big[e^{-im\theta_1(t)}\big] \quad (3.29)$$
$$= \sum_{m=-\infty}^{\infty} I_m(q)e^{im\phi}\mathbb{E}\big[e^{-im\theta_1(0)}\big]\mathbb{E}\big[e^{-im(\theta_1(t)-\theta_1(0))}\big] \quad (3.30)$$
$$= \sum_{m=-\infty}^{\infty} I_m(q)e^{im\phi}\delta_{0m}e^{-m^2tD_r} \quad (3.31)$$

$$= I_0(q). \tag{3.32}$$

Hence

$$S_{1122} = I_0(q)I_0(q'). \tag{3.33}$$

There are $N_p(N_p-1)$ such terms.

3) When $n_1 = n_4 \neq n_2 = n_3$, the terms can be calculated as follows:

$$\begin{aligned} S_{1221} = \mathbb{E}\big[e^{-2\pi i(\boldsymbol{q}\cdot\boldsymbol{r}_1(\tau)-\boldsymbol{q}'\cdot\boldsymbol{r}_1(t+\tau))}\big]\mathbb{E}\big[\hat{\rho}\big(q,\phi-\theta_1(\tau)\big)\overline{\hat{\rho}\big(q',\phi'-\theta_1(t+\tau)\big)}\big] \\ \mathbb{E}\big[e^{2\pi i(\boldsymbol{q}\cdot\boldsymbol{r}_1(\tau)-\boldsymbol{q}'\cdot\boldsymbol{r}_1(t+\tau))}\big]\mathbb{E}\big[\overline{\hat{\rho}\big(q,\phi-\theta_1(\tau)\big)}\hat{\rho}\big(q',\phi'-\theta_1(t+\tau)\big)\big]. \end{aligned} \tag{3.34}$$

Using the same techniques as the calculation of Eq. (3.22),

$$\mathbb{E}\big[\hat{\rho}\big(q,\phi-\theta_1(\tau)\big)\overline{\hat{\rho}\big(q',\phi'-\theta_1(t+\tau)\big)}\big] = \sum_{m=-\infty}^{\infty} e^{-im(\phi'-\phi)}\hat{\rho}_m(q)\overline{\hat{\rho}_m(q')}e^{-m^2tD_r}. \tag{3.35}$$

Also, we have

$$\begin{aligned} \mathbb{E}\big[e^{-2\pi i(\boldsymbol{q}\cdot\boldsymbol{r}_1(\tau)-\boldsymbol{q}'\cdot\boldsymbol{r}_1(t+\tau))}\big] &= \mathbb{E}\big[e^{-2\pi i\boldsymbol{q}'\cdot(\boldsymbol{r}_1(\tau)-\boldsymbol{r}_1(t+\tau))}\big]\mathbb{E}\big[e^{-2\pi i(\boldsymbol{q}-\boldsymbol{q}')\cdot\boldsymbol{r}_1(\tau)}\big] && (3.36) \\ &= \chi(2\pi|\boldsymbol{q}-\boldsymbol{q}'|)e^{-4\pi^2q^2tD_t}. && (3.37) \end{aligned}$$

According to the above three equations,

$$S_{1221} = |\chi(2\pi|\boldsymbol{q}-\boldsymbol{q}'|)|^2e^{-8\pi^2q^2tD_t}\left(\sum_{m=-\infty}^{\infty} e^{-im(\phi'-\phi)}\hat{\rho}_m(q)\overline{\hat{\rho}_m(q')}e^{-m^2tD_r}\right)^2. \tag{3.38}$$

Proceeding along the same lines, we can compute the rest of the terms. □

3.3 Convergence of Cross-correlation

Since the angular-temporal cross-correlation Eq. (3.1) is essentially an expectation over a complicated unknown joint distribution of the positions and orientations of the particles, it can not be evaluated exactly in practice. Instead, one can collect a finite amount of images, $\{J(\cdot,k\Delta t)\}_{k=0}^{K-1}$, where K is the total amount of images collected and Δt is the time difference between two consecutive images, and the cross-correlation can be approximated by the following estimator:

$$C_K(q,q',\Delta\phi,k) = \frac{1}{2\pi(K-k)}\int_0^{2\pi}\sum_{k'=0}^{K-1-k} J(q,\phi,k'\Delta t)J(q',\phi+\Delta\phi,(k+k')\Delta t)d\phi \tag{3.39}$$

which then results in introduction of statistical bias.

In this section, we prove that $C_K(q, q', \Delta\phi, k)$ is a consistent estimator of $C(q, q', \Delta\phi, k\Delta t)$, i.e. while Δt is fixed,

$$C_K(q, q', \Delta\phi, k) \xrightarrow{P} C(q, q', \Delta\phi, k\Delta t) \tag{3.40}$$

as $K \to \infty$.

Let $C(\boldsymbol{q}, \boldsymbol{q}', t)$ be the right hand side of Eq. (3.4) and

$$C_K(\boldsymbol{q}, \boldsymbol{q}', k) = \frac{1}{K-k} \sum_{k'=0}^{K-1-k} J(q, \phi, k'\Delta t) J(q', \phi', (k+k')\Delta t) \tag{3.41}$$

where $\boldsymbol{q} = (q, \phi)$ and $\boldsymbol{q}' = (q', \phi')$. Additionally, let $\mathcal{F}_t$ denote the collection of the positions and orientations of the particles before t,

$$\mathcal{F}_t = \{\boldsymbol{r}_n(\tau), \theta_n(\tau) | 0 \le \tau \le t, n = 1, 2, \cdots, N_p\}. \tag{3.42}$$

Then we prove the following theorem.

Theorem 3.3. *Assume Condition 2.1 (1-2) holds and $\mathcal{F}_0$ is known. If $\rho, |\mathbf{r}\rho(\mathbf{r})| \in L^1(\mathbb{R}^2)$, then for any $\boldsymbol{q} = (q, \phi)$, $\boldsymbol{q}' = (q', \phi')$ and any $\varepsilon > 0$, $\exists \alpha, \beta > 0$, such that*

$$\Pr\left(|C_K(\boldsymbol{q}, \boldsymbol{q}', k) - C(\boldsymbol{q}, \boldsymbol{q}', t)| \ge \varepsilon \middle| \mathcal{F}_0\right) \le \alpha e^{-\beta K \varepsilon^2}, \tag{3.43}$$

holds for any $K > k$, where α and β are two constants that do not depend on $\mathcal{F}_0$.

Since α and β do not rely on the information of $\mathcal{F}_0$, by integrating the inequality (3.43) with respect to $\mathcal{F}_0$ and the angular coordinate, the convergence of $C_K(q, q', \Delta\phi, k)$ to $C(q, q', \Delta\phi, k\Delta t)$ in probability can be established trivially.

Remark 3.3.1. Though Condition 2.1 (4) is used in the calculation of $C(\boldsymbol{q}, \boldsymbol{q}', t)$ in Section 3.2, here the initial positions and orientations are treated as constants instead of random variables, since conduction of multiple experiments with randomized initial states is sometimes not feasible. Additionally, we are usually not able to access the value of the images at the full angular range due to detector issues. Under these circumstances, Theorem 3.3 authorizes us to estimate $C(q, q', \phi, k\Delta t)$ using part of the angular data from a single conduction of the experiment.

Proof of Theorem 3.3. Here all the probability and expectation are conditional on $\mathcal{F}_0$. For the sake of simplicity, we just drop the dependence of $\mathcal{F}_0$.

Fix $\boldsymbol{q} = (q, \phi), \boldsymbol{q}' = (q', \phi')$ and k. From Lemma 3.1, we know

$$\hat{\rho}(q, \cdot), \hat{\rho}(q', \cdot), \overline{\hat{\rho}(q, \cdot)}, \overline{\hat{\rho}(q', \cdot)}, I(q, \cdot), I(q', \cdot) \in A([0, 2\pi]). \tag{3.44}$$

The absolute convergence of their circular harmonic series ensures the feasibility of all expansions of summation, the interchange of summation and expectation, and the convergence of infinite series in this proof.

Recalling Eq. (2.30),

$$C_K(\boldsymbol{q},\boldsymbol{q}',k) = \sum_{n_1,n_2,n_3,n_4=1}^{N_p} \frac{1}{K-k} \sum_{k'=0}^{K-1-k} e^{2\pi i(-\boldsymbol{q}\cdot\mathbf{r}_{n_1}(k'\Delta t)+\boldsymbol{q}\cdot\mathbf{r}_{n_2}(k'\Delta t)-\boldsymbol{q}'\cdot\mathbf{r}_{n_3}((k+k')\Delta t)+\boldsymbol{q}'\cdot\mathbf{r}_{n_4}((k+k')\Delta t)} \cdot\hat{\rho}\big(q,\phi-\theta_{n_1}(k'\Delta t)\big)\overline{\hat{\rho}\big(q,\phi-\theta_{n_2}(k'\Delta t)\big)}\hat{\rho}\big(q',\phi'-\theta_{n_3}((k+k')\Delta t)\big)\overline{\hat{\rho}\big(q',\phi'-\theta_{n_4}((k+k')\Delta t)\big)}. \tag{3.45}$$

Assume the sum of the terms with $n_1=n_2=n_3=n_4$ is $S_{1,K}$ and the sum of the rest terms is $S_{2,K}$. First we prove that

$$S_{1,K}(\boldsymbol{q},\boldsymbol{q}',k) \xrightarrow{P} N_p \sum_{m=-\infty}^{\infty} I_m(q)\overline{I_m(q')}e^{-im(\phi'-\phi)}e^{-tm^2D_r} \text{ as } K\to\infty. \tag{3.46}$$

First, we have

$$S_{1,K}(\boldsymbol{q},\boldsymbol{q}',k) = \sum_{n=1}^{N} \frac{1}{K-k} \sum_{k'=0}^{K-1-k} I(q,\phi-\theta_n(k'\Delta t))I(q',\phi'-\theta_n((k'+k)\Delta t)). \tag{3.47}$$

For each $k'=0,1,\cdots,K-1-k$ and each $n=1,\cdots,N_p$,

$$\mathbb{E}[I(q,\phi-\theta_n(k'\Delta t))I(q',\phi'-\theta_n((k'+k)\Delta t))] \tag{3.48}$$

$$=\mathbb{E}\left[\sum_{m_1,m_2=-\infty}^{\infty} I_{m_1}(q)\overline{I_{m_2}(q')}e^{im_1(\phi-\theta_n(k'\Delta t))}e^{-im_2(\phi'-\theta_n((k'+k)\Delta t))}\right] \tag{3.49}$$

$$=\sum_{m_1,m_2=-\infty}^{\infty} I_{m_1}(q)\overline{I_{m_2}(q')}e^{im_1\phi}e^{-im_2\phi'}\mathbb{E}[e^{i(m_2-m_1)\theta_n(k'\Delta t)}]\mathbb{E}[e^{im_2(\theta_n((k'+k)\Delta t)-\theta_n(k'\Delta t))}] \tag{3.50}$$

$$=\sum_{m_1,m_2=-\infty}^{\infty} I_{m_1}(q)\overline{I_{m_2}(q')}e^{i(m_1\phi-m_2\phi')}e^{-m_2^2k\Delta tD_r}e^{-(m_2-m_1)^2k'\Delta tD_r}e^{i(m_2-m_1)\theta_n(0)}. \tag{3.51}$$

Adding this up,

$$\mathbb{E}[S_{1,K}(\boldsymbol{q},\boldsymbol{q}',k)] \tag{3.52}$$

$$=\sum_{n=1}^{N_p}\sum_{m_1,m_2=-\infty}^{\infty} I_{m_1}(q)\overline{I_{m_2}(q')}e^{i(m_1\phi-m_2\phi')}e^{-m_2^2k\Delta tD_r}e^{i(m_2-m_1)\theta_n(0)}\frac{1}{K-k}\sum_{k'=0}^{K-1-k}e^{-(m_2-m_1)^2k'\Delta tD_r} \tag{3.53}$$

$$
\begin{aligned}
=&N_p \sum_{m=-\infty}^{\infty} I_m(q)\overline{I_m(q')}e^{-im(\phi'-\phi)}e^{-m^2k\Delta tD_r} \\
&+ \frac{1}{K-k}\sum_{n=1}^{N_p}\sum_{m_1\neq m_2} I_{m_1}(q)\overline{I_{m_2}(q')}e^{i(m_1\phi-m_2\phi')}e^{-m_2^2k\Delta tD_r}e^{i(m_2-m_1)\theta_n(0)}\frac{1-e^{-(m_2-m_1)^2(K-k)\Delta tD_r}}{1-e^{-(m_2-m_1)^2\Delta tD_r}}.
\end{aligned} \tag{3.54}
$$

Let $\tilde{S}_{1,K}$ be the second term in the above equality,

$$
\begin{aligned}
|\tilde{S}_{1,K}| \leq& N_p \sum_{m_1\neq m_2}^{\infty} |I_{m_1}(q)||I_{m_2}(q')|\frac{1}{K-k}\frac{1-e^{-(m_2-m_1)^2(K-k)\Delta tD_r}}{1-e^{-(m_2-m_1)^2\Delta tD_r}} &(3.55)\\
\leq& \frac{N_p}{(K-k)(1-e^{-\Delta tD_r})}\|I(q,\cdot)\|_A\|I(q',\cdot)\|_A. &(3.56)
\end{aligned}
$$

Therefore,

$$
\lim_{K\to\infty}\mathbb{E}[S_{1,K}(\boldsymbol{q},\boldsymbol{q}',k)] = N_p\sum_{m=-\infty}^{\infty} I_m(q)\overline{I_m(q')}e^{-im(\phi'-\phi)}e^{-tm^2\Delta tD_r}. \tag{3.57}
$$

Then for each $n = 1, \cdots, N$, let

$$
S_{1,K}^{(n)}(\boldsymbol{q},\boldsymbol{q}',k) = \frac{1}{K-k}\sum_{k'=0}^{K-1-k} I(q,\phi-\theta_n(k'\Delta t))I(q',\phi'-\theta_n((k'+k)\Delta t)). \tag{3.58}
$$

We now illustrate that

$$
S_{1,K}^{(n)}(\boldsymbol{q},\boldsymbol{q}',k) - \mathbb{E}[S_{1,K}^{(n)}(\boldsymbol{q},\boldsymbol{q}',k)] \xrightarrow{P} 0 \text{ as } K\to\infty. \tag{3.59}
$$

For simplicity, we drop n temporarily in some of the subscripts and superscripts and let $\theta_j = \theta_n(j\Delta t)$ for $j = 0, 1, \cdots, K-1$. Suppose that

$$
H_p = \mathbb{E}[S_{1,K}^{(n)}(\boldsymbol{q},\boldsymbol{q}',k)|\mathcal{F}_{(p-1)\Delta t}] - \mathbb{E}[S_{1,K}^{(n)}(\boldsymbol{q},\boldsymbol{q}',k)|\mathcal{F}_{p\Delta t}],\ p = 1,\cdots,K-1. \tag{3.60}
$$

It is obvious that $\{H_p\}_{p=1}^{K-1}$ is a martingale with respect to $\{\mathcal{F}_{p\Delta t}\}_{p=1}^{K-1}$ and

$$
\sum_{p=1}^{K-1} H_p = S_{1,K}^{(n)}(\boldsymbol{q},\boldsymbol{q}',k) - \mathbb{E}[S_{1,K}^{(n)}(\boldsymbol{q},\boldsymbol{q}',k)]. \tag{3.61}
$$

Then, let

$$
\begin{aligned}
H_{p,k'}^{(m_1,m_2)} = &\mathbb{E}\big[e^{i(m_2-m_1)(\theta_{k'}-\theta_0)}e^{im_2(\theta_{k+k'}-\theta_{k'})}\big|\mathcal{F}_{(p-1)\Delta t}\big] \\
&- \mathbb{E}\big[e^{i(m_2-m_1)(\theta_{k'}-\theta_0)}e^{im_2(\theta_{k+k'}-\theta_{k'})}\big|\mathcal{F}_{p\Delta t}\big].
\end{aligned} \tag{3.62}
$$

If $k' < p-k$, $|H_{p,k'}^{(m_1,m_2)}| = 0$. Considering $p-k \le k' \le p-1$, we have

$$\sum_{k'=\max\{0,p-k\}}^{\min\{p-1,K-1-k\}} \left|H_{p,k'}^{(m_1,m_2)}\right| \tag{3.63}$$

$$= \sum_{k'=\max\{0,p-k\}}^{\min\{p-1,K-1-k\}} \left|e^{i(m_2-m_1)(\theta_{k'}-\theta_0)+im_2(\theta_{p-1}-\theta_{k'})}\right| \cdot \left|\mathbb{E}\left[e^{im_2(\theta_{k'+k}-\theta_{p-1})\Delta\theta_j}\middle|\mathcal{F}_{(p-1)\Delta t}\right] - \mathbb{E}\left[e^{im_2(\theta_{k'+k}-\theta_{p-1})}\middle|\mathcal{F}_{p\Delta t}\right]\right| \tag{3.64}$$

$$= \sum_{k'=\max\{0,p-k\}}^{\min\{p-1,K-1-k\}} \left|\mathbb{E}\left[e^{im_2(\theta_{k+k'}-\theta_{p-1})}\right] - e^{im_2(\theta_p-\theta_{p-1})}\mathbb{E}\left[e^{im_2(\theta_{k+k'}-\theta_p)}\right]\right| \tag{3.65}$$

$$\le \left|e^{-m_2^2\Delta tD_r} - e^{im_2(\theta_p-\theta_{p-1})}\right| \sum_{k'=0}^{k-2} e^{-m_2^2k'\Delta tD_r} \tag{3.66}$$

$$\le \frac{2}{1-e^{-\Delta tD_r}}, \tag{3.67}$$

and when considering $k' \ge p$,

$$\sum_{k'=p}^{K-1-k} \left|H_{p.k'}^{(m_1,m_2)}\right| \tag{3.68}$$

$$= \sum_{k'=p}^{K-1-k} \left|e^{i(m_2-m_1)(\theta_{p-1}-\theta_0)}\right| \cdot \left|\mathbb{E}\left[e^{im_2(\theta_{k+k'}-\theta_{k'})j}\right]\right| \cdot \left|\mathbb{E}\left[e^{i(m_2-m_1)(\theta_{k'}-\theta_{p-1})}\middle|\mathcal{F}_{(p-1)\Delta t}\right] - \mathbb{E}\left[e^{i(m_2-m_1)(\theta_{k'}-\theta_{p-1})}\middle|\mathcal{F}_{p\Delta t}\right]\right| \tag{3.69}$$

$$= \sum_{k'=p}^{K-1-k} e^{-m_2^2k\Delta tD_r}\left|\mathbb{E}\left[e^{i(m_2-m_1)(\theta_{k'}-\theta_{p-1})}\right] - e^{i(m_2-m_1)(\theta_p-\theta_{p-1})}\mathbb{E}\left[e^{i(m_2-m_1)(\theta_{k'}-\theta_p)}\right]\right| \tag{3.70}$$

$$\le \left|e^{-(m_2-m_1)^2\Delta tD_r} - e^{i(m_2-m_1)\Delta\theta_p}\right| \sum_{k'=0}^{K-2-k-p} e^{-(m_2-m_1)^2\Delta tD_r} \tag{3.71}$$

$$\le \frac{2}{1-e^{-\Delta tD_r}}. \tag{3.72}$$

Hence,

$$\sum_{k'=0}^{K-1-k} \left|H_{p,k'}^{(m_1,m_2)}\right| = \sum_{k'=0}^{p-k} \left|H_{p,k'}^{(m_1,m_2)}\right| + \sum_{k'=\max\{0,p-k\}}^{\min\{p-1,K-1-k\}} \left|H_{p,k'}^{(m_1,m_2)}\right| + \sum_{k'=p}^{K-1-k} \left|H_{p.k'}^{(m_1,m_2)}\right| \tag{3.73}$$

$$\le \frac{4}{1-e^{-\Delta tD_r}}. \tag{3.74}$$

Then for each $p = 1, \cdots, N-1$,

$$|H_p| \leq \frac{1}{K-k} \sum_{m_1,m_2=-\infty}^{\infty} |I_{m_1}(q)| \cdot |I_{m_2}(q')| \cdot \left|e^{i(m_1\phi - m_2\phi' + (m_2-m_1)\theta_n(0))}\right| \cdot \left| \sum_{k'=0}^{K-1-k} H_{p,k'}^{(m_1,m_2)} \right| \tag{3.75}$$

$$\leq \frac{4}{(K-k)(1-e^{-\Delta t D_r})} \|I(q,\cdot)\|_A \|I(q,\cdot)\|_A. \tag{3.76}$$

Applying the Azuma-Hoeffding inequality (Theorem A.7), for all $\varepsilon > 0$, we have

$$\mathrm{P}(|S_{1,K}^{(n)}(\boldsymbol{q},\boldsymbol{q}',k) - \mathbb{E}[S_{1,K}^{(n)}(\boldsymbol{q},\boldsymbol{q}',k)]| > \varepsilon) \leq 2\exp\left(\frac{-(K-k)^2(1-e^{-\Delta t D_r})^2\varepsilon^2}{32K\|I(q,\cdot)\|_A^2\|I(q,\cdot)\|_A^2}\right). \tag{3.77}$$

Since this limit holds for $n = 1, \cdots, N_p$ and

$$S_{1,K}(\boldsymbol{q},\boldsymbol{q}',k) = \sum_{n=1}^{N_p} S_{1,K}^{(n)}(\boldsymbol{q},\boldsymbol{q}',k), \tag{3.78}$$

we know that for $\forall \varepsilon > 0, N > 0$, $\exists \alpha > 0, \beta > 0$ such that

$$\mathrm{P}(|S_{1,K}(\boldsymbol{q},\boldsymbol{q}',k) - \mathbb{E}[S_{1,K}(\boldsymbol{q},\boldsymbol{q}',k)]| > \varepsilon) \leq \alpha e^{-\beta N\varepsilon^2}. \tag{3.79}$$

A similar tail bound of $S_{2,K}(\boldsymbol{q},\boldsymbol{q}',k)$ can be obtain along similar procedure. The derivation of this theorem is then straightforward. □

In the above proof, the time difference Δt is fixed while K is increasing, which implies the total duration of the experiment $K\Delta t$ is increasing as well. If we fix the duration $K\Delta t = T$, then increase the number of images collected K, i.e. collect the images more frequently, the desired conclusion can not be obtained. Under this assumption that $\Delta t = T/K$ and $k = t/\Delta t$ where t is fixed, the right hand side of the inequality (3.54) contains a factor whose limit is non-zero,

$$\lim_{K\to\infty} \frac{1}{K-k} \frac{1-e^{-(m_2-m_1)^2(K-k)TD_r/K}}{1-e^{-(m_2-m_1)^2TD_r/K}} = \frac{1-e^{-(m_2-m_1)^2(T-t)D_r}}{(m_2-m_1)^2(T-t)D_r}, \tag{3.80}$$

for $m_1 \neq m_2$, and thus it can be proved that the bias of C_K is asymptotically proportional to $\frac{1}{T}$ as $T \to \infty$,

$$\mathbb{E}[C_K(\boldsymbol{q},\boldsymbol{q}',k)] - C(\boldsymbol{q},\boldsymbol{q}',k\Delta t) = \mathcal{O}\left(\frac{1}{T}\right), \tag{3.81}$$

which suggests that more frequent collection of images without extending the total duration of experiments will not help obtain better estimates. In other words, collecting more images over the same time period will not converge to a better estimate, due to the non-zero limit above.

On the other hand, as D_r becomes larger, both the bounds Eq. (3.56) and Eq. (3.77) become tighter. In fact, the larger the D_r and D_t, the tighter the bounds of C_K. Indeed, faster motions of the particles can be viewed intuitively as longer duration of the experiments, which as claimed by our previous discussion, results in more accurate estimates of the angular-temporal cross-correlation.

Chapter 4

Numerical Algorithm for Estimating the Rotational Diffusion Coefficient

In practice, the domain is usually large enough and with smooth boundary, so that the characteristic function χ can be viewed as the indicator function $\mathbf{1_0}$. Since the electron density ρ is real, and following Friedel's law (Theorem A.4), one can prove that the intensity I is symmetric, i.e. $I(\boldsymbol{q}) = I(-\boldsymbol{q})$, and hence $I_m = 0$ for any odd m. Then Eq. (3.9) becomes

$$C(q, q', \Delta\phi, t) = N_p \sum_{\substack{m=-\infty \\ m\neq 0}}^{\infty} e^{-i2m\Delta\phi} I_{2m}(q)\overline{I_{2m}(q')} e^{-4m^2 t D_r} + N_p^2 I_0(q) I_0(q'). \tag{4.1}$$

In this chapter, we construct a mathematical algorithm, which we call "Multi-tiered Estimation for Correlation Spectroscopy (MTECS)", for estimating the rotational diffusion coefficient D_r from the angular-temporal cross-correlation Eq. (3.9), given in the first term on the right-hand-side of the above equation. (The second term on the right-hand-side is the angular average of the cross-correlation.) The first term, denoted as $\tilde{C}(q, q', \Delta\phi, t)$, is essentially the correlation of the angular fluctuation of the images, and can be estimated by

$$\tilde{C}(q, q', \Delta\phi, k\Delta t) = C(q, q', \Delta\phi, k\Delta t) - \langle J(q, \phi, \tau)\rangle \cdot \langle J(q', \phi, \tau)\rangle \tag{4.2}$$

$$\approx \frac{1}{2\pi(N_{sp}-k)} \int_0^{2\pi} \sum_{k'=0}^{N_{sp}-1-k} J(q, \phi, k'\Delta t) J(q', \phi+\Delta\phi, (k+k')\Delta t) d\phi \tag{4.3}$$

$$- \left(\frac{1}{2\pi N_{sp}} \sum_{k=0}^{N_{sp}-1} \int_0^{2\pi} J(q, \phi, k\Delta t) d\phi\right) \left(\frac{1}{2\pi N_{sp}} \sum_{k=0}^{N_{sp}-1} \int_0^{2\pi} J(q', \phi, k\Delta t) d\phi\right). \tag{4.4}$$

where the subtraction of the second term above can be replaced by subtracting the angular average from each images beforehand. Here we assume:

Condition 4.1. *ρ is not isotropic. The support of ρ is bounded.*

In the above condition, the former one implies that the reorientation of particles will result in the variation of the images J. Such assumption is required by our algorithm, because an isotropic ρ makes $\tilde{C}$ constantly zero so that the rotation of the particles can not be detected from the cross-correlation. The latter holds naturally for any realistic electron density ρ. Let L be an upper bound of the diameter of the support. This is the only prior knowledge that is necessary to the MTECS algorithm.

Assuming that the above function is discretely approximated at $q, q' \in \{q_j\}_{j=1}^{N_q}$, $\Delta\phi \in \{\Delta\phi_j\}_{j=1}^{N_\phi}$, and $t \in \{k\Delta t\}_{k=0}^{K-1}$, this gives rise to a 4-way data tensor $\mathcal{C} \in \mathbb{R}^{N_q \times N_q \times N_\phi \times K}$ whose entries are

$$\mathcal{C}_{ii'jk} = \tilde{C}(q_i, q_{i'}, \Delta\phi_j, k\Delta t) = N_p \sum_{\substack{m=-\infty \\ m\neq 0}}^{\infty} e^{-i2m\Delta\phi} I_{2m}(q_i)\overline{I_{2m}(q_{i'})} e^{-4m^2 k\Delta t D_r}, \tag{4.5}$$

where the constant N_p is omitted hereafter since it is irrelevant to the construction and execution of the algorithm and thus does not have to be determined.

Taking the data tensor $\mathcal{C}$ as input, the MTECS algorithm estimates the rotational diffusion coefficient D_r by following the multi-tiered iterative projection (M-TIP) approach which decomposes the complex optimization into subparts whose solutions can be either obtained directly or approximated through computationally efficient iterative solvers. This avoids solving a high-dimensional non-convex optimization directly, narrowing down the non-convex part to relatively lower dimensional space. Each of the subparts enforces a constraint originating from the underlying theoretical model describing the input data Eq. (4.5), and together are combined into an iteration, which is applied repeatedly to find a form that is close to the data while obeying the mathematical characterization.

The flowchart Figure 4.1 sketches the procedure of the MTECS algorithm. In Section 4.1-4.4, we introduce the subparts throughly. In Section 4.5, we give an overview of the MTECS algorithm and provide other algorithmic details.

We will use the similar notations of tensors as in [21, 22]. The $(i_1, i_2, \cdots, i_n)-$th entry of an n-way tensor $\mathcal{X} \in \mathbb{C}^{I_1 \times I_2 \times \cdots \times I_n}$ is denoted as $\mathcal{X}_{i_1 i_2 \cdots i_n}$. The subarrays of $\mathcal{X}$ are identified by fixing a subset of the indices while varying the others, which are labeled by MATLAB-style notations, i.e. replacing the varying subscripts by colons. For example, $\mathcal{X}_{:i_2\cdots i_n}$ is a vector obtained by varying the first index, $\mathcal{X}_{i_1::i_4\cdots i_n}$ indicates a matrix formed by varying the second and the third indices, and $\mathcal{X}_{i_1:\cdots:}$ is an $(n-1)$-way tensor. The Frobenious norm of the tensor $\mathcal{X}$ is defined as

$$\|\mathcal{X}\|_F = \sqrt{\sum_{i_1=1}^{I_1}\sum_{i_2=1}^{I_2}\cdots\sum_{i_n=1}^{I_n} |\mathcal{X}_{i_1\cdots i_n}|^2}. \tag{4.6}$$

We say $\mathcal{X}$ is rank one if there exists vectors $x^{(1)} \in \mathcal{C}^{I_1}, x^{(2)} \in \mathcal{C}^{I_2}, \cdots, x^{(n)} \in \mathcal{C}^{I_n}$ such that $\mathcal{X}$

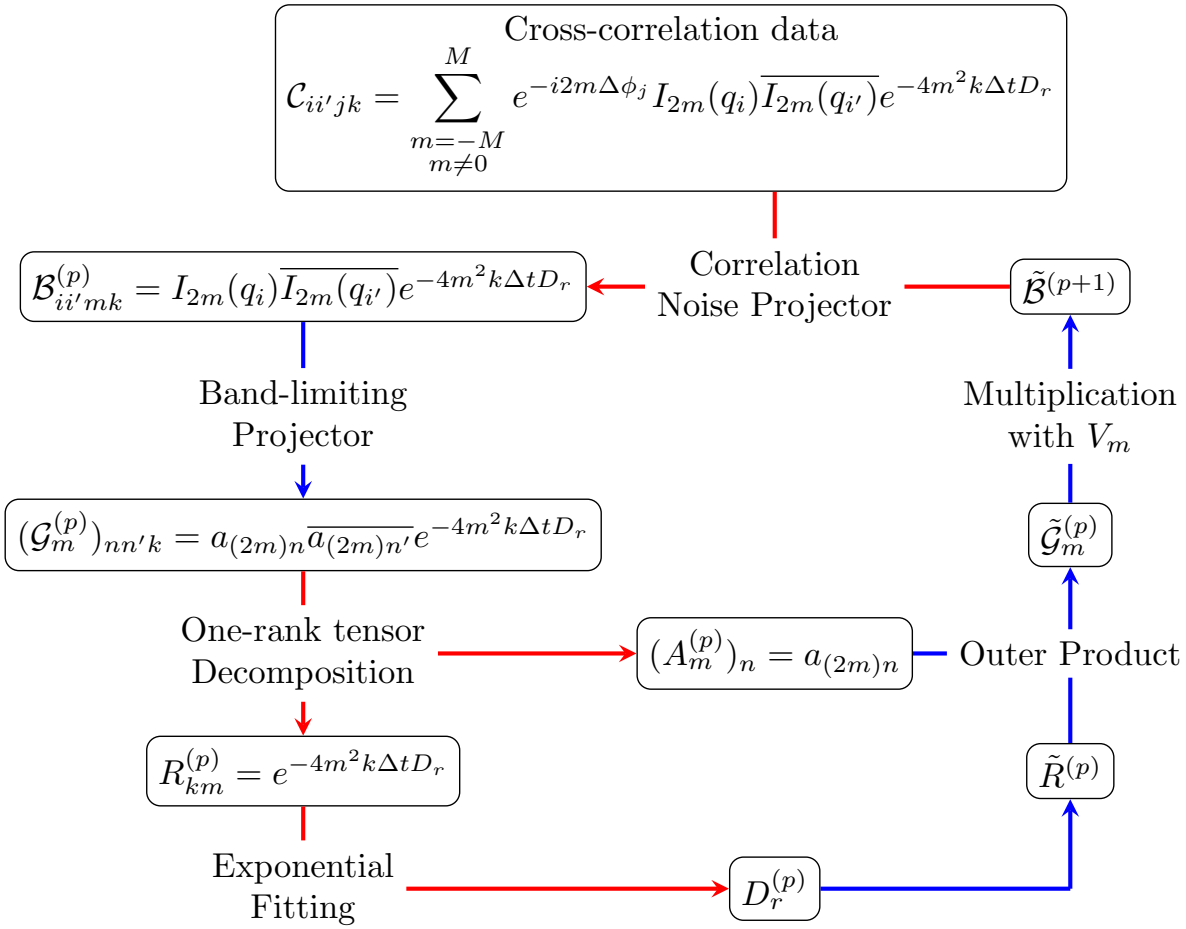

Figure 4.1: Flowchart of the MTECS algorithm. The blue arrows represent the subparts that can be computed exactly, and the red arrows stand for the subparts whose solutions can only be approximated iteratively. See the following subsections for more detailed description of the subparts and equations.

can be represented as their outer product,

$$\mathcal{X} = x^{(1)} \otimes x^{(2)} \otimes \cdots \otimes x^{(n)}, \Longleftrightarrow \mathcal{X}_{i_1 i_2 \cdots i_n} = x^{(1)}_{i_1} x^{(2)}_{i_2} \cdots x^{(n)}_{i_n}. \tag{4.7}$$

4.1 Correlation Noise Projector

Here we construct the correlation noise projector P_C which finds the Fourier components of the cross-correlation data by utilizing the fact that the cross-correlation can be approximated by a finite amount of terms in Eq. (4.5). We first truncate the infinite summation in Eq. (4.5) to the first finite terms

$$\mathcal{C}_{ii'jk} = N_p \sum_{\substack{m=-M \\ m\neq 0}}^{M} e^{-i2m\Delta\phi} I_{2m}(q_i)\overline{I_{2m}(q_{i'})} e^{-4m^2 k\Delta t D_r}. \tag{4.8}$$

which can be written in terms of matrix-vector multiplication as

$$C_{ii':k} = E \cdot \mathcal{B}_{ii':k}, \tag{4.9}$$

where the entries of $E \in \mathbb{C}^{N_\phi \times 2M}$ and $\mathcal{B} \in \mathbb{C}^{N_q \times N_q \times 2M \times K}$ are

$$\mathcal{B}_{ii'mk} = I_{2m}(q)\overline{I_{2m}(q')} e^{-4m^2 k\Delta t D_r}, \tag{4.10}$$

$$E_{jm} = e^{-i2m\Delta\phi_j}. \tag{4.11}$$

A good heuristic choice of M is proportional to $\pi L q_{\max}$, which is based on the number of Shannon elements within the measured q range. Seeing that the matrix E can be calculated explicitly, Eq. (4.9) is an overdetermined linear system.

Remark 4.1.1. Though Eq. (4.8) is the Fourier series of the function $\tilde{C}(q_i, q_{i'}, \cdot, k\Delta t)$ with respect to the third argument, the coefficients $\mathcal{B}_{ii':k}$ cannot be computed through Eq. (2.7), owing to the fact that we are not able to access the value of $\tilde{C}(q_i, q_{i'}, \cdot, k\Delta t)$ over the whole angular range $[0, 2\pi)$. This is caused by the necessary assumption, $\Delta\phi \neq 0$ and $\Delta\phi \neq \pi$, which is required by Theorem 3.2: violating this assumption leads to the peaks at $\Delta\phi = 0$ and $\Delta\phi = \pi$ (See the analysis in the Section 3.2 and Figure 5.3). In practice, detector malfunction may also result in that the angular range $[0, 2\pi)$ cannot be fully accessed.

To solve the linear system Eq. (4.9), we formulate the correlation noise projector through a Tikhonov regularization with Morozov's discrepancy [36]. Given the current guess of $\mathcal{B}$, the projector P_C calculates

$$P_C\mathcal{B} = \mathcal{B} + \Delta\mathcal{B}, \tag{4.12}$$

where for each k, $\Delta\mathcal{B}_{:::k}$ solves

$$\min_{\Delta\mathcal{B}_{:::k}\in\mathbb{C}^{N_q\times N_q\times 2M}} \sum_{i,i'=1}^{N_q} \|\Delta\mathcal{B}_{ii':k}\|^2 q_i q_{i'}, \tag{4.13}$$

$$\text{s.t. } \frac{1}{N_\phi N_q^2}\sum_{i,i'=1}^{N_q}\frac{1}{\sigma_{ii'k}^2}\|\mathcal{C}_{ii':k} - E\cdot(\mathcal{B}_{ii':k}+\Delta\mathcal{B}_{ii':k})\|^2 \le \tau_k, \tag{4.14}$$

where $\sigma_{ii'k}$ are scaling parameters and τ_k is a fitting parameter indicating the strength of the constraint. The $q_iq_{i'}$ factor in the objective function results from the q factor in the orthogonality of the basis function Eq. (4.29) (See Eq. (4.35)). In principle, the projector P_C seeks the minimal perturbation of the current guess of $\mathcal{B}$ to make the cross-correlation corresponding to the updated $\mathcal{B}$ within the range weighted and specified by $\sigma_{ii'k}$ and τ_k from the data. The effect of the projector P_C is greatly influenced by the choice of τ_k. Small τ_k imposes tighter constraints so that the updated cross-correlation is closer to data, leading to potential absorption of noise, while large values of τ_k have the tendency to oversmooth the solution. The selection of the $\sigma_{ii'k}$ and τ_k will be described later.

By rescaling and vectorizing the tensors, the above optimization problem can be rewritten as

$$\min_{\Delta\overline{B}\in\mathbb{C}^{2N_q^2M}} \|\Delta\overline{B}\|^2, \tag{4.15}$$

$$\text{s.t. } \|\overline{C} - \overline{E}\cdot\Delta\overline{B}\|^2 \le \tau_k, \tag{4.16}$$

where $\overline{C}\in\mathbb{R}^{N_q^2N_\phi}$ and $\overline{E}\in\mathbb{C}^{N_q^2N_\phi\times 2N_q^2M}$. This optimization is equivalent to Tikhonov regularization with Morozov's discrepancy [36], which can be solved by finding

$$\Delta\overline{B}(\lambda) = (\overline{E}^*\overline{E} + \lambda I)^{-1}\overline{C} \tag{4.17}$$

satisfying

$$\|\overline{C} - \overline{E}\Delta\overline{B}(\lambda)\|^2 = \tau_k. \tag{4.18}$$

In [19], it is shown that the left hand side of Eq. (4.18) is a monotonic function of λ, which in our implementation Eq. (4.18) was solved by the Newton–Raphson method coupled with the bisection method when the bound constraints are violated.

We select the parameter $\sigma_{ii'k}$ and τ_k following the approach outlined in [39]. The parameter $\sigma_{ii'k}$ are chosen by how well the mathematical model describes the cross-correlation data $\mathcal{C}$. Specifically, we calculate the full singular value decomposition of E,

$$\begin{aligned} E &= \mathcal{U}_C\Lambda_C\mathcal{V}_C^*, \\ \mathcal{U}_C &= [\mathcal{U}_{C1}, \mathcal{U}_{C2}], \end{aligned} \tag{4.19}$$

where $\mathcal{U}_{C1}$ consists of the first $2M$ columns of $\mathcal{U}_C$, and the remaining $N_\phi - 2M$ columns form $\mathcal{U}_{C2}$. Then we select

$$\sigma^2_{ii'k} = \frac{\|\mathcal{U}^*_{C2}\mathcal{C}_{ii':k}\|^2}{N_\phi - 2M}, \tag{4.20}$$

which in fact is an estimation of the inconsistency between the cross-correlation data $\mathcal{C}_{ii':k}$ and Eq. (4.8). As for τ_k, a good heuristic is

$$\tau_k = \left(1 + \frac{2}{N_\phi - 2M - 2}\right)\left(1 - \frac{2M(\|\overline{C}\|^2 - 1)}{N_\phi(\|\overline{C}\|^2 - 1) + 2M}\right). \tag{4.21}$$

where the first term is based on Chi-square distribution statistics and the second one is based on the estimated magnitude of errors.

According to Eq. (4.10) and the fact that I is real, we know theoretically

$$\mathcal{B}_{ii'mk} = \overline{\mathcal{B}_{ii'(-m)k}}. \tag{4.22}$$

Such conjugacy could be enforced after the correlation noise projector P_C by

$$\mathcal{B}_{ii'mk} \coloneqq \frac{1}{2}(\mathcal{B}_{ii'mk} + \overline{\mathcal{B}_{ii'(-m)k}}), \tag{4.23}$$

and input only the part of $\mathcal{B}$ associating with $m > 0$ to the following subparts, so as to accelerate the computation.

4.2 Band-limiting Projector

In this section, we develop the band-limiting projector which acts on the tensor $\mathcal{B}$ given by the correlation noise projector P_C to remove high frequency noise through a basis expansion of the circular harmonic coefficients I_m.

The density-density autocorrelation function is defined as

$$A(\boldsymbol{r}) = \int_{\mathbb{R}^2} \rho(\boldsymbol{r} + \boldsymbol{r}')\rho(\boldsymbol{r}')d\boldsymbol{r}', \tag{4.24}$$

whose circular harmonic coefficient $A_m(r)$ is supported on $[0, L]$, and thus can be represented through a Fourier-Bessel series

$$A_m(r) = \sum_{n=1}^{\infty} a_{mn} \frac{\sqrt{2}J_m\left(\frac{u_{mn}}{L}r\right)}{LJ_{m+1}(u_{mn})}. \tag{4.25}$$

Notice that we don't need L to be precisely determined: it is only required to be larger than the true value of the diameter to ensure the convergence of Eq. (4.30).

Since the Fourier transform of $A(\boldsymbol{r})$ is $I(\boldsymbol{q})$ (Theorem A.3), the circular harmonic coefficient I_m can be obtained by the Hankel transform of A_m,

$$I_m(q) = 2\pi(-1)^m \int_0^L A_m(r) J_m(2\pi q r) r dr. \tag{4.26}$$

Combining Eq. (4.25) and Eq. (4.26) gives

$$I_m(q) = \sum_{n=1}^{\infty} a_{mn} \frac{2\sqrt{2}\pi(-1)^m}{L J_{m+1}(u_{m,n})} \int_0^L J_m\left(\frac{u_{mn}}{L} r\right) J_m(2\pi q r) r dr \tag{4.27}$$

$$= \sum_{n=1}^{\infty} a_{mn} \frac{2\sqrt{2}\pi(-1)^m L u_{mn} J_m(2\pi q L)}{u_{mn}^2 - (2\pi q L)^2}. \tag{4.28}$$

Then letting

$$v_{mn}(q) = \begin{cases} \sqrt{2}\pi(-1)^m L J_{m+1}(u_{mn}) & \text{if } q = \dfrac{u_{mn}}{2\pi L} \\ \dfrac{2\sqrt{2}\pi(-1)^m L u_{mn} J_m(2\pi q L)}{u_{mn}^2 - (2\pi q L)^2} & \text{otherwise,} \end{cases} \tag{4.29}$$

we derive an basis expansion of the circular harmonic coefficients of the intensity I,

$$I_m(q) = \sum_{n=1}^{\infty} a_{mn} v_{mn}(q). \tag{4.30}$$

A special property of the set of basis functions v_{mn} is that its mass concentrates around $q = \frac{u_{mn}}{2\pi L}$ (See Figure 4.2), which implies that it is practicable to take truncation of Eq. (4.30) based on the number of terms whose majority of mass is within the measured q range. We truncated the series Eq. (4.30) to the first N_m terms as N_m is chosen as the maximal n such that

$$\frac{u_{mn}}{2\pi L} \leq \alpha q_{\max}. \tag{4.31}$$

where q_{max} is the maximum of the measure-q grid $\{q_i\}_{i=1}^{N_q}$ and α is a hyperparameter.

Combining Eq. (4.10) and Eq. (4.30), we have

$$\mathcal{B}_{::mk} = V_m (\mathcal{G}_m)_{::k} V_m^*, \tag{4.32}$$

where

$$(V_m)_{in} = v_{(2m)n}(q_i), \ \ (\mathcal{G}_m)_{nn'k} = a_{(2m)n} \overline{a_{(2m)n'}} e^{-4m^2 k \Delta t D_r}. \tag{4.33}$$

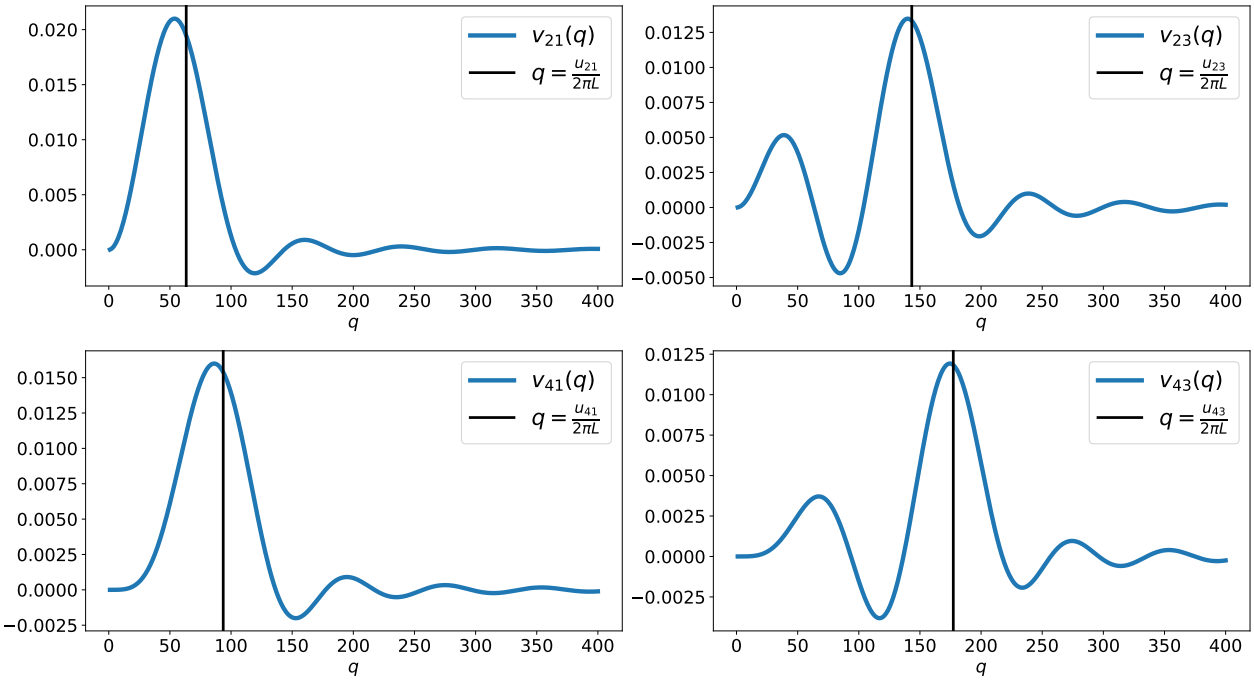

Figure 4.2: Examples of the band-limiting basis functions v_{mn}. The black vertical bar represents positions of values of associated $\frac{u_{mn}}{2\pi L}$.

Since the matrices V_m as well as their pseudoinverses $V_m^\dagger$ can be computed explicitly, we define the band-limiting projector to solve Eq. (4.32) for $\mathcal{G}_m$ as

$$(\mathcal{G}_m)_{::k} = V_m^\dagger \mathcal{B}_{::mk} V_m^{\dagger *}. \tag{4.34}$$

According to Theorem A.6 and orthogonality of the Fourier-Bessel series, the basis functions v_{mn} are orthogonal to each other in the sense that

$$\int_0^\infty v_{mn}(q) v_{mn'}(q) q dq = \delta_{nn'}. \tag{4.35}$$

Therefore, prior to computation of the pseudoinverse $V_m^\dagger$, we weight V_m by multiplying the n-th row by $\sqrt{q_n d_n}$ with $d_n = \frac{q_{n+1} - q_{n-1}}{2}$. This weighted V_m is denoted by $\overline{V}_m$. We calculate the singular value decomposition of $\overline{V}_m$,

$$\overline{V}_m = \mathcal{U}_B \Lambda_B \mathcal{V}_B^*, \tag{4.36}$$

and then the pseudoinverse of $\overline{V}_m$ as

$$\overline{V}_m^\dagger = \mathcal{V}_B \Lambda_B^{\text{inv}} \mathcal{U}_B^*, \tag{4.37}$$

where Λ_B^{inv} is a diagonal matrix with diagonal entries

$$(\Lambda_B^{\text{inv}})_{nn} = \begin{cases} \frac{1}{(\Lambda_B)_{nn}} & \text{if } (\Lambda_B)_{nn} \geq \beta(\Lambda_B)_{11}, \\ 0 & \text{if } (\Lambda_B)_{nn} < \beta(\Lambda_B)_{11}. \end{cases} \tag{4.38}$$

The pseudoinverse $V_m^\dagger$ is attained by dividing the n-th column of $\overline{V}_m^\dagger$ by $\sqrt{q_n d_n}$.

4.3 Rank-one Tensor Decomposition

Next, we obtain the coefficients $a_{(2m)n}$ and the term $e^{-4m^2k\Delta t D_r}$. According to Eq. (4.33), for each m, the tensor $\mathcal{G}_m \in \mathbb{C}^{N_m \times N_m \times K}$ can be viewed as an outer product:

$$\mathcal{G}_m = A_m \otimes \overline{A_m} \otimes R_{:m}, \tag{4.39}$$

where

$$(A_m)_n = a_{(2m)n}, \ R_{km} = e^{-4m^2k\Delta t D_r}. \tag{4.40}$$

The above equation implies that $\mathcal{G}_m$ is at most rank one. Relying on this, A_m and $R_{:m}$ can be retrieved using a weighted partially-Hermitian bound-constrained rank-one tensor decomposition:

$$\min_{A_m \in \mathbb{C}^{N_m}, R_{:m} \in \mathbb{R}^K} \sum_{k=0}^{K-1} (\omega_{td})_k \|(\mathcal{G}_m)_{::k} - R_{km} A_m A_m^*\|_F^2, \tag{4.41}$$

$$\text{s.t. } R_{0m} = 1, \ 0 \leq R_{km} \leq 1 \text{ for each } k, \tag{4.42}$$

where ω_{td} are weights, and $\|\cdot\|_F$ is the Frobenius norm. We express this subpart briefly as

$$[\![A_m; R_{:m}]\!] = P_O \mathcal{G}_m, \text{ for each } m. \tag{4.43}$$

The purpose of the weights ω_{td} is to balance the exponentially-decaying signal and the noise whose magnitude remains the same with respect to different k. If K or D_r is quite large, the unweighted tensor decomposition Eq. (4.41) tends to pick up the noise instead of true signal. A reasonable choice of ω_{td} is based on the decaying terms $e^{-4m^2k\Delta t D_r}$ where D_r is the current estimation.

The above problem can be solved by modified alternating least square [6, 16]. In particular, we initialize $R_{0m} = 1$ and let $R_{km}, k \in [1, K-1] \cap \mathbb{Z}$ independently and identically distributed uniformly on $[0, 1]$. Then the A_m-subproblem and $R_{:m}$-subproblem are solved iteratively:

- The A_m-subproblem is equivalent to

$$\min_{A_m \in \mathbb{C}^{N_m}} \left\| \frac{1}{\|w_{td} \circ R_{:m}\|^2} \sum_{k=0}^{K-1} (w_{td})^2 R_{km} \mathcal{G}_{::k} - A_m A_m^* \right\|_F^2 \tag{4.44}$$

  where $\circ$ is the element-wise multiplication. The solution to the above minimization is $A_m = \lambda_0 v_0$ where λ_0 is the largest positive eigenvalue and v_0 is the corresponding eigenvector of the matrix

$$\frac{1}{\|w_{td} \circ R_{:m}\|^2} \sum_{k=0}^{K-1} (w_{td})^2 R_{km} \mathcal{G}_{::k}. \tag{4.45}$$

- The $R_{:m}$-subproblem can be solved element-wisely, for each $k > 0$

$$\min_{0 \le R_{km} \le 1} \|\mathcal{G}_{::k} - R_{km} A_m A_m^*\|_F^2. \tag{4.46}$$

  The solution to the above minimization is

$$R_{km} = P_{[0,1]} \left(\frac{\Re(A_m^* \mathcal{G}_{::k} A_m)}{\|A_m\|^4} \right), \tag{4.47}$$

  where $P_{[0,1]}$ projects any real number to $[0, 1]$,

$$P_{[0,1]}(x) = \begin{cases} 0 & \text{if } x < 0, \\ x & \text{if } 0 \le x \le 1, \\ 1 & \text{if } x > 1. \end{cases} \tag{4.48}$$

The uniqueness of optimal A_m is up to a complex factor. Therefore, we stop the iterations when value of difference between the values of the objective function Eq. (4.41) at two consecutive iterations are smaller than a tolerance.

Remark 4.3.1. The best method for computing partially-symmetric tensor rank decomposition, for instance,

$$\mathcal{X} \approx \sum_{r=1}^{R} A_{:r} \otimes A_{:r} \otimes C_{:r}, \tag{4.49}$$

which is called individual differences in scaling (INDSCAL), is still an open problem. One widely-used method is to treat two A matrices as distinct factors A and A', and then update them separately through the conventional alternating least square and enforce $A = A'$ at the end of iterations. Here we select a different strategy which is to impose the conjugacy (symmetry) directly through the eigenvalue decomposition (A_m-subproblem), though eigenvalue decomposition is usually computationally expensive, since the size of the matrix Eq. (4.45), $N_m \times N_m$, is not large.

4.4 Exponential Fitting

Once the matrix R of decaying terms $e^{-4m^2k\Delta t D_r}$ is computed, we are able to estimate the rotational diffusion coefficient D_r by solving the following minization:

$$x_{min} = \underset{0<x<1}{\operatorname{argmin}} \sum_{k=1}^{K-1} \sum_{\substack{m=-M \\ m\neq=0}}^{M} \omega_m (R_{km} - x^{4m^2k})^2, \tag{4.50}$$

and then letting

$$D_r = -\frac{\log x_{min}}{\Delta t}. \tag{4.51}$$

If the magnitudes of I_m are too close to zero for some m, which happens when the particles possess unknown radial symmetry, then $R_{:m}$ could be too noisy for these m. To deal with this situation, the algorithm allows assigning the weights ω_m according to the estimated magnitude of I_m, e.g. $\omega_m = \|V_m A_m\|^2$. This subpart is denoted by

$$P_E R = D_r. \tag{4.52}$$

4.5 MTECS Algorithm

We now assemble the subparts described in the previous subsections to give an iterative algorithm, MTECS (See Figure 4.1 for the flowchart). With initialization $\tilde{\mathcal{B}}^{(0)} = \mathbf{0}$ and $p = 0$, the algorithm consists of the following steps:

Step 1: Given the cross-correlation $\mathcal{C}$, apply the correlation noise projector to compute $\mathcal{B}^{(p)} = P_C \tilde{\mathcal{B}}^{(p)}$;

Step 2: Enforce the conjugacy by $\mathcal{B}^{(p)}_{::m:} \coloneqq \frac{1}{2}(\mathcal{B}^{(p)}_{::m:} + \overline{\mathcal{B}^{(p)}_{::(-m):}})$ for $m \in [1, M] \cap \mathbb{Z}$;

Step 3: For $m \in [1, M] \cap \mathbb{Z}$, compute $(\mathcal{G}^{(p)}_m)_{::k} = V_m^{\dagger} \mathcal{B}^{(p)} V_m^{\dagger *}$ by performing the band-limiting projector for $k \in [0, K-1] \cap \mathbb{Z}$;

Step 4: Compute the rank-one tensor decomposition $P_O \mathcal{G}^{(p)}_m = [\![A^{(p)}_m; R^{(p)}_{:m}]\!]$ for $m \in [1, M] \cap \mathbb{Z}$;

Step 5: Make an current estimation of the rotational diffusion coefficient as $D_r^{(p)} = P_E R^{(p)}$;

Step 6: Form an updated matrix of the decay terms whose entries are $\tilde{R}^{(p)}_{km} = e^{-4m^2k\Delta t D_r^{(p)}}$ for $m \in [1, M] \cap \mathbb{Z}$ and $k \in [0, K-1] \cap \mathbb{Z}$;

Step 7: For $m \in [1, M] \cap \mathbb{Z}$, obtain the tensors $\tilde{\mathcal{G}}_m^{(p)} = A_m^{(p)} \otimes \overline{A_m^{(p)}} \otimes \tilde{R}_{:m}^{(p)}$;

Step 8: Update the tensor $\tilde{\mathcal{B}}^{(p+1)}$ by calculating $\tilde{\mathcal{B}}_{::mk}^{(p+1)} = V_m(\tilde{\mathcal{G}}_m^{(p)})_{::k}V_m^*$ for $m \in [1, M] \cap \mathbb{Z}$ and $k \in [0, K-1] \cap \mathbb{Z}$;

Step 9: For $m \in [1, M] \cap \mathbb{Z}$, let $\tilde{\mathcal{B}}_{::(-m):}^{(p+1)} = \overline{\tilde{\mathcal{B}}_{::m:}^{(p+1)}}$;

Step 10: Terminate if

$$d(\tilde{\mathcal{B}}^{(p+1)}, \tilde{\mathcal{B}}^{(p)}) = \sum_{k=0}^{K+1} \frac{\|\tilde{\mathcal{B}}_{:::k}^{(p+1)} - \tilde{\mathcal{B}}_{:::k}^{(p)}\|_F^2}{\|\tilde{\mathcal{B}}_{:::k}^{(p+1)}\|_F^2} \tag{4.53}$$

is smaller than a preset tolerance, otherwise set $p \coloneqq p + 1$ and go to 1.

The algorithm terminates when the relative change between $\tilde{\mathcal{B}}^{(n)}$ and $\tilde{\mathcal{B}}^{(n+1)}$ is smaller than a tolerance: this provides a more robust algorithm, rather than choosing to let the stopping criteria hinge on the desired coefficient $D_r^{(n)}$.

Before applying the algorithm, to ameliorate bias that may result from the estimation of the cross-correlation data Eq. (4.3) and Eq. (4.4), a further operation can be conducted. For each i, i', k, we seek out the real number $\alpha_{ii'k}$ to make $\mathcal{C}_{ii':k} - \alpha_{ii'k}\mathbf{1}$ as close to the column space of E as possible,

$$\begin{aligned} \alpha_{ii'k} &= \operatorname*{argmin}_{\alpha \in \mathbb{R}} \|\mathcal{U}_{C2}^*(\mathcal{C}_{ii':k} - \alpha\mathbf{1})\|^2 \\ &= \frac{\Re\big((\mathcal{U}_{C2}^*\mathbf{1})^*(\mathcal{U}_{C2}^*\mathcal{C}_{ii':k})\big)}{\|\mathcal{U}_{C2}^*\mathbf{1}\|^2}, \end{aligned} \tag{4.54}$$

where $\mathbf{1}$ is the all-ones vector and $\Re(\cdot)$ takes the real part of a complex number, and then we perform

$$\mathcal{C}_{ii':k} \coloneqq \mathcal{C}_{ii':k} - \alpha_{ii'k}\mathbf{1}. \tag{4.55}$$

The upper bound L of the diameter of the minimal bounding circle of the particle required by Step 2 is the only required prior knowledge. Additionally, MTECS can be modified to capitalize on additional prior information of particle structure when such knowledge is available. Some additional constraints on the intensity I and its circular harmonic coefficients I_m can be derived accordingly. For example, if the particles have s-fold symmetry, then $I_m = 0$ for m that is not a multiple of s. Then Eq. (4.8) can be adapted accordingly.

Analogous to the methods introduced in [39], a filtered cross-correlation tensor, $\mathcal{C}^{\text{filtered}}$, is acquired through Eq. (4.8) using the last $\tilde{\mathcal{B}}^{(n)}$. Against the input $\mathcal{C}$, the signal-to-noise ratio of $\mathcal{C}^{\text{filtered}}$ is significantly enhanced (See Chapter 5) to benefit the aforementioned angular cross-correlation analysis for other X-ray diffraction techniques, e.g. structure reconstruction [10, 43].

Chapter 5

Numerical Experiments

To illustrate the capabilities of the MTECS algorithm outlined in Chapter 4, we applied this approach to a series of carefully designed numerical experiments. We first construct a forward solver to simulate the motion of particles in the sample and collections of XPCS images are synthesized through application of the forward solver. We then applied the MTECS algorithm to the angular-temporal cross-correlation estimated from different number of images produced from this forward solver.

In Section 5.1, we introduce the construction of the simulation and provide some implementation details. In Section 5.2 and Section 5.3, we present the results of two types of numerical experiments, including both the accuracy of the estimated rotational diffusion coefficient D_r and the filtered cross-correlation data given by our algorithm.

5.1 Simulation and Implementation Details

Here we simulate a monodisperse system, i.e. all the particles of interest in the systems are assumed to be identical. Each particle is constructed by attaching two spheres to the ends of a cylinder in three-dimensional space, then projected to two-dimensional space by integrating along z-axis. See Figure 5.1a for the shape. The analytical formulation of the electron density distribution ρ of an individual particle is (up to a scaling constant)

$$\rho(\boldsymbol{r}) = \begin{cases} \sqrt{W^2 - 4r_2^2} & \text{if } 2|r_1| \le T \text{ and } 2|r_2| \le W, \\ 2\sqrt{H^2 - (r_1 - (H + T/2)))^2 - r_2^2} & \text{if } (r_1 - (H + T/2))^2 + r_2^2 \le H^2, \\ 2\sqrt{H^2 - (r_1 + (H + T/2)))^2 - r_2^2} & \text{if } (r_1 + (H + T/2))^2 + r_2^2 \le H^2, \\ 0 & \text{otherwise,} \end{cases} \tag{5.1}$$

where $H = W = \frac{4}{2047}$, and $T = \frac{8}{2047}$.

The intensity I, which is the squared magnitude of the Fourier transform of ρ, can be calculated explicitly,

$$I(q,\phi) = \left| \frac{TWJ_1(\pi Wq\sin\phi)\sin(Tq\cos\phi)}{2Tq^2\sin\phi\cos\phi} + \frac{2H^{3/2}J_{3/2}(2\pi Hq)\cos(2\pi(T/2+H)q\cos\phi)}{q^{3/2}} \right|^2. \tag{5.2}$$

See Figure 5.1b for an illustration of the intensity I. The values of the circular harmonic coefficients I_m are approximated by numerical integration schemes with high precision.

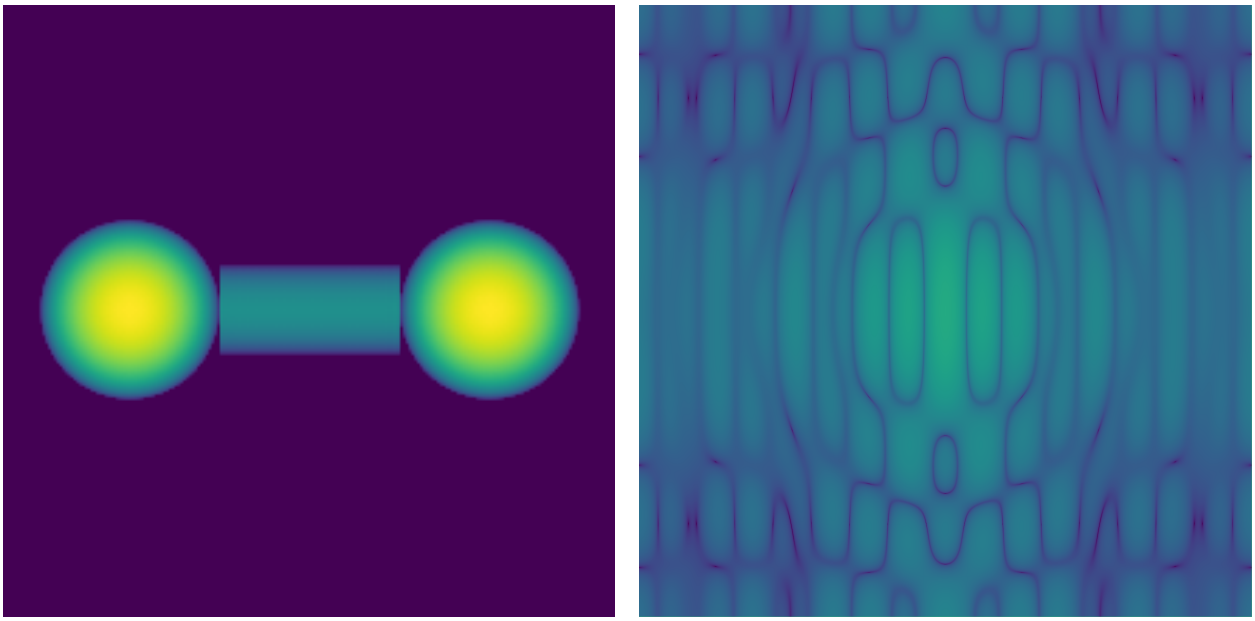

(a) (b)

Figure 5.1: (a) The electron density of an individual particle ρ. (b) The intensity of an individual particle I.

The systems are simulated on a 2047×2047 Cartesian grid equally spaced in domain $[0,1]\times[0,1]$. In each system, there are 500 particles whose initial positions and orientations are uniformly distributed. The position replacements and orientation perturbations are treated as Gaussian random variables. Since we are not focused on estimation of the translation diffusion coefficient in this work, D_t is set to be $D_t = 1/2047^2$ in all the simulated systems, while the rotational diffusion coefficients D_r are selected differently for different systems. Overlapping and collisions are ignored. Figure 5.2a shows an example of part of the simulated samples.

The scattering fields, which are the Fourier transform of the density of the overall sample (Eq. (2.26)), are calculated via the 2D fast Fourier transform. Instead of using the whole

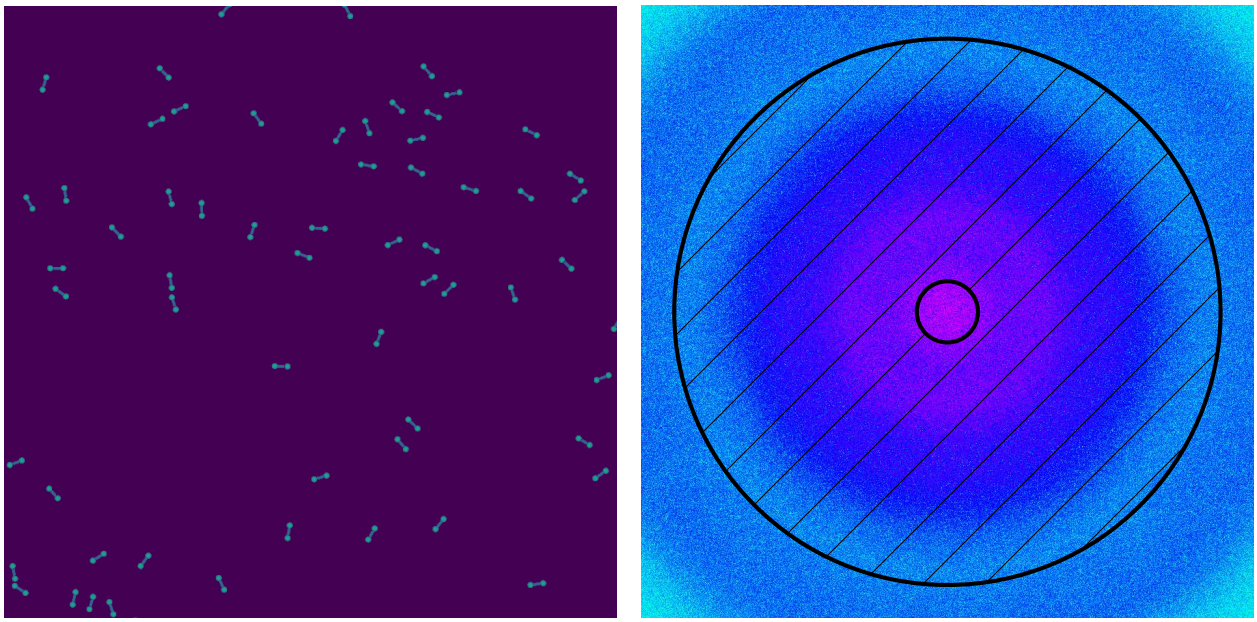

(a) (b)

Figure 5.2: (a) Part of an example of the density of the simulated samples. (b) An example of generated XPCS images (Colormap accentuated to make more graphically visible). The shaded area enclosed by the two circles describes the domain of the polar grid on which the intensity is used.

images on Cartesian grid, we interpolate them to a polar grid with $N_q = 350$ radial coordinates spaced equally on $[51, 400]$ and 3210 angular coordinates spaced equally on $[0, 2\pi)$. See Figure 5.2b for an example of the images. The time difference Δt between consecutive images is 1.0.

For each system, we let $K = 16$, and calculated a cross-correlation data tensor $\mathcal{C} \in \mathbb{R}^{350\times350\times3210\times16}$. The wall time of the calculation of a such tensor from $40,000$ images is 4 hours using 32 single-socket Intel Xeon Phi 7250 processor with 68 cores at 1.4 GHz. Since the number of time lag K is fixed, the time consumed by such calculation scales linearly with respect to the number of images collected.

Some curves of cross-correlation data against the angular coordinates $\Delta\phi$ are shown in Figure 5.3. There are two sharp peaks at $\Delta\phi = 0$ and ϕ in all the plots. The derivation of these peaks can be seen from Theorem 3.1. When $\Delta\phi = 0$ or π and $q = q'$, i.e. $\boldsymbol{q} = \boldsymbol{q}'$ or $\boldsymbol{q} = -\boldsymbol{q}'$, the third or fourth term in the right hand side of Eq. (3.4) remains, leaving a term with factor $N_p(N_p - 1)$ in Eq. (3.9), which manifests as one of the peaks after subtraction of the second term. Since χ is not exactly the indicator function of $\mathbf{0}$ in the simulation, there are also two peaks in Figure 5.3b though $q \neq q'$. The peaks disappear as the difference between

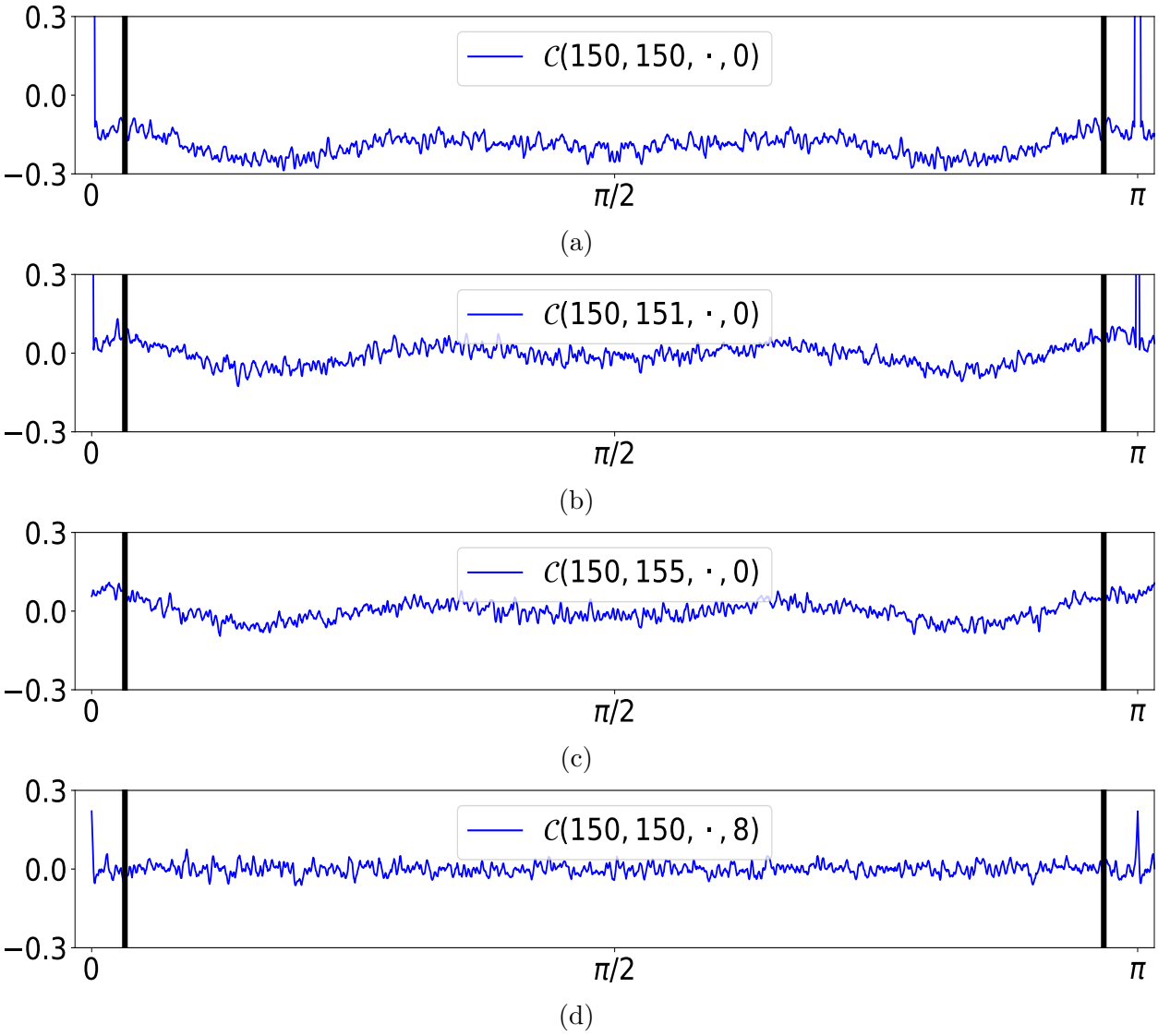

Figure 5.3: Examples of the angular-temporal cross-correlation data with $D_r = 0.01$ at (a) $q = q' = 150$, $k\Delta = 0$, (b) $q = 150$, $q' = 151$, $k\Delta t = 0$, (c) $q = 150$, $q' = 155$, $k\Delta t = 0$, and (d) $q = q' = 150$, $k\Delta t = 8$ against angular coordinates ranging from $[0, \pi)$. The data on $\Delta\phi \in [0, \pi)$ and the data on $\Delta\phi \in [\pi, 2\pi)$ are identical. The vertical black bars indicate the boundaries of the masking that masks out the peaks at $\Delta\phi = 0$ and π.

q and q' becomes larger (See Figure 5.3c). In Figure 5.3d, the heights of the peaks are much smaller, due to the translational diffusion relaxation. Additionally, the data on $\Delta\phi \in [0, \pi)$ are identical to the data on $\Delta\phi \in [\pi, 2\pi)$ due to symmetry of the intensity I. Thus we kept only the data on $\Delta\phi \in [\frac{\pi}{32}, \frac{31\pi}{32}]$, ending up with a data tensor $\mathcal{C} \in \mathbb{R}^{350\times350\times1503\times16}$.

We used $M = 9$ in the truncation of the cross-correlation Eq. (4.8) and the upper bound of the diameter of the particle $L = 0.0128969$ that is 10% larger than the actual diameter. Such precision can be easily achieved in practice.

The first subpart, the correlation noise projector P_C, was solved by methods described in Section 4.1. In computation of the second subpart, the band-limiting projector, we chose $\alpha = 8$ in Eq. (4.31). We solved the tensor decomposition P_O, through a modified alternating least square algorithm depicted in Section 4.3. In the first iterative step of MTECS, we let $(w_{td})_0 = 1$ and $(w_{td})_k = 0$ for $k > 0$, and then in the following iterations of MTECS, let $(w_{td})_k = e^{-4m^2k\Delta t D_r^{(p)}}$, where $D_r^{(p)}$ is the current estimation of the rotational diffusion coefficient. The tolerance of the change of the objective function Eq. (4.41) is 1e-12. To acquire better results, each tensor rank decomposition was repeated 100 times with different random initialization. The exponential fitting P_E was handled by L-BFGS-B [5] with multiple random starts.

In the MTECS algorithm, we first ran several preprocessing iterations which skips the exponential fitting P_E and takes $\tilde{R}^{(p)} = R^{(p)}$ (See Figure 4.1 and Section 4.5). This process ceased if $d(\tilde{\mathcal{B}}^{(p+1)}, \tilde{\mathcal{B}}^{(p)})$ defined by Eq. (4.53) is smaller the 1e-16 or 100 preprocessing iterations is completed. Then we ran the full iterations of MTECS, and terminated the algorithm if $d(\tilde{\mathcal{B}}^{(p+1)}, \tilde{\mathcal{B}}^{(p)})$ is smaller than 1e-16 or after 100 full iterations. It took at most 20 minutes to complete the algorithms on a single core of a 2.3 GHz 16-core Intel Xeon Processor E5-2698 v3.

5.2 First Set of Experiments

In the first type of experiments, for each of the 10 rotational diffusion coefficient $D_r \in \{0.01i\}_{i=1}^{10}$, we simulated a sample from which $40,000$ synthesized images are collected. Then we calculated 10 angular-temporal cross-correlation datasets corresponding to different D_r and input these datasets to the MTECS algorithm.

Table 5.1 gives the ground truth, the estimated D_r given by the MTECS algorithm and the relative error between them. All the relative errors are smaller than 3%.

In Figure 5.4-5.13, we present the curves of the filtered cross-correlation data $\mathcal{C}^{\text{filtered}}$ against the angular coordinate $\Delta\phi$. The input data $\mathcal{C}$ and ground truth calculated from the

Table 5.1: Ground truth of D_r, estimation of D_r, and the relative errors.

True D_r	0.01	0.02	0.03	0.04	0.05
Estimated D_r	0.010062	0.020086	0.030490	0.040521	0.0509191
Relative Error	0.62%	0.43%	1.63%	1.30%	1.84%
True D_r	0.06	0.07	0.08	0.09	0.10
Estimated D_r	0.061311	0.071812	0.080488	0.092633	0.1000931
Relative Error	2.19%	2.59%	0.61%	2.93%	0.09%

the circular harmonic coefficients I_m via Eq. (4.8) are also shown for comparison. These figures show that the curves of filtered cross-correlation data almost completely overlap with the ground truth, demonstrating the ability of the MTECS algorithm to filter the cross-correlation data.

According to Eq. (4.10), we know

$$\mathcal{B}_{iim0} = |I_{2m}(q_i)|^2. \tag{5.3}$$

To further exhibit the ability of the MTECS algorithm to filter the angular-temporal cross-correlation data, the Figure 5.14-5.23 show the $\mathcal{B}_{iim0}^{\text{filtered}}$, which is the $\tilde{\mathcal{B}}^{(p)}$ output by the latest iteration of the algorithm, and $|I_{2m}(q_i)|^2$ against measured q_i. Overall, these figures shows that the circular harmonic coefficients I_m can be estimated up to a phase factor by our algorithm successfully.

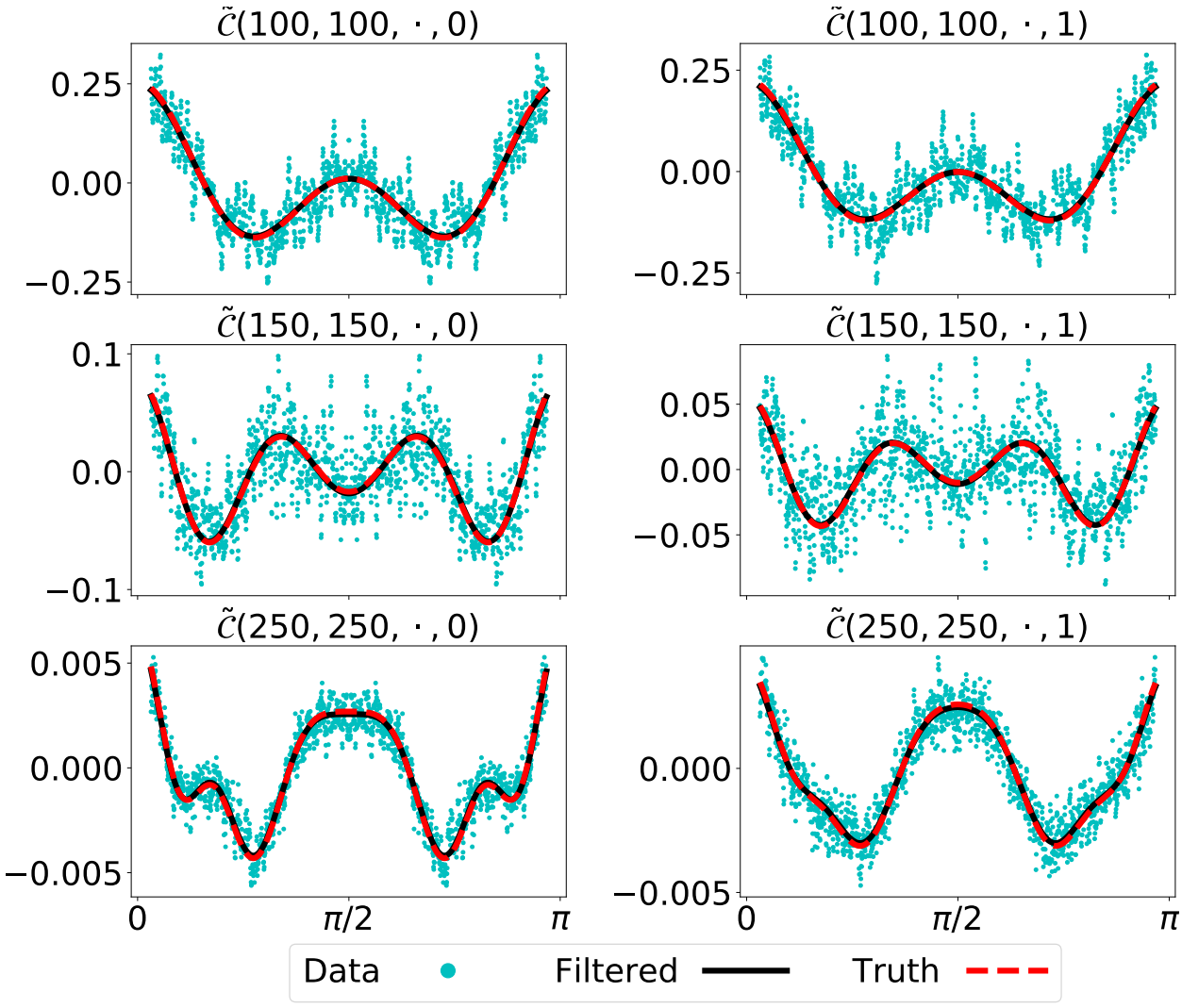

Figure 5.4: Filtered cross-correlation data corresponding to system with $D_r = 0.01$ at (top left) $q = q' = 100$, $k\Delta t = 0$, (top right) $q = q' = 100$, $k\Delta t = 1$, (middle left) $q = q' = 150$, $k\Delta t = 0$, (middle right) $q = q' = 150$, $k\Delta t = 1$, (bottom left) $q = q' = 250$, $k\Delta t = 0$, and (bottom right) $q = q' = 250$, $k\Delta t = 1$, against angular coordinates $\Delta\phi$. The cyan dots are the cross-correlation data computed from images, which are the input to MTECS. The black solid lines are the cross-correlation filtered by the algorithm. Ground truth calculated from ρ is indicated by the red dashed lines.

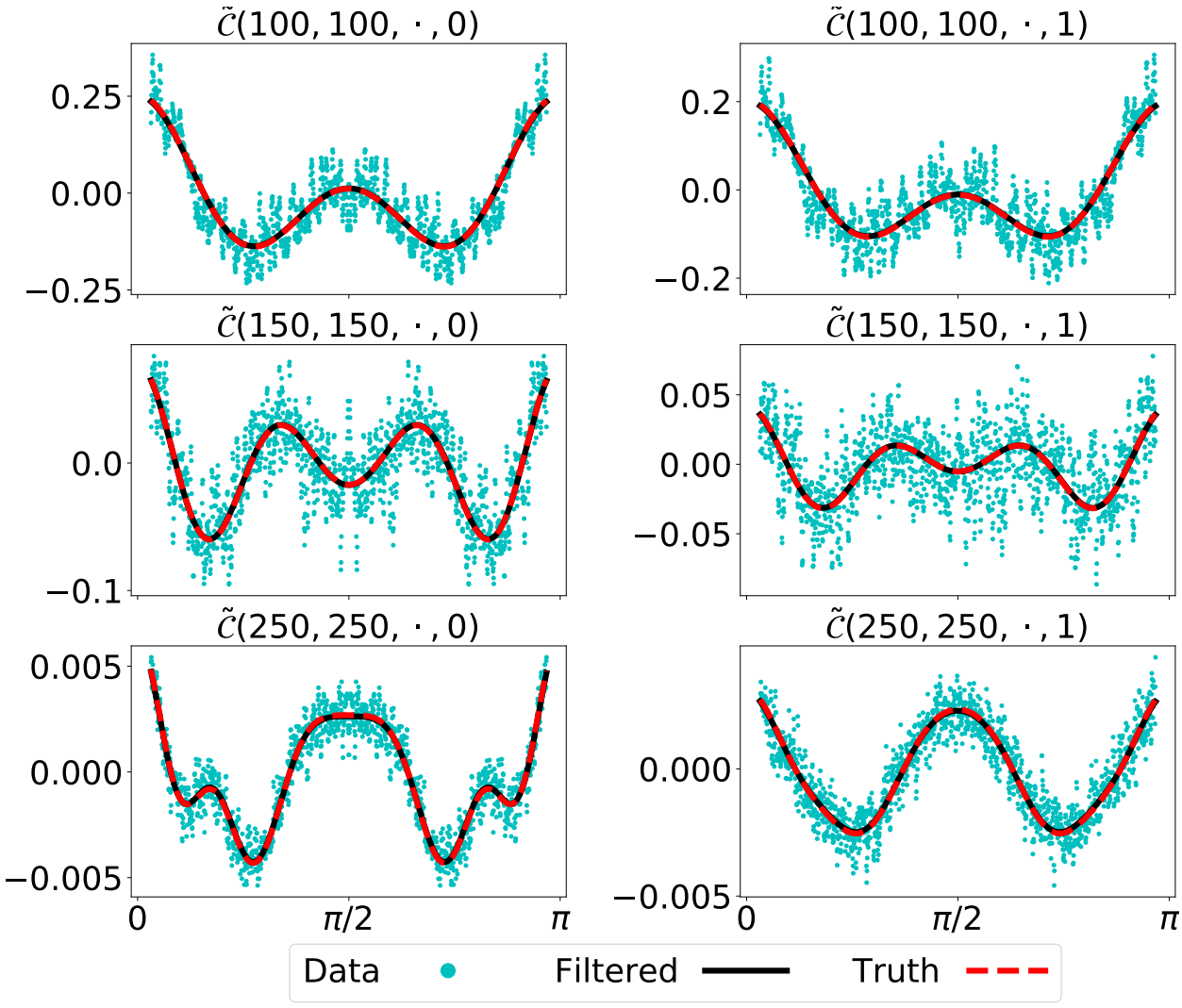

Figure 5.5: Filtered cross-correlation data corresponding to system with $D_r = 0.02$ at (top left) $q = q' = 100$, $k\Delta t = 0$, (top right) $q = q' = 100$, $k\Delta t = 1$, (middle left) $q = q' = 150$, $k\Delta t = 0$, (middle right) $q = q' = 150$, $k\Delta t = 1$, (bottom left) $q = q' = 250$, $k\Delta t = 0$, and (bottom right) $q = q' = 250$, $k\Delta t = 1$, against angular coordinates $\Delta\phi$. The cyan dots are the cross-correlation data computed from images, which are the input to MTECS. The black solid lines are the cross-correlation filtered by the algorithm. Ground truth calculated from ρ is indicated by the red dashed lines.

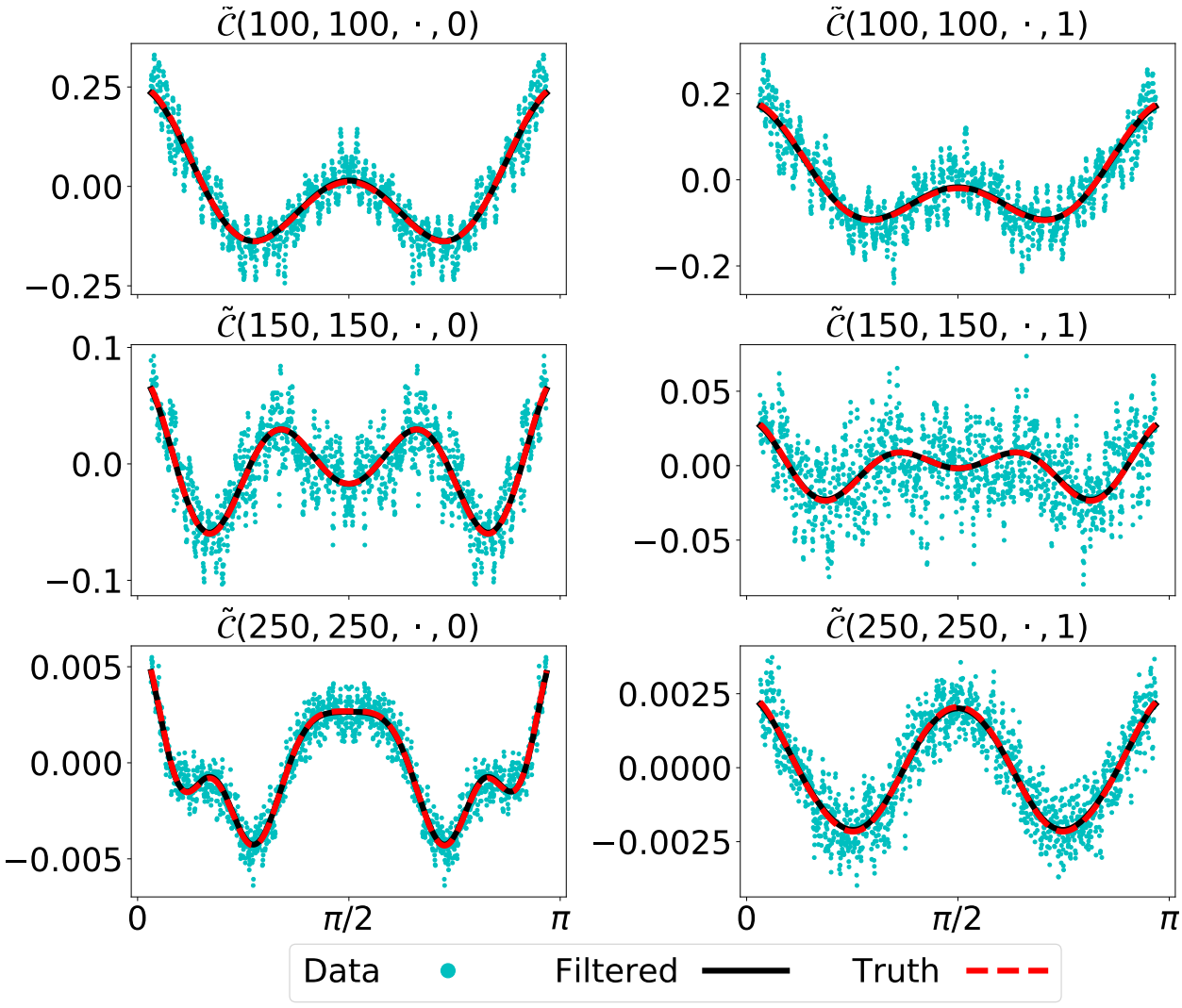

Figure 5.6: Filtered cross-correlation data corresponding to system with $D_r = 0.03$ at (top left) $q = q' = 100$, $k\Delta t = 0$, (top right) $q = q' = 100$, $k\Delta t = 1$, (middle left) $q = q' = 150$, $k\Delta t = 0$, (middle right) $q = q' = 150$, $k\Delta t = 1$, (bottom left) $q = q' = 250$, $k\Delta t = 0$, and (bottom right) $q = q' = 250$, $k\Delta t = 1$, against angular coordinates $\Delta\phi$. The cyan dots are the cross-correlation data computed from images, which are the input to MTECS. The black solid lines are the cross-correlation filtered by the algorithm. Ground truth calculated from ρ is indicated by the red dashed lines.

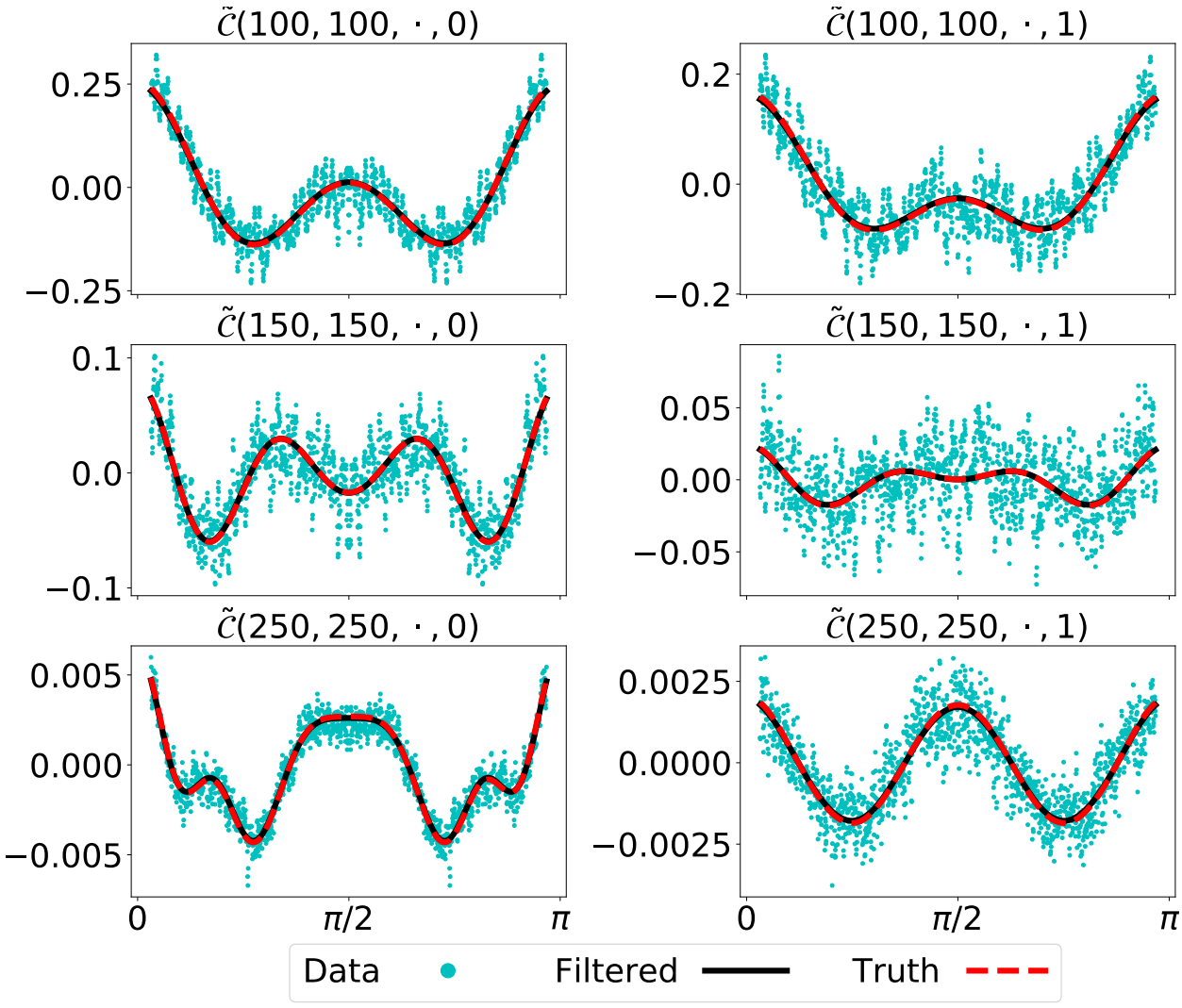

Figure 5.7: Filtered cross-correlation data corresponding to system with $D_r = 0.04$ at (top left) $q = q' = 100$, $k\Delta t = 0$, (top right) $q = q' = 100$, $k\Delta t = 1$, (middle left) $q = q' = 150$, $k\Delta t = 0$, (middle right) $q = q' = 150$, $k\Delta t = 1$, (bottom left) $q = q' = 250$, $k\Delta t = 0$, and (bottom right) $q = q' = 250$, $k\Delta t = 1$, against angular coordinates $\Delta\phi$. The cyan dots are the cross-correlation data computed from images, which are the input to MTECS. The black solid lines are the cross-correlation filtered by the algorithm. Ground truth calculated from ρ is indicated by the red dashed lines.

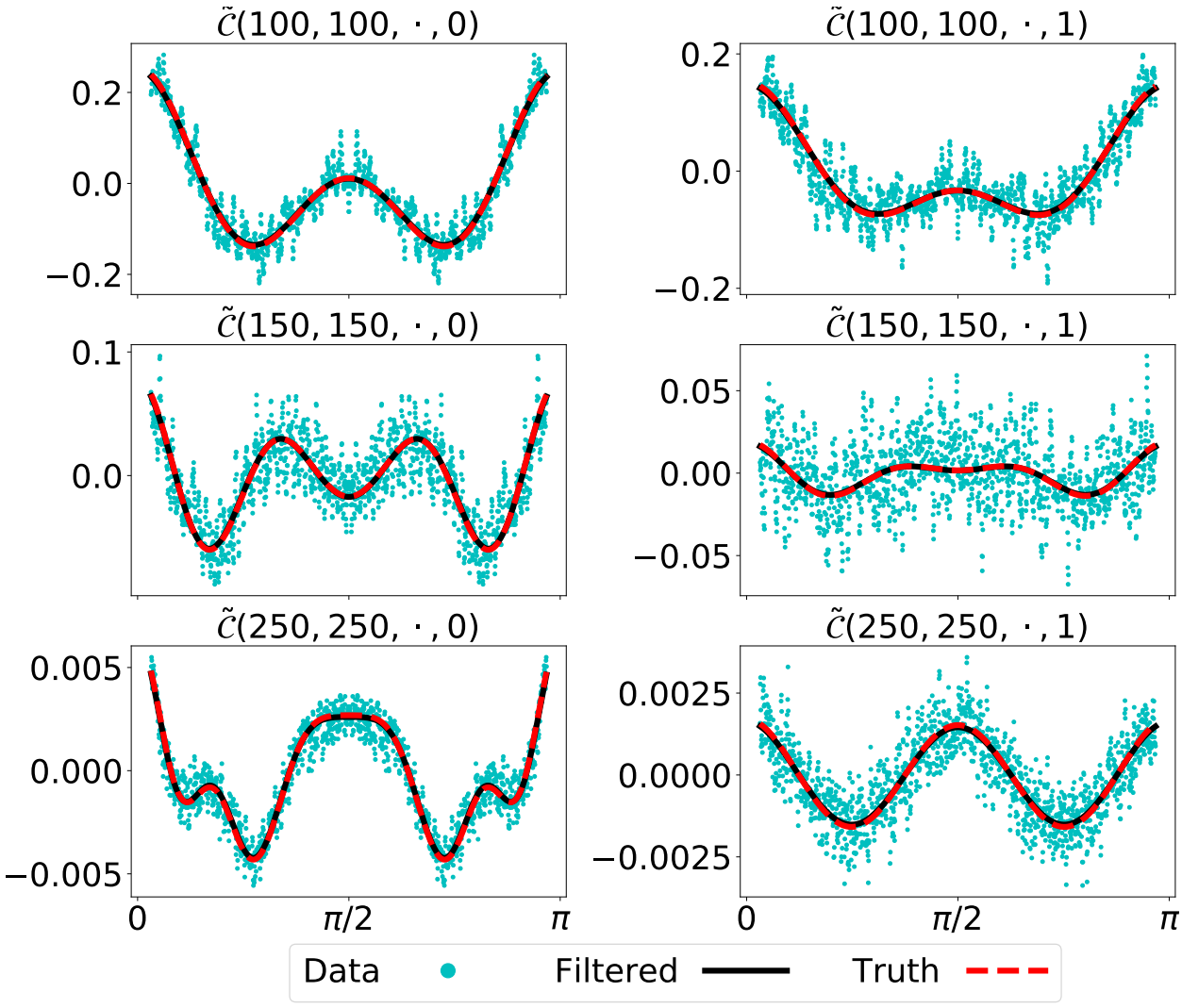

Figure 5.8: Filtered cross-correlation data corresponding to system with $D_r = 0.05$ at (top left) $q = q' = 100$, $k\Delta t = 0$, (top right) $q = q' = 100$, $k\Delta t = 1$, (middle left) $q = q' = 150$, $k\Delta t = 0$, (middle right) $q = q' = 150$, $k\Delta t = 1$, (bottom left) $q = q' = 250$, $k\Delta t = 0$, and (bottom right) $q = q' = 250$, $k\Delta t = 1$, against angular coordinates $\Delta\phi$. The cyan dots are the cross-correlation data computed from images, which are the input to MTECS. The black solid lines are the cross-correlation filtered by the algorithm. Ground truth calculated from ρ is indicated by the red dashed lines.

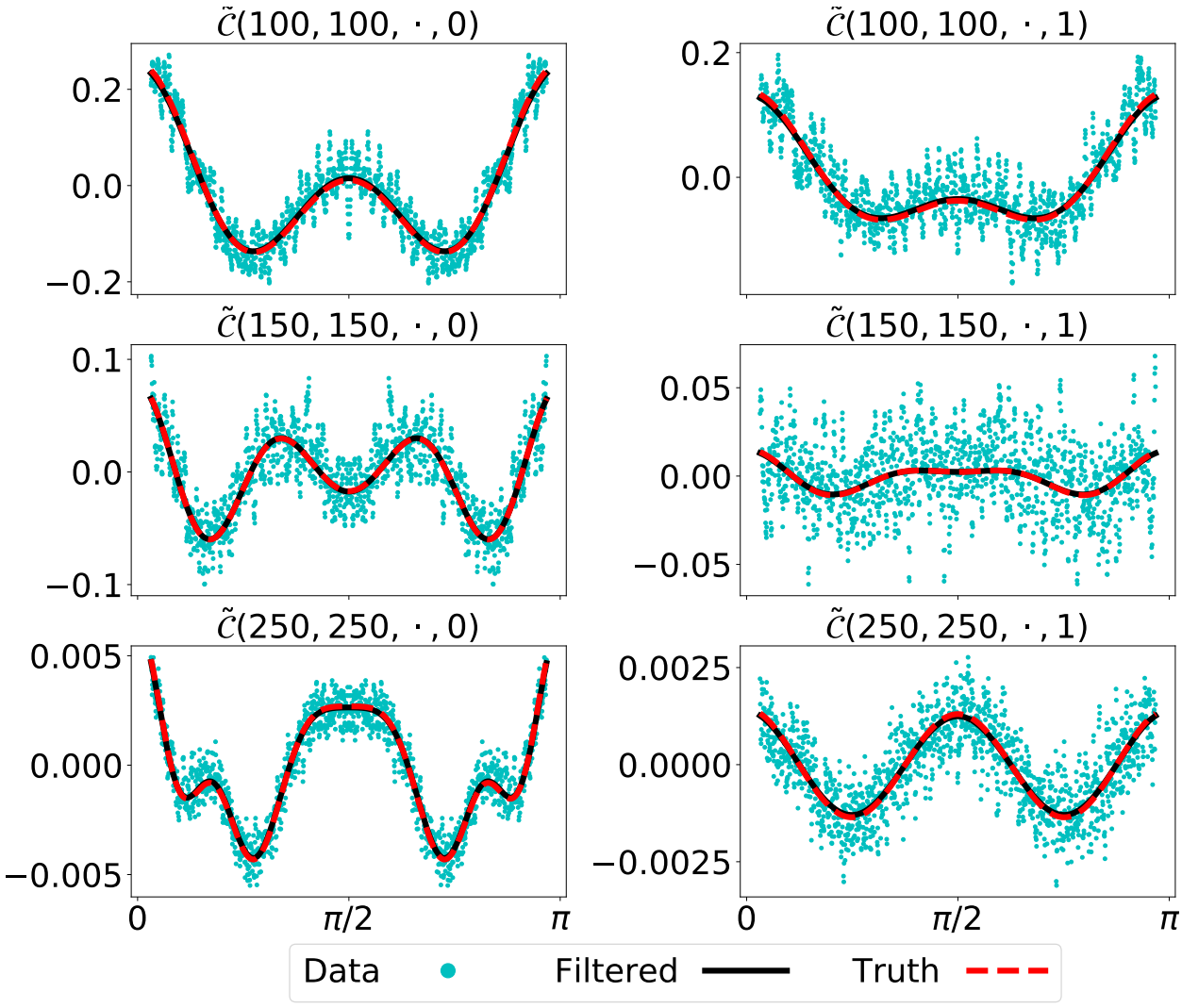

Figure 5.9: Filtered cross-correlation data corresponding to system with $D_r = 0.06$ at (top left) $q = q' = 100$, $k\Delta t = 0$, (top right) $q = q' = 100$, $k\Delta t = 1$, (middle left) $q = q' = 150$, $k\Delta t = 0$, (middle right) $q = q' = 150$, $k\Delta t = 1$, (bottom left) $q = q' = 250$, $k\Delta t = 0$, and (bottom right) $q = q' = 250$, $k\Delta t = 1$, against angular coordinates $\Delta\phi$. The cyan dots are the cross-correlation data computed from images, which are the input to MTECS. The black solid lines are the cross-correlation filtered by the algorithm. Ground truth calculated from ρ is indicated by the red dashed lines.

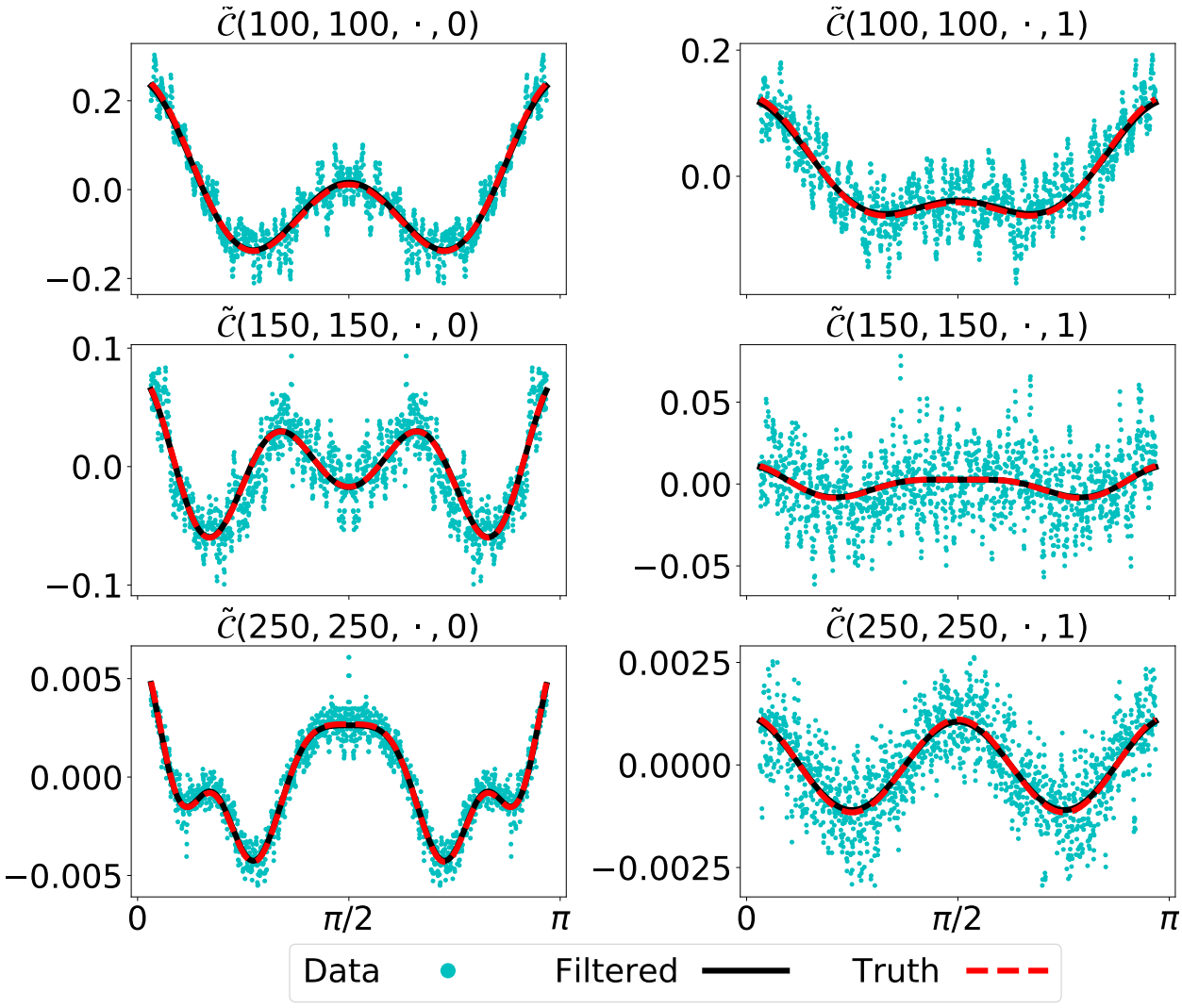

Figure 5.10: Filtered cross-correlation data corresponding to system with $D_r = 0.07$ at (top left) $q = q' = 100$, $k\Delta t = 0$, (top right) $q = q' = 100$, $k\Delta t = 1$, (middle left) $q = q' = 150$, $k\Delta t = 0$, (middle right) $q = q' = 150$, $k\Delta t = 1$, (bottom left) $q = q' = 250$, $k\Delta t = 0$, and (bottom right) $q = q' = 250$, $k\Delta t = 1$, against angular coordinates $\Delta\phi$. The cyan dots are the cross-correlation data computed from images, which are the input to MTECS. The black solid lines are the cross-correlation filtered by the algorithm. Ground truth calculated from ρ is indicated by the red dashed lines.

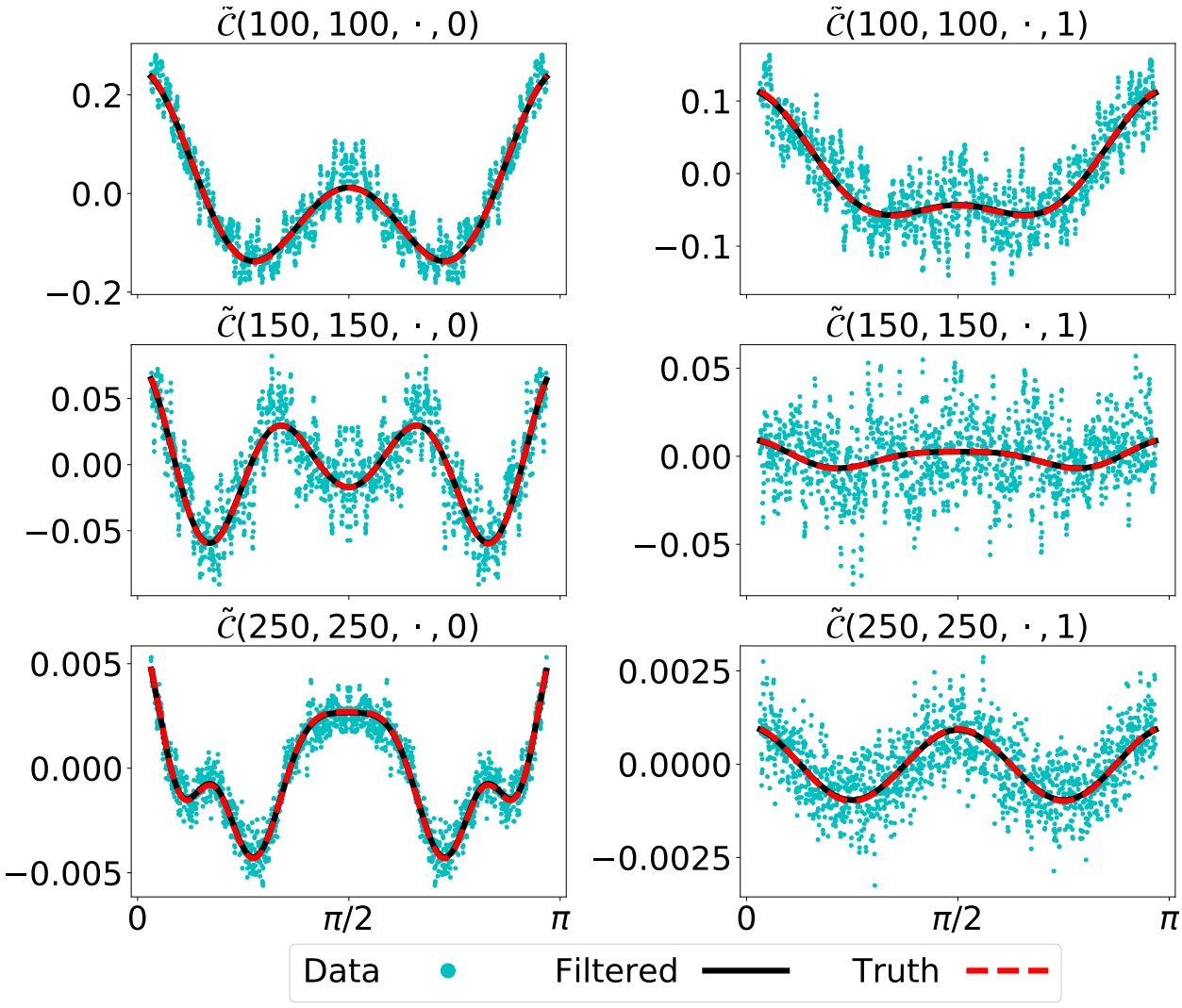

Figure 5.11: Filtered cross-correlation data corresponding to system with $D_r = 0.08$ at (top left) $q = q' = 100$, $k\Delta t = 0$, (top right) $q = q' = 100$, $k\Delta t = 1$, (middle left) $q = q' = 150$, $k\Delta t = 0$, (middle right) $q = q' = 150$, $k\Delta t = 1$, (bottom left) $q = q' = 250$, $k\Delta t = 0$, and (bottom right) $q = q' = 250$, $k\Delta t = 1$, against angular coordinates $\Delta\phi$. The cyan dots are the cross-correlation data computed from images, which are the input to MTECS. The black solid lines are the cross-correlation filtered by the algorithm. Ground truth calculated from ρ is indicated by the red dashed lines.

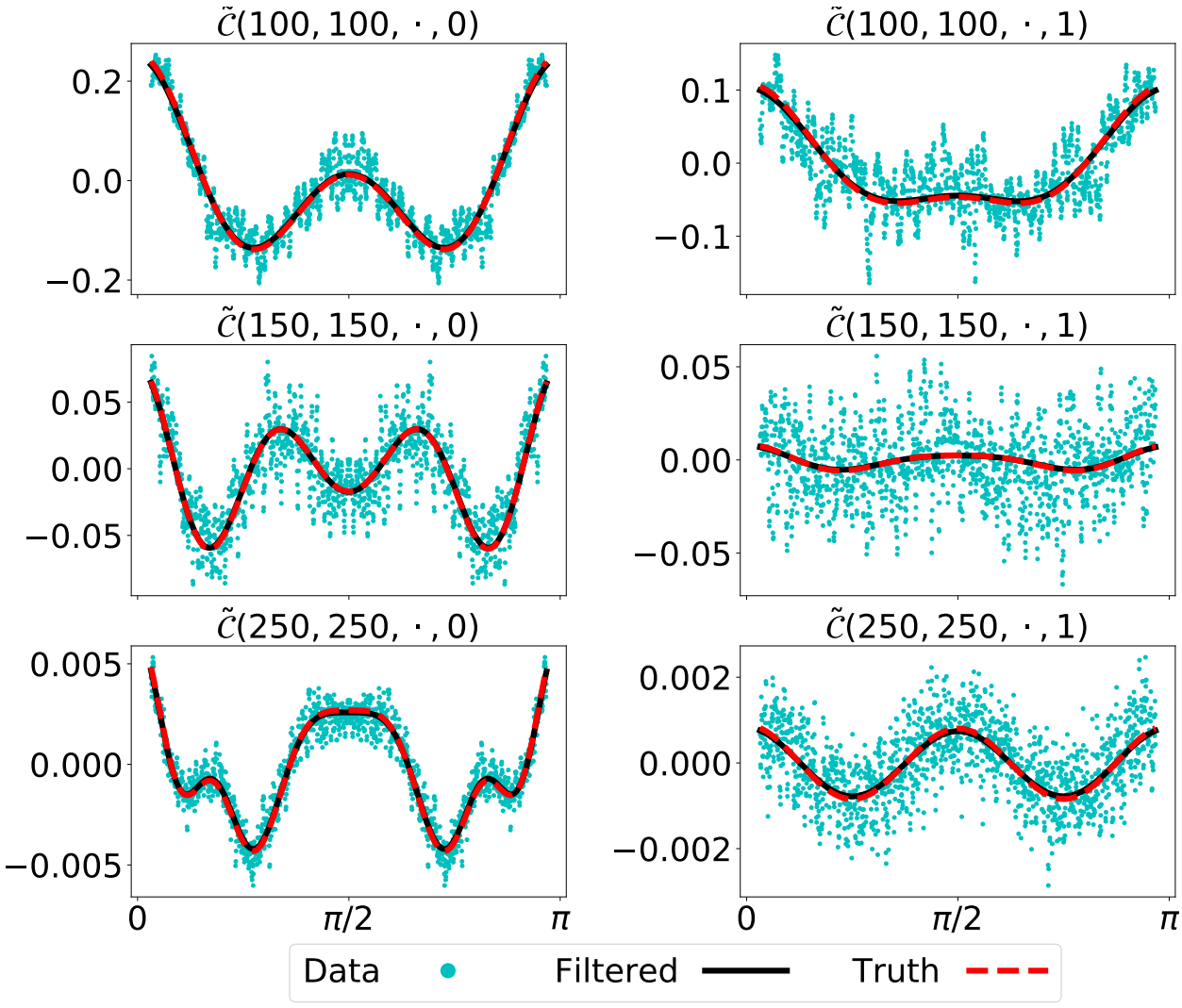

Figure 5.12: Filtered cross-correlation data corresponding to system with $D_r = 0.09$ at (top left) $q = q' = 100$, $k\Delta t = 0$, (top right) $q = q' = 100$, $k\Delta t = 1$, (middle left) $q = q' = 150$, $k\Delta t = 0$, (middle right) $q = q' = 150$, $k\Delta t = 1$, (bottom left) $q = q' = 250$, $k\Delta t = 0$, and (bottom right) $q = q' = 250$, $k\Delta t = 1$, against angular coordinates $\Delta\phi$. The cyan dots are the cross-correlation data computed from images, which are the input to MTECS. The black solid lines are the cross-correlation filtered by the algorithm. Ground truth calculated from ρ is indicated by the red dashed lines.

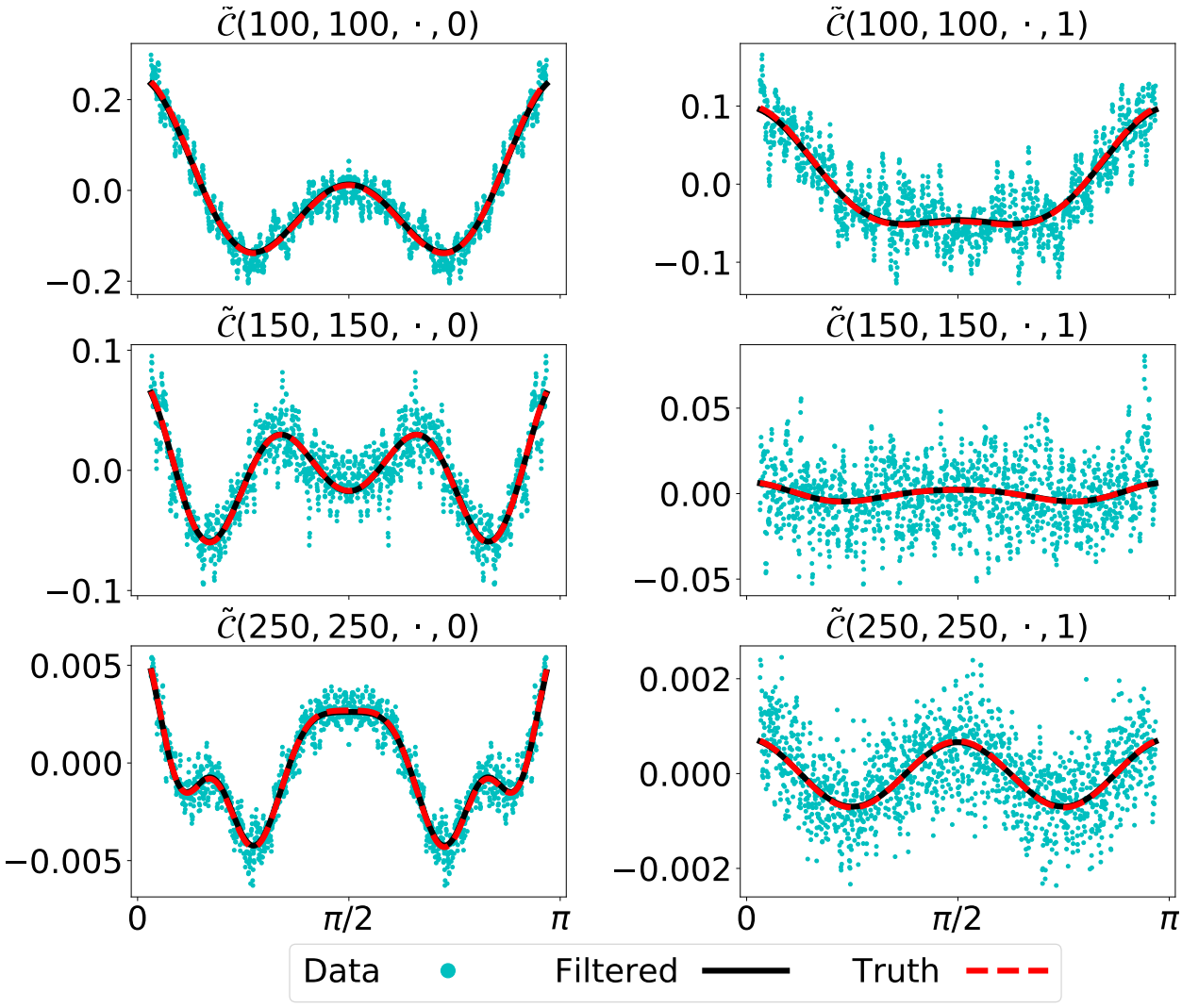

Figure 5.13: Filtered cross-correlation data corresponding to system with $D_r = 0.10$ at (top left) $q = q' = 100$, $k\Delta t = 0$, (top right) $q = q' = 100$, $k\Delta t = 1$, (middle left) $q = q' = 150$, $k\Delta t = 0$, (middle right) $q = q' = 150$, $k\Delta t = 1$, (bottom left) $q = q' = 250$, $k\Delta t = 0$, and (bottom right) $q = q' = 250$, $k\Delta t = 1$, against angular coordinates $\Delta\phi$. The cyan dots are the cross-correlation data computed from images, which are the input to MTECS. The black solid lines are the cross-correlation filtered by the algorithm. Ground truth calculated from ρ is indicated by the red dashed lines.

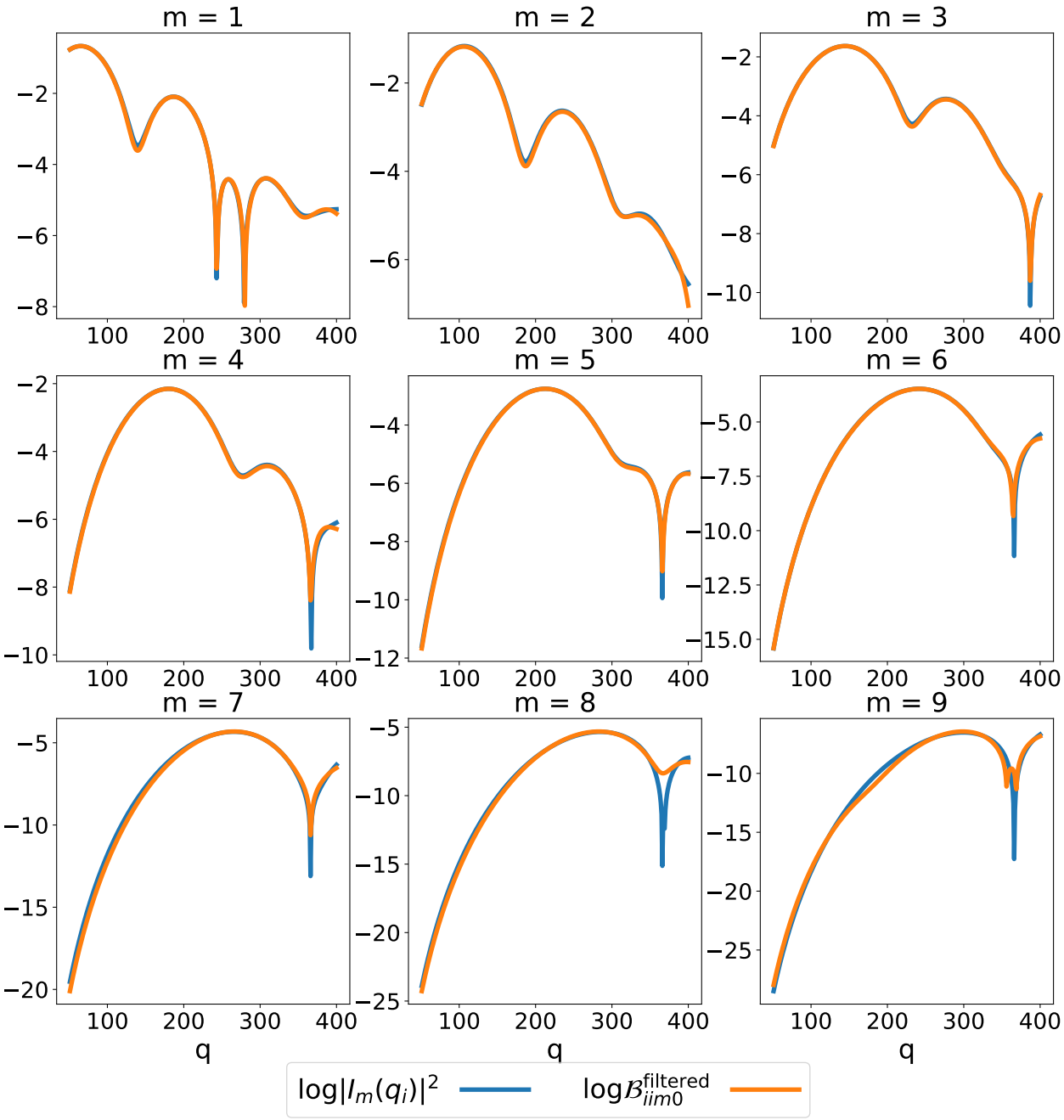

Figure 5.14: The $\log(\mathcal{B}^{\text{filtered}}_{iim0})$ (in orange) corresponding to the system with $D_r = 0.01$ and $\log|I_{2m}(q_i)|^2$ (in blue) versus measured q_i.

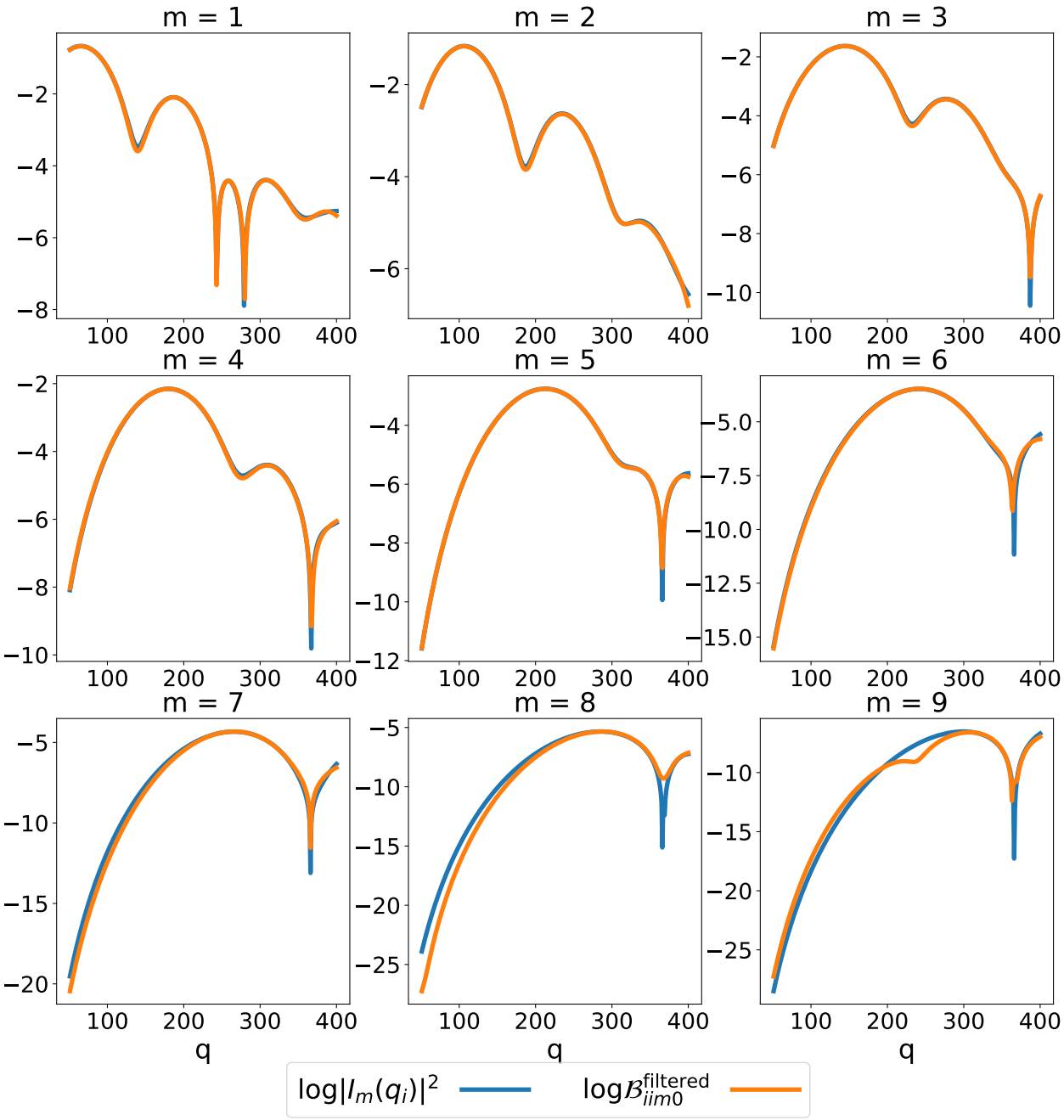

Figure 5.15: The $\log(\mathcal{B}^{\text{filtered}}_{iim0})$ (in orange) corresponding to the system with $D_r = 0.02$ and $\log|I_{2m}(q_i)|^2$ (in blue) versus measured q_i.

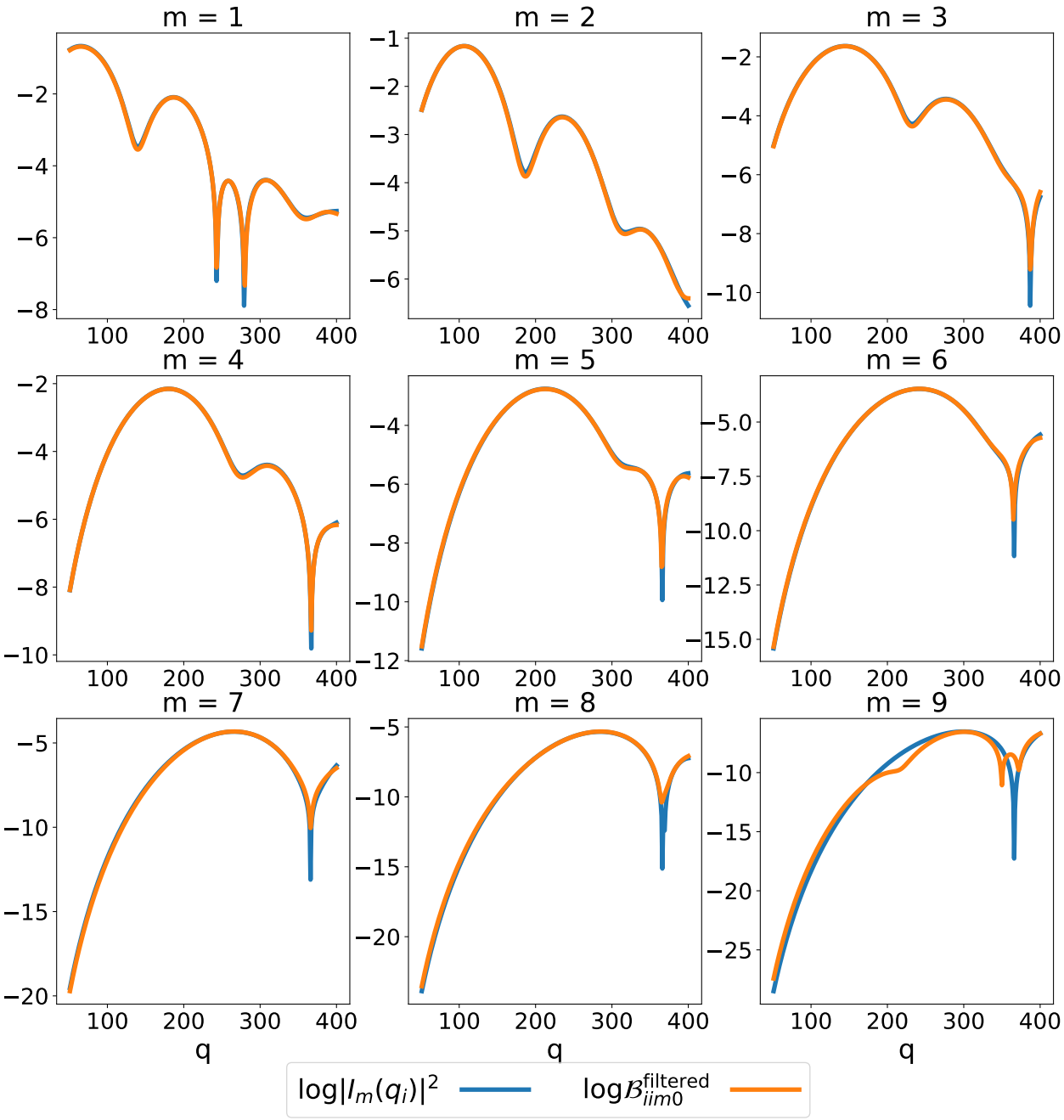

Figure 5.16: The $\log(\mathcal{B}^{\text{filtered}}_{iim0})$ (in orange) corresponding to the system with $D_r = 0.03$ and $\log|I_{2m}(q_i)|^2$ (in blue) versus measured q_i.

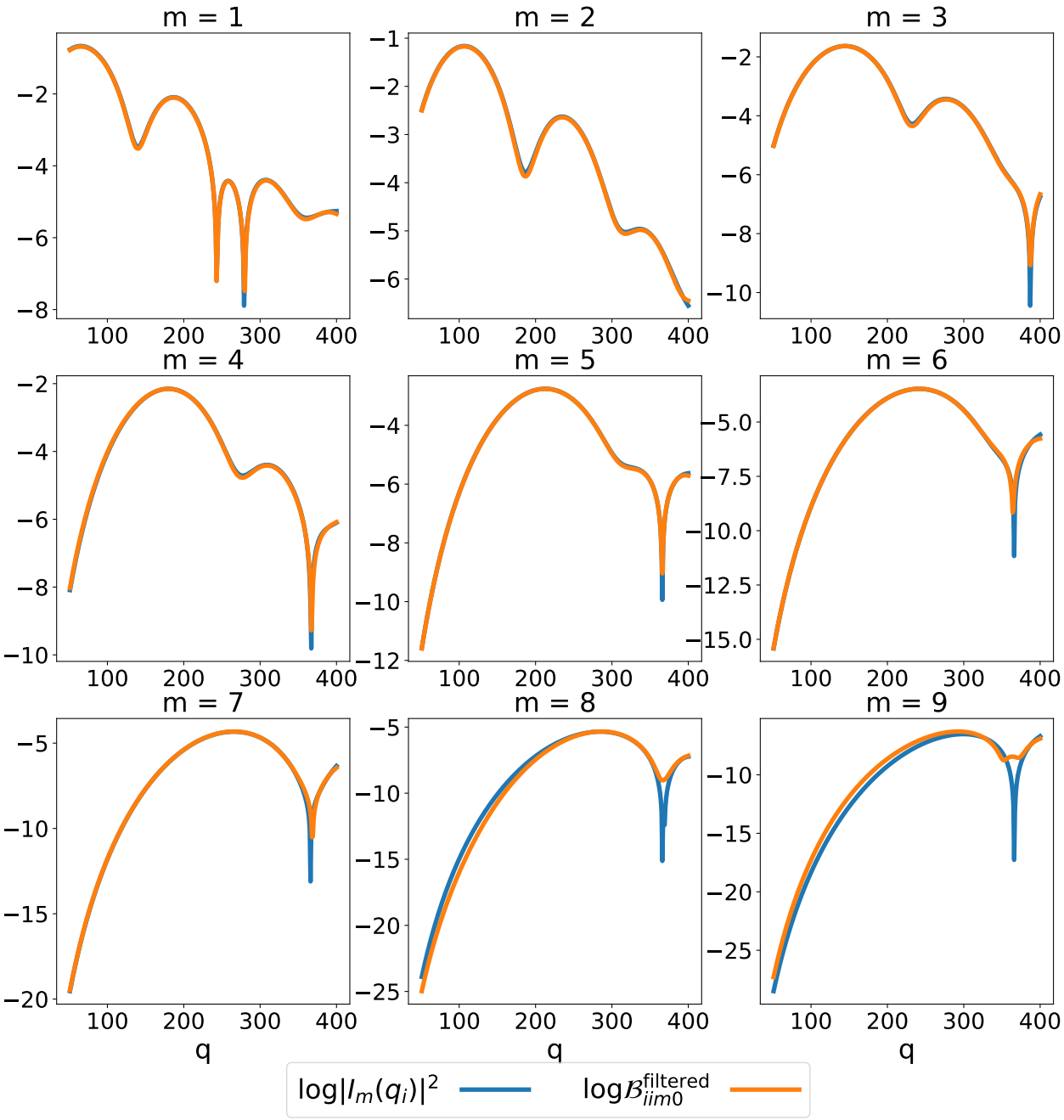

Figure 5.17: The $\log(\mathcal{B}^{\text{filtered}}_{iim0})$ (in orange) corresponding to the system with $D_r = 0.04$ and $\log|I_{2m}(q_i)|^2$ (in blue) versus measured q_i.

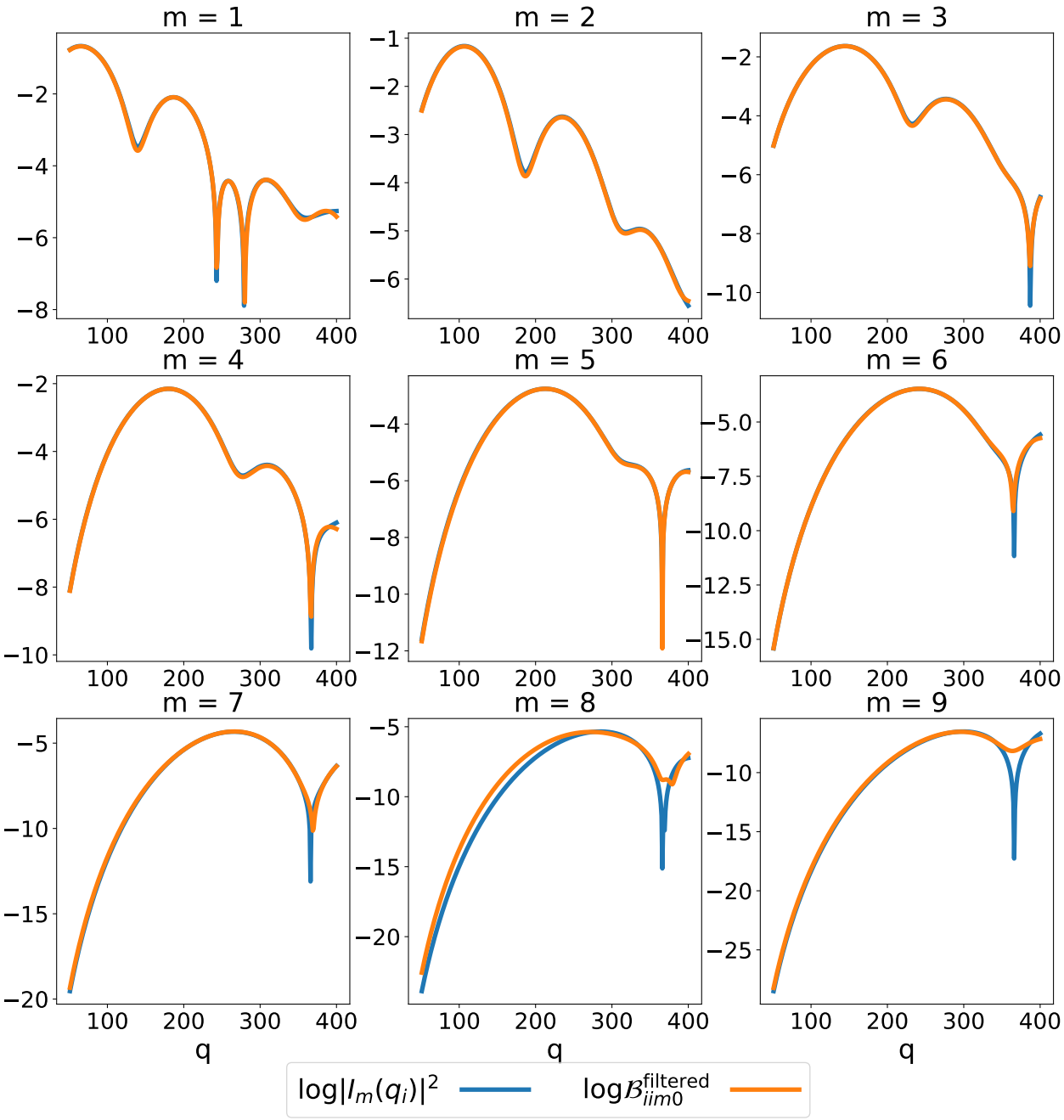

Figure 5.18: The $\log(\mathcal{B}^{\text{filtered}}_{iim0})$ (in orange) corresponding to the system with $D_r = 0.05$ and $\log|I_{2m}(q_i)|^2$ (in blue) versus measured q_i.

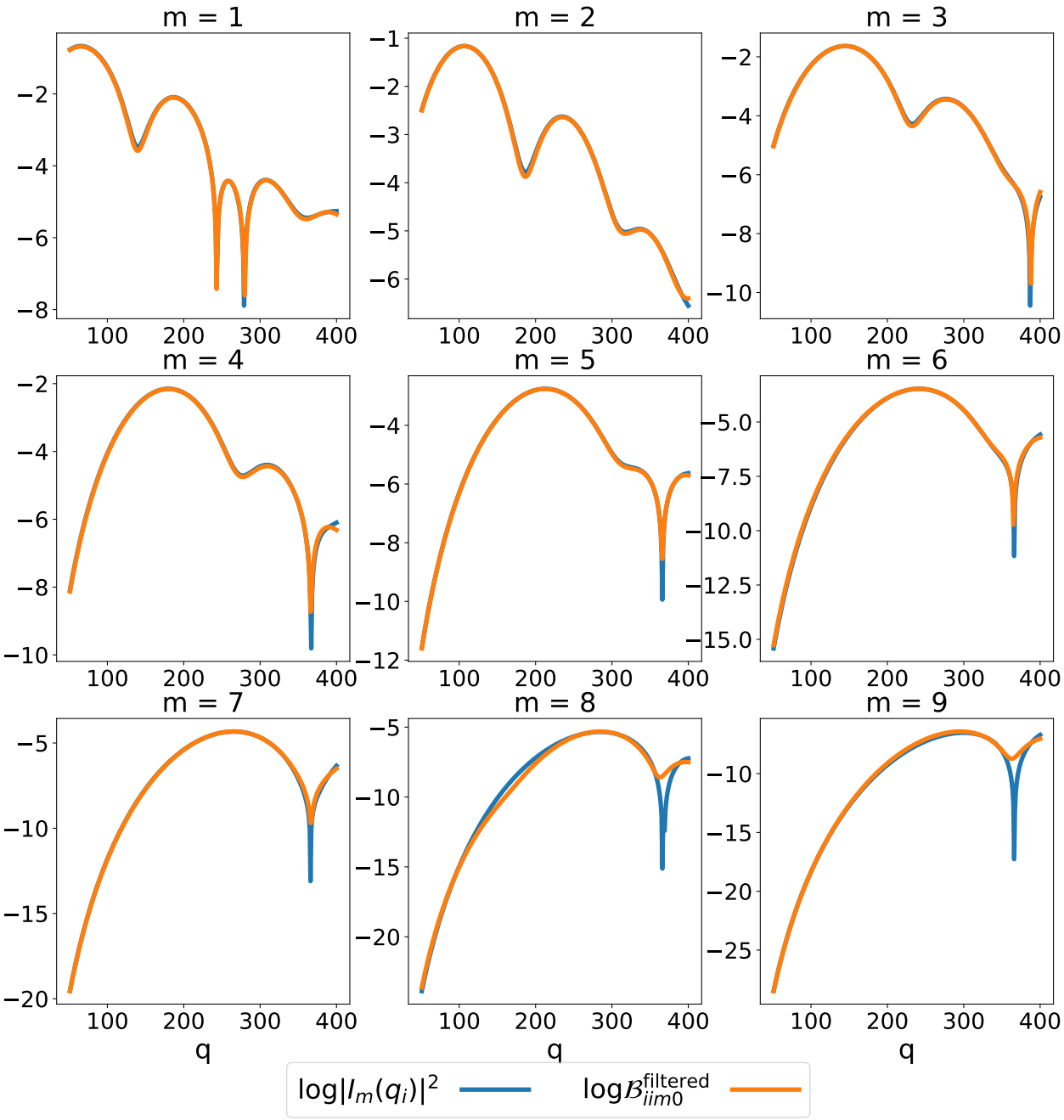

Figure 5.19: The $\log(\mathcal{B}^{\text{filtered}}_{iim0})$ (in orange) corresponding to the system with $D_r = 0.06$ and $\log|I_{2m}(q_i)|^2$ (in blue) versus measured q_i.

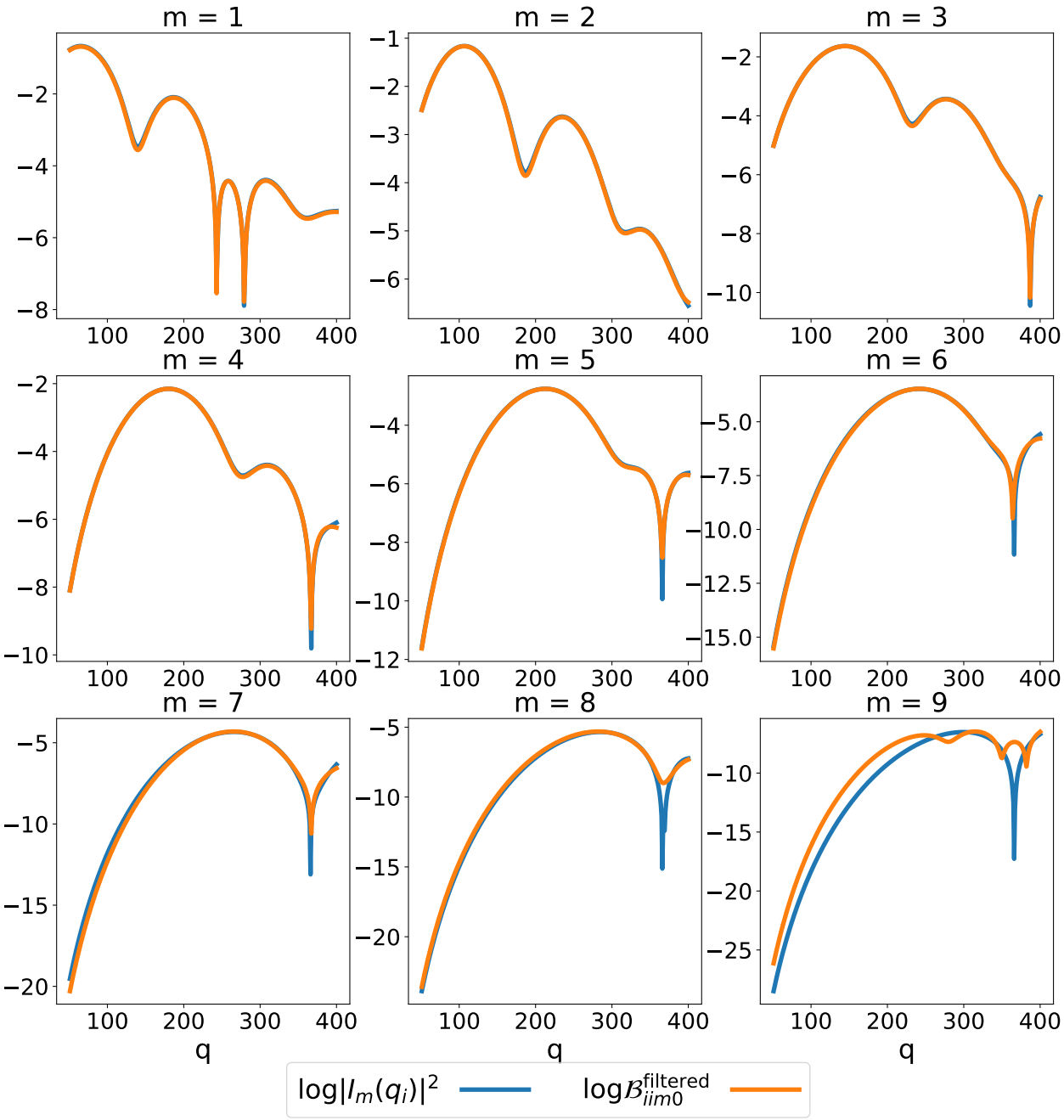

Figure 5.20: The $\log(\mathcal{B}^{\text{filtered}}_{iim0})$ (in orange) corresponding to the system with $D_r = 0.07$ and $\log|I_{2m}(q_i)|^2$ (in blue) versus measured q_i.

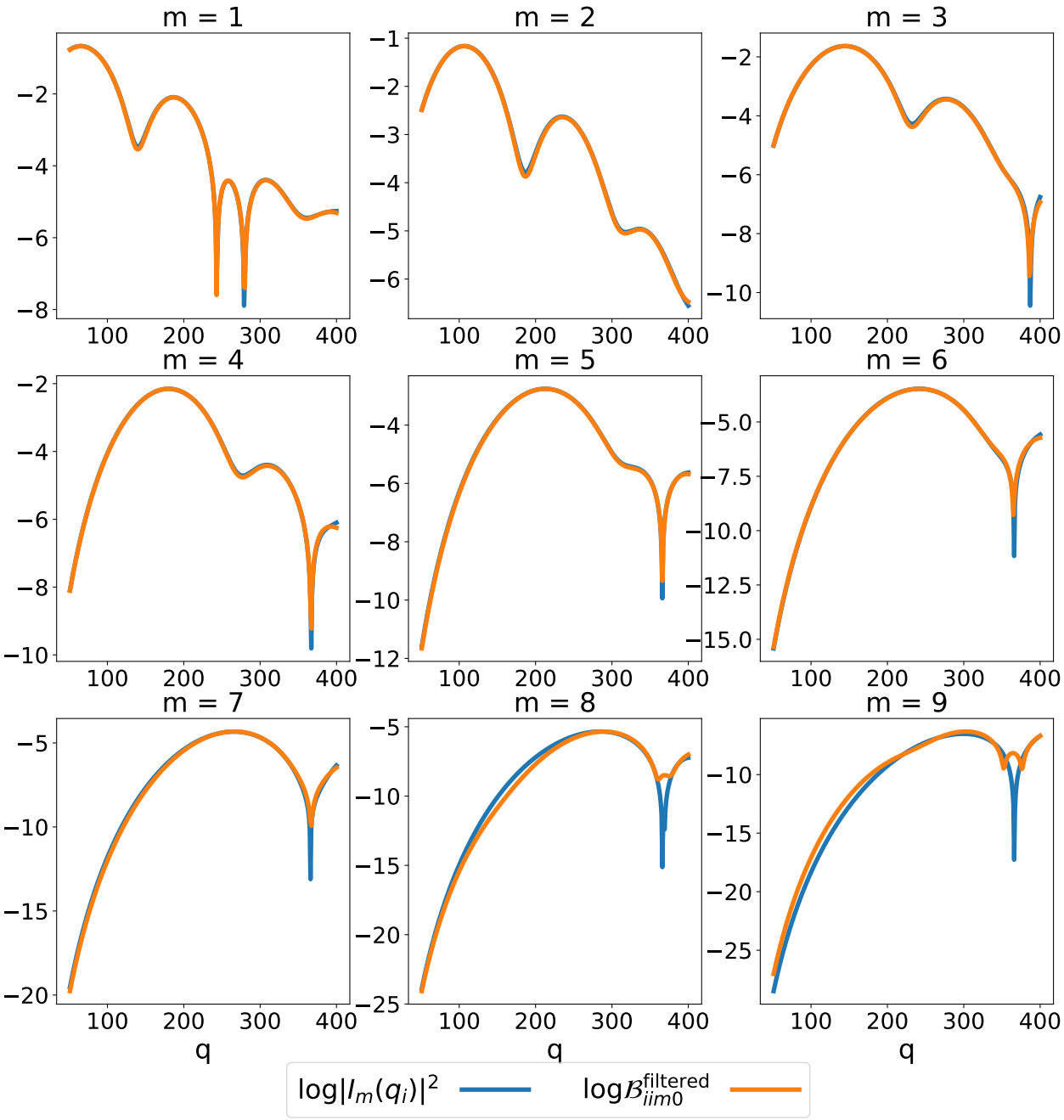

Figure 5.21: The $\log(\mathcal{B}^{\text{filtered}}_{iim0})$ (in orange) corresponding to the system with $D_r = 0.08$ and $\log|I_{2m}(q_i)|^2$ (in blue) versus measured q_i.

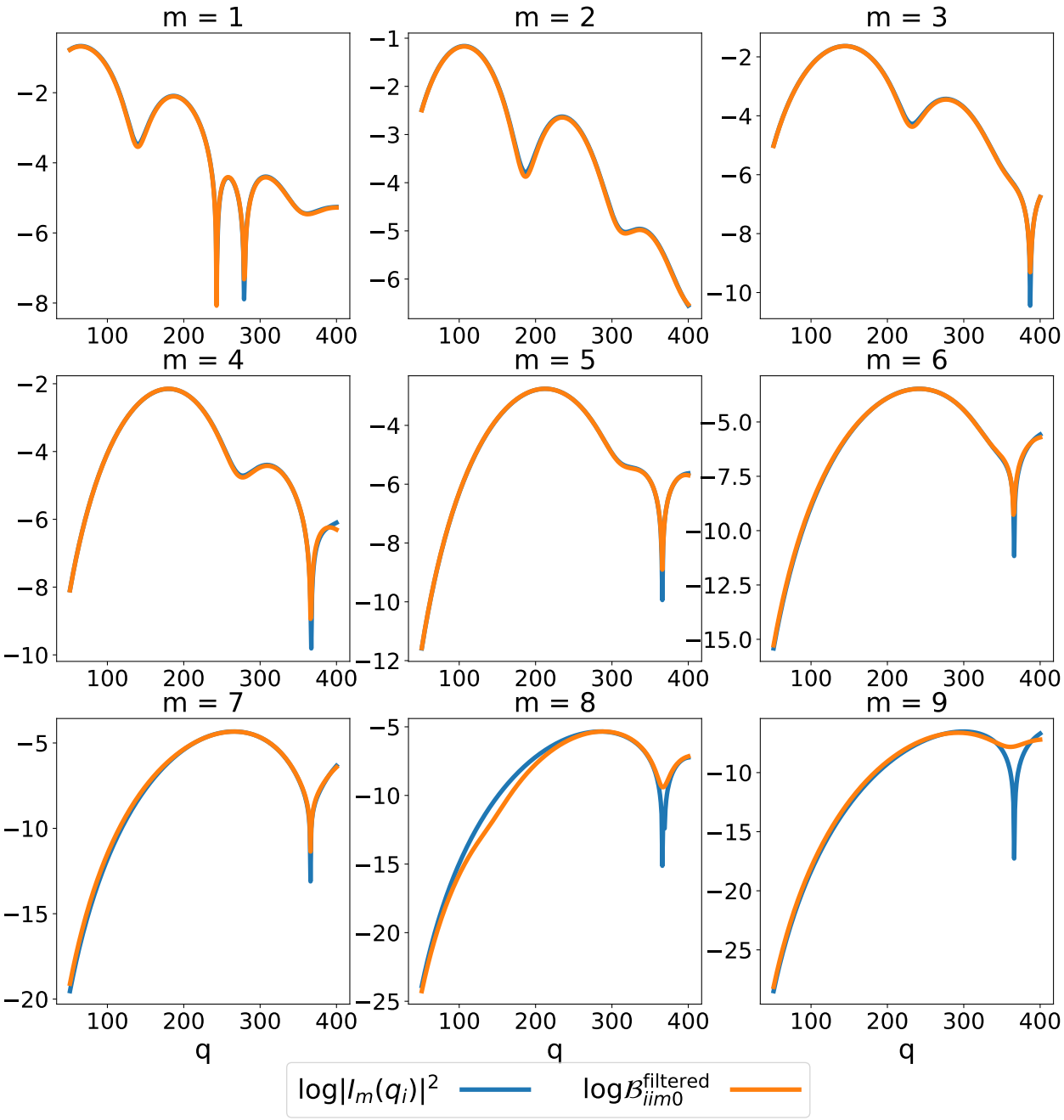

Figure 5.22: The $\log(\mathcal{B}^{\text{filtered}}_{iim0})$ (in orange) corresponding to the system with $D_r = 0.09$ and $\log|I_{2m}(q_i)|^2$ (in blue) versus measured q_i.

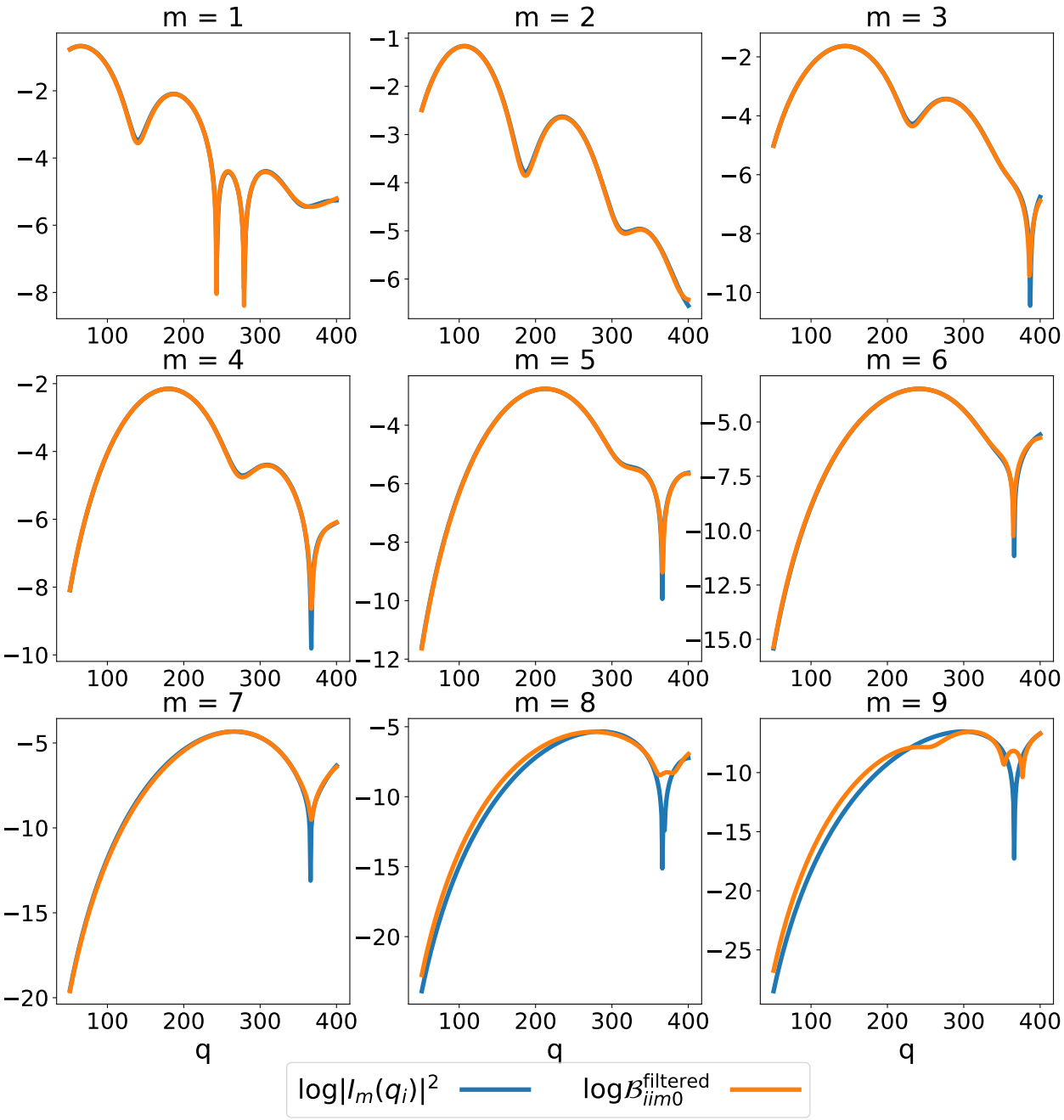

Figure 5.23: The $\log(\mathcal{B}^{\text{filtered}}_{iim0})$ (in orange) corresponding to the system with $D_r = 0.10$ and $\log|I_{2m}(q_i)|^2$ (in blue) versus measured q_i.

5.3 Second Set of Experiments

To understand how the computed accuracy depends on the number of images, for $D_r = 0.01, 0.02, 0.04, 0.08$, we gradually reduced the number of images from $40,000$ to $4,000$. Due to the stochastic nature of the experiments, which is also true in practice, the outputs exhibit some randomness. To characterize the results better, for each value of D_r and each number of images, we repeated the experiments 10 times, and hence generated 10 different estimations, whose statistics are shown in Figure 5.24. We note that the MTECS algorithm is still able to give reasonable estimation while using less images. Despite the fluctuation, the trend shows that as the number of images increases, the quality of the estimations improves. The result of each experiment is shown in Table 5.2-5.5.

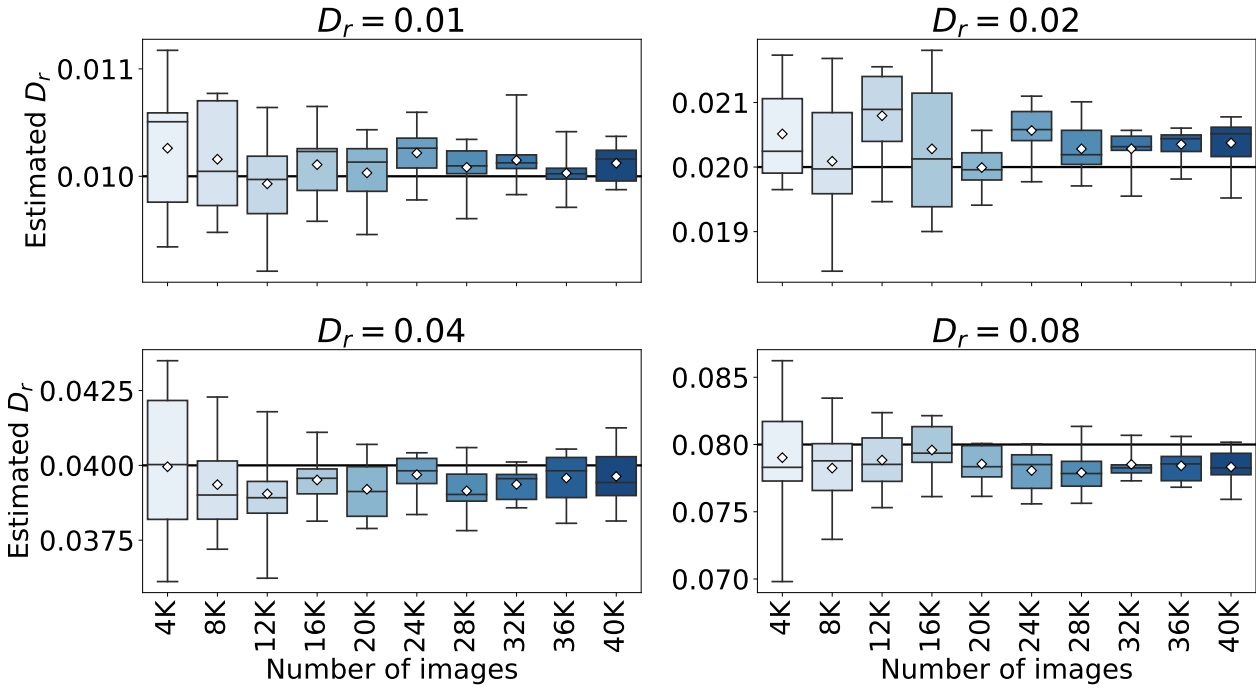

Figure 5.24: Quantiles of 10 different estimated values against number of images. Horizontal bars from top to bottom are maxima, third quartiles, medians, first quartiles, and minima. White boxes are averages. Horizontal lines behind boxes are ground truth.

Table 5.2: D_r estimated from different number of images generated by systems with the ground truth $D_r = 0.01$.

	Number of images				
	$4,000$	$8,000$	$12,000$	$16,000$	$2,0000$
Estimated D_r	0.009776	0.010763	0.010151	0.010260	0.009854
	0.009504	0.010772	0.009908	0.010441	0.010276
	0.010887	0.010748	0.009869	0.010247	0.010433
	0.011173	0.009946	0.009580	0.009581	0.010266
	0.010486	0.009478	0.010199	0.010008	0.010230
	0.009753	0.009814	0.009525	0.010215	0.009659
	0.010565	0.009653	0.010032	0.009821	0.010080
	0.010530	0.010569	0.009116	0.009611	0.009879
	0.010599	0.009699	0.010640	0.010249	0.009458
	0.009343	0.010146	0.010274	0.010650	0.010184

	Number of images				
	$24,000$	$28,000$	$32,000$	$36,000$	$40,000$
Estimated D_r	0.010377	0.010101	0.010087	0.010415	0.010226
	0.010047	0.009935	0.010067	0.009976	0.009903
	0.009851	0.010151	0.010757	0.010081	0.010372
	0.010277	0.010061	0.010165	0.010057	0.010300
	0.010541	0.010011	0.009834	0.009711	0.009926
	0.010247	0.009606	0.010288	0.010154	0.010248
	0.010168	0.010344	0.010129	0.009973	0.010047
	0.009780	0.010265	0.010121	0.009991	0.010120
	0.010289	0.010271	0.009829	0.009882	0.010201
	0.010596	0.010093	0.010211	0.010056	0.009875

Table 5.3: D_r estimated from different number of images generated by systems with the ground truth $D_r = 0.02$.

	Number of images				
	$4,000$	$8,000$	$12,000$	$16,000$	$2,0000$
Estimated D_r	0.019651	0.021060	0.021338	0.021807	0.019410
	0.021003	0.020006	0.020068	0.019270	0.019974
	0.019715	0.019617	0.021424	0.019370	0.019943
	0.021078	0.021023	0.021552	0.020703	0.019714
	0.020193	0.019936	0.021184	0.020512	0.020252
	0.020275	0.021681	0.020515	0.019431	0.019776
	0.021733	0.019304	0.019464	0.021692	0.019870
	0.021455	0.018388	0.020358	0.021291	0.020568
	0.019810	0.020305	0.021443	0.019002	0.020281
	0.020213	0.019577	0.020601	0.019739	0.020129

	Number of images				
	$24,000$	$28,000$	$32,000$	$36,000$	$40,000$
Estimated D_r	0.020859	0.019708	0.020357	0.020588	0.020381
	0.019985	0.021010	0.019550	0.020110	0.020089
	0.021098	0.020383	0.020486	0.020218	0.019521
	0.020578	0.019757	0.020453	0.020311	0.020777
	0.021020	0.020050	0.020532	0.020430	0.020742
	0.020532	0.020862	0.020266	0.020447	0.020571
	0.020369	0.020225	0.020257	0.019814	0.020459
	0.019772	0.020630	0.020274	0.020603	0.019965
	0.020582	0.020037	0.020568	0.020496	0.020594
	0.020860	0.020158	0.020091	0.020498	0.020625

Table 5.4: D_r estimated from different number of images generated by systems with the ground truth $D_r = 0.04$.

	Number of images				
	$4,000$	$8,000$	$12,000$	$16,000$	$2,0000$
Estimated D_r	0.042482	0.038119	0.041792	0.038354	0.040701
	0.042250	0.037198	0.038996	0.041104	0.038965
	0.036396	0.038022	0.036229	0.039551	0.038271
	0.038844	0.039833	0.038531	0.039966	0.040023
	0.041045	0.039486	0.039495	0.039586	0.037891
	0.043497	0.040252	0.041162	0.038136	0.040502
	0.036117	0.042284	0.039368	0.038917	0.038230
	0.039007	0.038445	0.038841	0.040427	0.038381
	0.041927	0.038531	0.038359	0.039628	0.039758
	0.037979	0.041386	0.037712	0.039444	0.039288

	Number of images				
	$24,000$	$28,000$	$32,000$	$36,000$	$40,000$
Estimated D_r	0.040247	0.040005	0.039619	0.039139	0.040002
	0.039772	0.037970	0.040113	0.038851	0.040386
	0.039379	0.039070	0.038770	0.039742	0.038938
	0.040239	0.038756	0.039139	0.038749	0.039376
	0.038357	0.038987	0.039493	0.040373	0.039154
	0.040420	0.037820	0.039705	0.038065	0.038141
	0.038961	0.038955	0.038604	0.039896	0.038859
	0.039436	0.039566	0.039942	0.040096	0.040716
	0.040213	0.040594	0.039672	0.040320	0.039478
	0.039865	0.039754	0.038582	0.040544	0.041253

Table 5.5: D_r estimated from different number of images generated by systems with the ground truth $D_r = 0.08$.

	Number of images				
	$4,000$	$8,000$	$12,000$	$16,000$	$2,0000$
Estimated D_r	0.084387	0.077137	0.078410	0.078938	0.078761
	0.078475	0.074075	0.082237	0.081887	0.077938
	0.086231	0.083450	0.075308	0.082137	0.080075
	0.077179	0.079486	0.082369	0.079660	0.077425
	0.076623	0.080197	0.078634	0.079570	0.079998
	0.069808	0.079664	0.080833	0.077699	0.077849
	0.078132	0.072949	0.078292	0.082144	0.079924
	0.082525	0.081010	0.076916	0.079144	0.077510
	0.077604	0.076396	0.079452	0.076127	0.079901
	0.079279	0.078088	0.075951	0.078591	0.076146

	Number of images				
	$24,000$	$28,000$	$32,000$	$36,000$	$40,000$
Estimated D_r	0.078976	0.075630	0.078508	0.079124	0.077992
	0.079270	0.079017	0.080684	0.077928	0.079515
	0.076110	0.077441	0.078190	0.079077	0.080172
	0.077082	0.076215	0.080115	0.080601	0.077672
	0.076626	0.081348	0.077788	0.078146	0.078836
	0.079772	0.078493	0.078422	0.079493	0.075923
	0.079126	0.078243	0.077677	0.076900	0.078212
	0.075587	0.076862	0.078203	0.078971	0.078309
	0.078041	0.077024	0.077299	0.077102	0.079757
	0.080050	0.078834	0.078320	0.076824	0.076910

5.4 Summary of Results

These two sets of numerical experiments show the capability of the MTECS algorithm to estimate the rotational diffusion coefficients from the angular-temporal cross-correlation data and filter the cross-correlation data so as to boost the signal-to-noise ratio.

In the first set of experiments, the algorithm estimated accurately the coefficient D_r, whose ground truth ranges from 0.01 to 0.1, indicating that the algorithm is able to handle both relatively fast and slow dynamics. However, we have to point out that special care is supposed to be taken in the cases that the particles rotate extremely slow or fast. If the particles rotates extremely slow, i.e. D_r is very small, then according to the theoretical analysis presented in Section 3.3, a huge amount of time is required to let the system experience different states to obtain accurate estimation of the angular-temporal cross-correlation. At the other extreme, when the D_r is large, for fixing Δt, the input data $\mathcal{C}$ (Eq. (4.5)) decays to zero very quickly, which may cause numerical instability in the algorithm. Thus either the motion should be slowed down, or the images are supposed to be taken much more frequently to make Δt smaller.

The filtered data output by the algorithm agrees with the ground truth calculated based the electron density ρ (Eq. (5.1)) and the theoretical formulation of the input data $\mathcal{C}$ (Eq. (4.5)), which implies that the MTECS algorithm is robust against the noise caused by the randomness of particle motion.

According to the figures of $\mathcal{B}_{iim0}^{\text{filtered}}$ against the ground truth, the algorithm generated successfully the estimation of each of the circular harmonic coefficients I_m. We notice that the error in estimation of I_m increases as m becomes larger. Intuitively, this is because the magnitude of I_m with large m is much smaller than I_m with small m. The correlation noise projector P_C tends to fit the overall cross-correlation data, so that the estimation of the I_m with small m is relatively better than the estimation of I_m with large m. Further refinement of the following subparts that handle I_m for each individual m separately might be helpful to this situation, and thus enable the production of better filtered data.

In the second set of experiments, we focused on applying the MTECS algorithm to data estimated from less number of images. The MTECS algorithm was still able to give good estimation of the rotational diffusion coefficients while much less images were used, confirming the robustness of the algorithm, since the angular-temporal cross-correlation data would become more noisy as the number of images collected decreases.

In the practical experiments performed on X-ray light sources, the data may contain many other types of noises, including the scattering of the background, the Poisson photon-counting noises, cosmic ray penetrating through the instruments, bad pixels on the detectors, etc. The

complication of the composition of these noises causes a lot of difficulties to model and clean the data. Currently, we are testing the performance of the MTECS algorithm on the datasets contaminated by these noises through numerical simulations. We are also seeking potential practical experiments to examine and improve the MTECS algorithm further.

Chapter 6

Conclusion

We have shown how to estimate rotational diffusion coefficients D_r from the angular-temporal cross-correlation estimated from XPCS images. The cross-correlation provides significant information which cannot be acquired through the autocorrelation function g_2. In fact, viewed as a natural generalization of g_2, the cross-correlation function has the potential of being applied to various other problems, despite the fact that it takes substantially more effort and resources to process and interpret the cross-correlation data owing to the size of data.

There are several advantages of our approach. One is that it requires little amount of prior knowledge, and in the presence of additional prior knowledge of the particles and the system, other operators can be incorporated into the algorithm to leverage these knowledge to find better estimation. Another advantage is its great expandability. The combination of cross-correlation functions and MTECS provides a reliable methodology to measure the rotational dynamics even beyond rotational diffusion. One can derive a conclusion similar to Theorem 3.1 for other rotational dynamics. The circular harmonic coefficients of cross-correlation curves vary because of the rotation. These variations can be computed through the first three subparts of the MTECS algorithm, and be studied by other operators that replace the last subpart, the exponential fitting P_E.

The flexibility of our algorithm allows the formulation of the subparts to be modified when necessary. In fact, there are several refinement of the subparts that can be investigated. In our implementation, the band-limiting projector can be viewed as a principal component regression (PCR), which are calculated without iterative solvers except the one looking for the singular value decomposition of the basis. It is still possible that the circular harmonic coefficients I_m can not be approximated well by those principal components. Though increase of the number of principal components can solve this, it will also impair the ability of denoising. One possible refinement is to replace the PCR by sparse linear regression. This computationally more expensive optimization is only needed to be solved in the first several

iterations, and the selection of the basis functions can be repeatedly used in the following iterations. Another possible refinement is of the last subparts, the exponential fitting P_E. The capability of P_E can be enhanced by deepened understanding of the noise propagation through the other subparts. By analyzing the structure of noises contained in the input to this subpart, we could find a formulation that handles the noises better and thus produces better estimation of the coefficients D_r.

One bottleneck of our algorithm is the lack of the analysis of the convergence. We just run the algorithm for enough number of iterations until the change between consecutive iterations is small. The analysis of convergence might not only guide us about how many iteration is required, but also help to develop useful tools to escape from the local "minima" and accelerate the convergence.

There are several other improvements and extensions that can be explored. In Chapter 7, two future works we plan to research will be discussed.

Chapter 7

Future Works

7.1 Polydispersity

In this section, we discuss the polydispersive case, i.e. the particles in the systems are not exactly identical. First assume that there are S different types of particles, and $N_p^{(s)}$ is the number of the s-th particles. Here we use similar notations, which are differentiated by superscript (s) when corresponding to the s-th particles. Then following the same steps, the Eq. (4.5) can be modified as

$$\mathcal{C}_{ii'jk} = \sum_{s=1}^{S} N_p^{(s)} \sum_{\substack{m=-\infty \\ m\neq 0}}^{\infty} e^{-i2m\Delta\phi} I_{2m}^{(s)}(q_i)\overline{I_{2m}(q_{i'})}^{(s)} e^{-4m^2 k\Delta t D_r^{(s)}}. \tag{7.1}$$

After applying the correlation noise projector P_C and the band-limiting projector, we obtain the tensors

$$\mathcal{G}_m = \sum_{s=1}^{S} A_m^{(s)} \otimes \overline{A_m^{(s)}} \otimes R_{:m}^{(s)}. \tag{7.2}$$

We conjecture that if the tensor rank decomposition and the exponential fitting are applied in the same was as in Section 4.3 and Section 4.4, then the estimated rotational diffusion coefficient D_r is between the maximum and minimum of $\{D_r^{(s)}\}_{s=1}^S$. We plan to examine such conjectures by further numerical experiments.

If the presence of the S types of particles is known, and S is small enough, then the decomposition Eq. (7.2) is unique (up to a scaling) [23, 24, 48, 50], so that $\{A_m^{(s)}\}_{s=1}^S$ and $\{R_{:m}^{(s)}\}_{s=1}^S$ could be retrieved by seeking the rank-S decomposition of $\mathcal{G}_m$. If S is large, then the decomposition Eq. (7.2) is not unique and extra knowledge is needed. Moreover, we assume the distribution of different particles can be continuously parameterized by coefficient s, as $p(s)$, $s \in [s_{min}, s_{max}]$. In the context of determination of the size distribution [3, 41], s

is the radius of the particle. Then Eq. (7.2) becomes

$$\mathcal{G}_m = \int_{s_{min}}^{s_{max}} \left(A_m^{(s)} \otimes \overline{A_m^{(s)}} \otimes R_{:m}^{(s)} \right) p(s) ds. \tag{7.3}$$

Through the discretization of the above expression and utilization of prior knowledge, the distribution $p(s)$ could be attained.

7.2 Three-dimensional Case

The current MTECS algorithm is designed for estimating the rotational diffusion coefficient in 2D rotational diffusion. A natural next step is to estimate the 3×3 rotational diffusion tensor of three-dimensional rotational diffusion.

Again, $J(\boldsymbol{q}, t)$ is the intensity measured at scattering vector $\boldsymbol{q}$ and time t. The first step is also the evaluation of the ensemble average

$$\langle J(\boldsymbol{q}, \tau) J(\boldsymbol{q}', \tau + t) \rangle = \mathbb{E}[J(\boldsymbol{q}, \tau) J(\boldsymbol{q}', \tau + t)], \tag{7.4}$$

where the expectation is over the distribution of motion of all the particles.

Still, we consider a monodisperse system containing N_p identical particles. Assuming that the characteristic function χ equals to the indicator function $\mathbf{1_0}$, and $\boldsymbol{q}, \boldsymbol{q}', \boldsymbol{q} + \boldsymbol{q}', \boldsymbol{q} - \boldsymbol{q}' \neq \mathbf{0}$, then applying the same computation as in Section 3.2, we can obtain

$$\mathbb{E}[J(\boldsymbol{q}, \tau) J(\boldsymbol{q}', \tau + t] = N_p \mathbb{E}[I(\Omega(\tau)\boldsymbol{q}) I(\Omega(\tau + t)\boldsymbol{q}')] + N_p(N_p - 1)\mathbb{E}[I(\Omega(\tau)\boldsymbol{q})]\mathbb{E}[I(\Omega(\tau)\boldsymbol{q}')], \tag{7.5}$$

where $\Omega(\cdot)$ is the three-dimensional rotation matrix depending on the orientation of particles.

Once the above equation is evaluated explicitly in terms of the rotational diffusion tensor, in the same manner as Chapter 4, we could design a series of subparts to solve the optimization for the rotational diffusion tensor. We are currently working on this extension.

Bibliography

[1] Bruce J Ackerson, Thomas W Taylor, and Noel A Clark. "Characterization of the local structure of fluids by apertured cross-correlation functions". In: *Physical Review A* 31.5 (1985), p. 3183.

[2] M Altarelli, RP Kurta, and IA Vartanyants. "X-ray cross-correlation analysis and local symmetries of disordered systems: General theory". In: *Physical Review B* 82.10 (2010), p. 104207.

[3] Gregory Beaucage, Hendrik K Kammler, and Sotiris E Pratsinis. "Particle size distributions from small-angle scattering using global scattering functions". In: *Journal of applied crystallography* 37.4 (2004), pp. 523–535.

[4] Bruce J Berne and Robert Pecora. *Dynamic light scattering: with applications to chemistry, biology, and physics*. Courier Corporation, 2000.

[5] Richard H Byrd et al. "A limited memory algorithm for bound constrained optimization". In: *SIAM Journal on scientific computing* 16.5 (1995), pp. 1190–1208.

[6] J Douglas Carroll and Jih-Jie Chang. "Analysis of individual differences in multidimensional scaling via an N-way generalization of "Eckart-Young" decomposition". In: *Psychometrika* 35.3 (1970), pp. 283–319.

[7] Noel A Clark, Bruce J Ackerson, and Alan J Hurd. "Multidetector scattering as a probe of local structure in disordered phases". In: *Physical Review Letters* 50.19 (1983), p. 1459.

[8] Jan KG Dhont. *An introduction to dynamics of colloids*. Elsevier, 1996.

[9] Jeffrey J Donatelli, James A Sethian, and Peter H Zwart. "Reconstruction from limited single-particle diffraction data via simultaneous determination of state, orientation, intensity, and phase". In: *Proceedings of the National Academy of Sciences* 114.28 (2017), pp. 7222–7227.

[10] Jeffrey J Donatelli, Peter H Zwart, and James A Sethian. "Iterative phasing for fluctuation X-ray scattering". In: *Proceedings of the National Academy of Sciences* 112.33 (2015), pp. 10286–10291.

[11] A Einstein. "On the movement of small particles suspended in stationary liquids required by the molecularkinetic theory of heat". In: *Ann. d. Phys* 17.549-560 (1905), p. 1.

[12] Albert Einstein. *Investigations on the Theory of the Brownian Movement*. Courier Corporation, 1956.

[13] Lawrence C Evans. *An introduction to stochastic differential equations*. Vol. 82. American Mathematical Soc., 2012.

[14] PP Ewald. "Introduction to the dynamical theory of X-ray diffraction". In: *Acta Crystallographica Section A: Crystal Physics, Diffraction, Theoretical and General Crystallography* 25.1 (1969), pp. 103–108.

[15] L Dale Favro. "Theory of the rotational Brownian motion of a free rigid body". In: *Physical Review* 119.1 (1960), p. 53.

[16] Michael P Friedlander and Kathrin Hatz. "Computing non-negative tensor factorizations". In: *Optimisation Methods and Software* 23.4 (2008), pp. 631–647.

[17] WH Furry. "Isotropic rotational Brownian motion". In: *Physical Review* 107.1 (1957), p. 7.

[18] Marco Grimaldo et al. "Dynamics of proteins in solution". In: *Quarterly Reviews of Biophysics* 52 (2019).

[19] Jari Kaipio and Erkki Somersalo. *Statistical and computational inverse problems*. Vol. 160. Springer Science & Business Media, 2006.

[20] Zvi Kam. "Determination of macromolecular structure in solution by spatial correlation of scattering fluctuations". In: *Macromolecules* 10.5 (1977), pp. 927–934.

[21] Henk AL Kiers. "Towards a standardized notation and terminology in multiway analysis". In: *Journal of Chemometrics: A Journal of the Chemometrics Society* 14.3 (2000), pp. 105–122.

[22] Tamara G Kolda and Brett W Bader. "Tensor decompositions and applications". In: *SIAM review* 51.3 (2009), pp. 455–500.

[23] Joseph B Kruskal. "Rank, decomposition, and uniqueness for 3-way and N-way arrays". In: *Multiway data analysis* (1989), pp. 7–18.

[24] Joseph B Kruskal. "Three-way arrays: rank and uniqueness of trilinear decompositions, with application to arithmetic complexity and statistics". In: *Linear algebra and its applications* 18.2 (1977), pp. 95–138.

[25] RP Kurta et al. "X-ray cross-correlation analysis applied to disordered two-dimensional systems". In: *Physical Review B* 85.18 (2012), p. 184204.

[26] Ruslan P Kurta et al. "Fluctuation X-ray scattering from nanorods in solution reveals weak temperature-dependent orientational ordering". In: *IUCrJ* 6.4 (2019), pp. 635–648.

[27] Paul Langevin. "Sur la théorie du mouvement brownien". In: *Compt. Rendus* 146 (1908), pp. 530–533.

[28] Michael Leitner et al. "Atomic diffusion studied with coherent X-rays". In: *Nature materials* 8.9 (2009), pp. 717–720.

[29] Haiguang Liu et al. "Computation of fluctuation scattering profiles via three-dimensional Zernike polynomials". In: *Acta Crystallographica Section A: Foundations of Crystallography* 68.5 (2012), pp. 561–567.

[30] Haiguang Liu et al. "Three-dimensional single-particle imaging using angular correlations from X-ray laser data". In: *Acta Crystallographica Section A: Foundations of Crystallography* 69.4 (2013), pp. 365–373.

[31] LB Lurio et al. "Absence of scaling for the intermediate scattering function of a hard-sphere suspension: Static and dynamic x-ray scattering from concentrated polystyrene latex spheres". In: *Physical review letters* 84.4 (2000), p. 785.

[32] Andrew V Martin. "Orientational order of liquids and glasses via fluctuation diffraction". In: *IUCrJ* 4.1 (2017), pp. 24–36.

[33] Andrew V Martin et al. "Fluctuation X-ray diffraction reveals three-dimensional nanostructure and disorder in self-assembled lipid phases". In: *Communications Materials* 1.1 (2020), pp. 1–8.

[34] Robert M Mazo. *Brownian motion: fluctuations, dynamics, and applications*. 112. Oxford University Press on Demand, 2002.

[35] Dennis M Mills. *Third-generation hard X-ray synchrotron radiation sources: source properties, optics, and experimental techniques*. 2002.

[36] Vladimir Alekseevich Morozov. *Methods for solving incorrectly posed problems*. Springer Science & Business Media, 2012.

[37] Edward Nelson. *Dynamical theories of Brownian motion*. Vol. 106. Princeton university press, 2020.

[38] Scott H Northrup, Stuart A Allison, and J Andrew McCammon. "Brownian dynamics simulation of diffusion-influenced bimolecular reactions". In: *The Journal of Chemical Physics* 80.4 (1984), pp. 1517–1524.

[39] Kanupriya Pande et al. "Ab initio structure determination from experimental fluctuation X-ray scattering data". In: *Proceedings of the National Academy of Sciences* 115.46 (2018), pp. 11772–11777.

[40] Bill Pedrini et al. "Two-dimensional structure from random multiparticle X-ray scattering images using cross-correlations". In: *Nature communications* 4.1 (2013), pp. 1–9.

[41] JA Potton, GJ Daniell, and BD Rainford. "Particle size distributions from SANS data using the maximum entropy method". In: *Journal of Applied Crystallography* 21.6 (1988), pp. 663–668.

[42] Aymeric Robert. "Measurement of self-diffusion constant with two-dimensional X-ray photon correlation spectroscopy". In: *Applied Crystallography* 40.s1 (2007), s34–s37.

[43] DK Saldin et al. "Beyond small-angle x-ray scattering: Exploiting angular correlations". In: *Physical Review B* 81.17 (2010), p. 174105.

[44] Tilo Seydel et al. "Capillary waves in slow motion". In: *Physical Review B* 63.7 (2001), p. 073409.

[45] Oleg G Shpyrko. "X-ray photon correlation spectroscopy". In: *Journal of synchrotron radiation* 21.5 (2014), pp. 1057–1064.

[46] Sunil K Sinha, Zhang Jiang, and Laurence B Lurio. "X-ray Photon Correlation Spectroscopy Studies of Surfaces and Thin Films". In: *Advanced Materials* 26.46 (2014), pp. 7764–7785.

[47] Dmitri Starodub et al. "Single-particle structure determination by correlations of snapshot X-ray diffraction patterns". In: *Nature communications* 3.1 (2012), pp. 1–7.

[48] Alwin Stegeman, Jos MF Ten Berge, and Lieven De Lathauwer. "Sufficient conditions for uniqueness in Candecomp/Parafac and Indscal with random component matrices". In: *Psychometrika* 71.2 (2006), pp. 219–229.

[49] Mark Sutton. "A review of X-ray intensity fluctuation spectroscopy". In: *Comptes rendus physique* 9.5-6 (2008), pp. 657–667.

[50] Jos MF Ten Berge and Nikolaos D Sidiropoulos. "On uniqueness in CANDECOMP/-PARAFAC". In: *Psychometrika* 67.3 (2002), pp. 399–409.

[51] Norbert Wiener. "Differential-Space". In: *Journal of Mathematics and Physics* 2.1-4 (1923), pp. 131–174.

[52] Norbert Wiener. "The average of an analytic functional and the Brownian movement". In: *Proceedings of the National Academy of Sciences of the United States of America* 7.10 (1921), p. 294.

[53] Norbert Wiener. "The mean of a functional of arbitrary elements". In: *Annals of Mathematics* (1920), pp. 66–72.

[54] Peter Wochner et al. "X-ray cross correlation analysis uncovers hidden local symmetries in disordered matter". In: *Proceedings of the National Academy of Sciences* 106.28 (2009), pp. 11511–11514.

Appendix A

List of Theorems

Theorem A.1 (**Parseval's Theorem for Fourier transform**). *For functions $f, g \in L^2(\mathbb{R}^d)$, we have*

$$\int_{\mathbb{R}^d} f(\mathbf{r})\overline{g(\mathbf{r})}d\mathbf{r} = \int_{\mathbb{R}^d} \hat{f}(\boldsymbol{q})\overline{\hat{g}(\boldsymbol{q})}d\boldsymbol{q}. \tag{A.1}$$

Theorem A.2 (**Poisson Summation Formula**). *Let $f : \mathbb{R} \to \mathbb{C}$ be a Schwartz function, i.e. it is a smooth function satisfying*

$$\sup_{x\in\mathbb{R}} |x|^k |f^{(l)}(x)| < \infty, \quad \forall k, l \geq 0. \tag{A.2}$$

Then

$$\sum_{n=-\infty}^{\infty} f(x + nP) = \frac{1}{P} \sum_{k=-\infty}^{\infty} \hat{f}\left(\frac{k}{P}\right) e^{i2\pi \frac{k}{P} x}, \quad \forall P > 0. \tag{A.3}$$

Theorem A.3 (**Wiener-Khinchin Theorem**). *For $f \in L^2(\mathbb{R}^d)$,*

$$\hat{A}f = |\hat{f}|^2. \tag{A.4}$$

Theorem A.4 (**Friedel's Law**). *For a real-value function $f \in L^1(\mathbb{R}^d) + L^2(\mathbb{R}^d)$,*

$$\hat{f}(\boldsymbol{q}) = \overline{\hat{f}(-\boldsymbol{q})}. \tag{A.5}$$

This theorem implies that the squared magnitude of Fourier transform of real-valued function exhibits centrosymmetry,

$$|\hat{f}(\boldsymbol{q})|^2 = |\hat{f}(-\boldsymbol{q})|^2. \tag{A.6}$$

Theorem A.5 (**Parseval's Theorem for Fourier series**). *For $f, g \in L^2([0, 2\pi])$, with Fourier series coefficients $\{f_m\}_{m=-\infty}^{\infty}$ and $\{g_m\}_{m=-\infty}^{\infty}$, we have*

$$\frac{1}{2\pi} \int_0^{2\pi} f(\phi)\overline{g(\phi)} = \sum_{m=-\infty}^{\infty} f_m \overline{g_m}. \tag{A.7}$$

Theorem A.6 (**Parseval's Theorem for Hankel transform**). *For $f, g \in L^1(\mathbb{R}^+) \cap L^2(\mathbb{R}^+)$ and $m \geq -\frac{1}{2}$, we have*

$$\int_0^\infty f(r)\overline{g(r)}rdr = \int_0^\infty (\mathcal{H}_m f)(q)\overline{(\mathcal{H}_m g)(q)}qdq. \tag{A.8}$$

Theorem A.7 (**Azuma-Hoeffding Inequality**). *Suppose a discrete time martingale $\{X_n : n \in \mathbb{Z}^+\}$ satisfies*

$$|X_n - X_{n-1}| \leq c_n, \ n = 1, 2, \cdots, \tag{A.9}$$

where c_n are all constants. Then for any $\epsilon > 0$, $n = 0, 1, \cdots$,

$$\mathrm{P}(|X_n - X_0| \geq \epsilon) \leq 2\exp\left(\frac{-2\epsilon^2}{\sum_{k=1}^n c_k^2}\right). \tag{A.10}$$

Theorem A.8 (**Fubini's Theorem**). *Let X and Y be σ-finite measure spaces, and $f : X \times Y \to \mathbb{R}$ is integrable. If*

$$\int_{X\times Y} |f(x,y)|d(x,y) < \infty, \tag{A.11}$$

then

$$\int_X \int_Y f(x,y)dydx = \int_Y \int_X f(x,y)dxdy = \int_{X\times Y} f(x,y)d(x,y). \tag{A.12}$$

Appendix B

Derivation of Eq. (3.5)

Here we derive Eq. (3.5) using exactly the same techniques as the derivation of Theorem 3.1. Similar notations will also be used.

Proof of Eq. (3.5). According to Eq. (2.30),

$$\mathbb{E}[J(q,\phi,t)] = \sum_{n_1,n_2=1}^{N_p} \mathbb{E}\big[e^{-2\pi i \boldsymbol{q}\cdot(\boldsymbol{r}_{n_1}(0)-\boldsymbol{r}_{n_2}(0))}\big] \cdot \mathbb{E}\big[\hat{\rho}\big(q,\phi-\theta_{n_1}(0)\big)\overline{\hat{\rho}\big(q,\phi-\theta_{n_2}(0)\big)}\hat{\rho}\big]. \tag{B.1}$$

We denote the terms in the above summation as $S_{n_1 n_2}$. The value of the N_p terms associated with $n_1 = n_2$ is

$$\begin{aligned} S_{11} &= \mathbb{E}\big[I\big(q,\phi-\theta(t)\big)\big] && \text{(B.2)}\\ &= \sum_{m=-\infty}^{\infty} I_m(q)e^{im\phi}\mathbb{E}\big[e^{-im\theta(0)}\big]\mathbb{E}\big[e^{-im(\theta(t)-\theta(0))}\big] && \text{(B.3)}\\ &= \sum_{m=-\infty}^{\infty} I_m(q)e^{im\phi}\delta_{m0}e^{-m^2tD_r} && \text{(B.4)}\\ &= I_0(q). && \text{(B.5)} \end{aligned}$$

When $n_1 \neq n_2$, the terms can be written as:

$$S_{12} = \mathbb{E}\big[e^{-2\pi i\boldsymbol{q}\cdot\boldsymbol{r}_1(t)}\big]\mathbb{E}\big[\hat{\rho}\big(q,\phi-\theta_1(t)\big)\big]\mathbb{E}\big[e^{2\pi i\boldsymbol{q}\cdot\boldsymbol{r}_1(t)}\big]\mathbb{E}\big[\overline{\hat{\rho}\big(q,\phi-\theta_1(t)\big)}\big]. \tag{B.6}$$

Similarly to the calculation of S_{11}, we can obtain

$$\mathbb{E}\big[\hat{\rho}\big(q,\phi-\theta_1(t)\big)\big] = \hat{\rho}_0(q). \tag{B.7}$$

Additionally,

$$\mathbb{E}\big[e^{-2\pi i\boldsymbol{q}\cdot\boldsymbol{r}_1(t)}\big] = \mathbb{E}\big[e^{-2\pi i\boldsymbol{q}\cdot(\boldsymbol{r}_1(t)-\boldsymbol{r}_1(0))}\big]\mathbb{E}\big[e^{-2\pi i\boldsymbol{q}\cdot\boldsymbol{r}_1(0)}\big] \tag{B.8}$$

$$= \chi(2\pi \boldsymbol{q}) e^{-4\pi^2 q^2 t D_t}. \tag{B.9}$$

Thus

$$S_{12} = |\chi(2\pi \boldsymbol{q})|^2 e^{-8\pi^2 q^2 t D_t} |\hat{\rho}_0(q)|^2. \tag{B.10}$$

Combination of Eq. (B.1),Eq. (B.5) and Eq. (B.10) completes the proof of Eq. (3.5). □